COO-4020-3

A Study of Flow and Loss Processes at the Ends of a Linear Theta Pinch

Progress Report
for the period

June 1, 1976 - May 31, 1977

Thomas M. York and Edward H. Klevans

The Pennsylvania State University
University Park, Pennsylvania 16802

February 1977

Prepared for

The U.S. Energy Research and Development Administration

under

Contract No. E4-76-S-02-4020*000

DISCLAIMER

Table of Contents

List of Illustrations

Abstract

Experimental and analytical studies initiating and supporting research on flow and energy losses at the ends of a linear theta pinch have been carried out. A 25 cm linear pinch coil has been driven by a 515,000 A discharge with 10μsec half-cycle time supplied by a 100μF, 18 kV energy storage system. With reliable preionization generated up to 400 mT He, current sheath behavior has been identified with magnetic loop probes and double loop probes. Spectroscopic determination of preionization has been made. A ruby laser Thomson scattering diagnostic has been designed and is being procured. A study of transient plasma behavior in a 10 cm theta pinch has been carried out with a Twyman-Green interferometer using a 7 mW He-Ne CW laser. Pressure, electric field, and velocity probe diagnostics have received preliminary testing. Design work has been completed for the doubling of pinch length and energy storage system. Studies of particle loss scaling and reactor scaling of linear theta pinch devices have been reported. Detailed calculations of plasma properties at the end of the pinch coil following expansion from the central coil have been carried out. A 0-D, time dependent computer code that includes conduction, convection, and magnetic field diffusion has been developed. Predicted plasma behavior is in good agreement with experimental data.

I. INTRODUCTION

The work to be discussed in this progress report represents the efforts of an initial nine-month period of study of the problems of flow and loss at the end of a linear theta pinch. Since this work addresses the processes that are expected to occur at the ends of longer (1-5 m) linear devices by studying short (25-50 cm) linear devices, the experimental and analytical emphasis have been unique. Specifically, along with the inherent activity involved in system development of the new experimental pinch device, there has been a predominant preoccupation with diagnostics development. Indeed, one reason for conducting the present experimental research is the accessability of the end loss plasma to a broader range of diagnostics than are available in longer but hotter pinch machines. Likewise, on reviewing the analytical work, there clearly has been a predominant interest in the problems of scaling experiments as well as reactor configurations. The notion has been pursued that judicious introduction and utilization of experimentally indicated behavior patterns and checks into analytical formulations will produce improvements in our understanding of pinch events.

A brief topical summary of activity will now be presented; all research efforts will be described in detail within the report. The experimental effort has progressed with the reliable operational capability of the 100 μF, 18 kV bank driving the 25 cm theta coil, and with the incorporation of a new preionization system. Inconsistencies in switching are being countered by the imminent introduction of new

sensing circuitry. Preliminary diagnostic studies have indicated intense sheath collapse in the 25 cm coil in conformance with expectations. Magnetic probe, double loop and spectroscopic studies have been initiated. Pressure, electric field, and velocity probes have been initially tested in a 10 cm long test pinch developed for Twyman-Green interferometer evaluation. That study is nearing completion and will be reported in an M.S. thesis and report. Considerable effort has been expended in evaluating and hopefully extending the state of the art in Thomson scattering diagnostics; ruby laser equipment is being procured. Design of the circuitry and components for doubling bank capacity and coil length has been completed and fabrication of individual units is being initiated.

Analytical studies have resulted in two technical reports, one on scaling experiments and the other on design parameters for reactor length linear pinches; these are appended. Considerable effort has been expended in predicting the state of the plasma in the end region of the discharge tube. Finally, several numerical computation models have been developed. These have been successfully used to simulate column behavior and loss behavior in several experiments that have been carried out.

In the conduct of this research, two principal investigators have been receiving the capable cooperation and assistance of two faculty members of the Department of Electrical Engineering at Penn State: Professor James Robinson and Professor Richard Mollo. Graduate research assistants who have been responsible for the detailed conduct of much of the work have included: John Heidrich, Elmer Stover, Barry Jacoby,

and Robert Freeman. The efforts of each of these individuals is specifically acknowledged following the title of each research activity.

II. EXPERIMENTAL STUDIES OF THE 25 CM THETA PINCH (Heidrich, Robinson)

A 25 cm long, 10 cm bore theta pinch coil is being used to conduct basic studies of the transient flows from the ends of a confined plasma column. The pinch coil is connected to a commercial design high power pulse forming network that is being adapted for laboratory plasma physics studies. The basic electrical discharge apparatus, modifications for preionization, diagnostics, basic performance, and future plans will be described.

1. Characteristics of the Electrical Discharge Apparatus

The electrical discharge pulse forming network was manufactured by Brown Boveri, Inc., Mannheim, Germany. In its original form it consisted of four rows of 7.7μF, 18kV capacitors with four capacitors per row. The capacitors are discharged through four pressurized spark gaps, with one gap for each row. The current is fed into a collector by 32 coaxial cables; there are eight cables per row. Each row can be charged individually; hence, combinations of one to four rows can be discharged. The total original bank capacitance was 123.2μF, and the total original bank inductance was 53nH. Using a 40nH shorting bar on the collector gave a total inductance of 93nH and a cycle time of 21.3μsec. This was specified by the manufacturer and verified in laboratory tests. The bank has an effective operating voltage range from 12kV to 18kV.

The original bank operation was completely automated. The rate of charging, level of charge, firing, and zeroing of the bank was done automatically. There are numerous built-in safeguards such that if a malfunction occurs during operation the control circuitry will automatically zero the energy storage capacitors.

The apparatus is designed with three separate electrical systems: a 220 volt three phase system, a 48 volt d.c. battery system, and a high voltage system; an electrically controlled compressed air system drives numerous switching devices. Specifically, the 220 volt supply system powers extensive control circuitry. The 48 volt d.c. system powers compressed air valves which operate knife switches on the high voltage system. The high voltage system consists of a two component power supply; one supply for main bank charging and the other for charging a 1 μF switch trigger capacitor. The high voltage system is isolated from the 220 volt system by isolation transformers and banks of resistors.

The compressed air system consists of two reserve tanks; one at 5 atmospheres and the other at 1 atmosphere. The 5 atmosphere supply is used to operate the knife switches on the high voltage system and the 1 atmosphere supply pressurizes the four bank spark gaps.

In order to incorporate the theta pinch coil and a preionization system into the original system, some modifications were necessary. The master spark gap on the trigger capacitor had been a 5 atm. compressed air gap, and it was discharged by releasing the compressed air. In order to allow precise timing of main bank discharge after preionization initiation, this gap had to be replaced by an electrically triggered gap that could be discharged at a preset delay time ranging from 10 to 100 μsec. This was satisfactorily accomplished early in the contract year.

With the fitting of collector plates, the pinch coil described above completed the circuit and initial bank evaluations were

carried out. During this phase, three capacitors failed by shorting out; as these capacitors were manufactured in England they were not replaceable. Hence, it was decided to reduce the bank capacitance from its original 123.2 μF to 100.1 μF for the duration of the transient studies. This would allow operation with two spare capacitors of the original design. Replacement of these units will be addressed in the renewal proposal.

Following an extensive period of test and evaluation, the characteristics of the modified facility were identified as follows:

Max. Voltage (kV)	18
Total Capacitance (μF)	100.1
Max. Energy (J)	16,220
Coil Length (m)	.25
Coil Diameter (cm)	10.5
Coil Inductance (nH) (ideal)	40
Source Inductance (nH)	56
Max. Current (KA)	515
Max. E_θ (tube i.d.) (Volts/cm)	173
Max. Mag. Field (kG)	23.9
Quarter-Cycle Time (μsec)	4.8
Total Number of Capacitors Used	1.3
Capacitance Per Capacitor (μF)	7.7
Inductance of 13 Capacitors (nH)	3
Inductance of Four Rows of Parallel Plate (nH)	11
Inductance of 32 Coaxial Cables (nH)	15
Inductance of Modified Collector (nH)	23

A typical record showing the response of the total bank discharge from 18 kV is presented in Fig. 1. The current was monitored by a calibrated Rogowski loop fitted around one of the plates feeding the pinch coil; the response is typical for a RLC circuit without crowbar.

2. Preionization System Design and Discharge Performance With Main Bank

The preionization state of theta-pinch plasmas has been recognized as having considerable importance.[1,2] It has been shown that the level of preionization can substantially affect the collapsed plasma column properties.[3] Consequently, a preionization system was designed so that both hydrogen and helium could be preionized effectively at fill pressures ranging from 50 mT to 500 mT.

The preionization system consists of an initiation HF discharge followed by a ringing θ-discharge. The HF discharge consists of two RG-8/U coaxial cables each 2.5 meters long. A 2.8 μF capacitor at 18 kV is discharged into both the cables and the parallel plate connecting the capacitor to the θ pinch coil. The end of each cable has its outer shield stripped away and its solid inner conductor wrapped around the theta pinch tube. Thus the inner conductor is capacitively coupled to the gas. There is one cable on each side of the theta pinch coil. The HF discharge, ringing at 20 MHz, starts the preionization and the θ-discharge completes the preionization process. The characteristics of the θ-discharge system are tabulated below.

θ-Discharge System Parameters

Max. Voltage (kV):	18
Total Capacitance (μF):	2.8

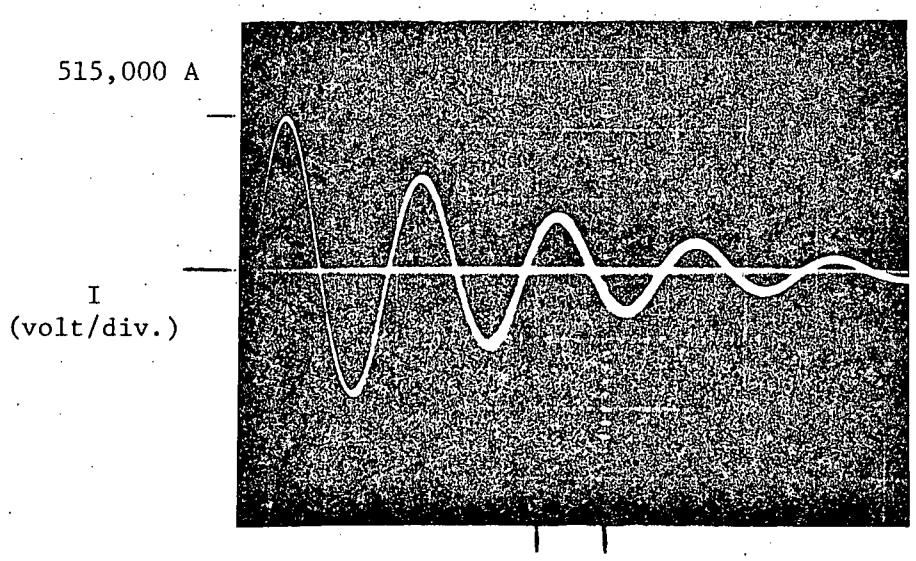

Figure 1. Current History of 100 μF Bank Discharged through 25 cm Theta Pinch

Max. Energy (Joules):	454
Total Inductance (nH): (Includes 25 cm θ pinch coil)	226
Max. Current (kamp):	58.2
Max. E_θ (tube i.d.) (Volts/cm):	76.3
Max. B (kGauss):	2.7
Cycle Time (μs):	5
Number of Capacitors:	1
Fraction of Energy Transferred to coil: (%)	15

Initial experiments have indicated that the preionization system is performing adequately. A preliminary spectroscopic study was performed on a preionization hydrogen plasma at 100 mT fill pressure. The percent preionization at the coil's center was found to be 74% at 10 μsec after initiation of the preionization discharge and it decayed to 16% at 30 μsec. A discussion of this study can be found in the section on spectroscopy. Although no spectroscopic analysis has been done yet with helium, an appropriate spectroscopic study of both hydrogen and helium preionization plasma is currently underway.

Reproducible collapse has been observed in helium at fill pressures up to 400 mT, e.g. see Fig. 2. The top trace in Fig. 2 is a dB/dt signal from a magnetic pickup loop on the preionization system. The discontinuity just after 30 μsec is from the main bank discharging. The bottom trace is a dB/dt signal from a magnetic field probe inserted radially at the coil's midplane and at a radius of 2.25 cm from the center of the 4.5 cm radius discharge tube. This trace was triggered upon the discharge of the main bank and ends 4.5 μsec later (main bank

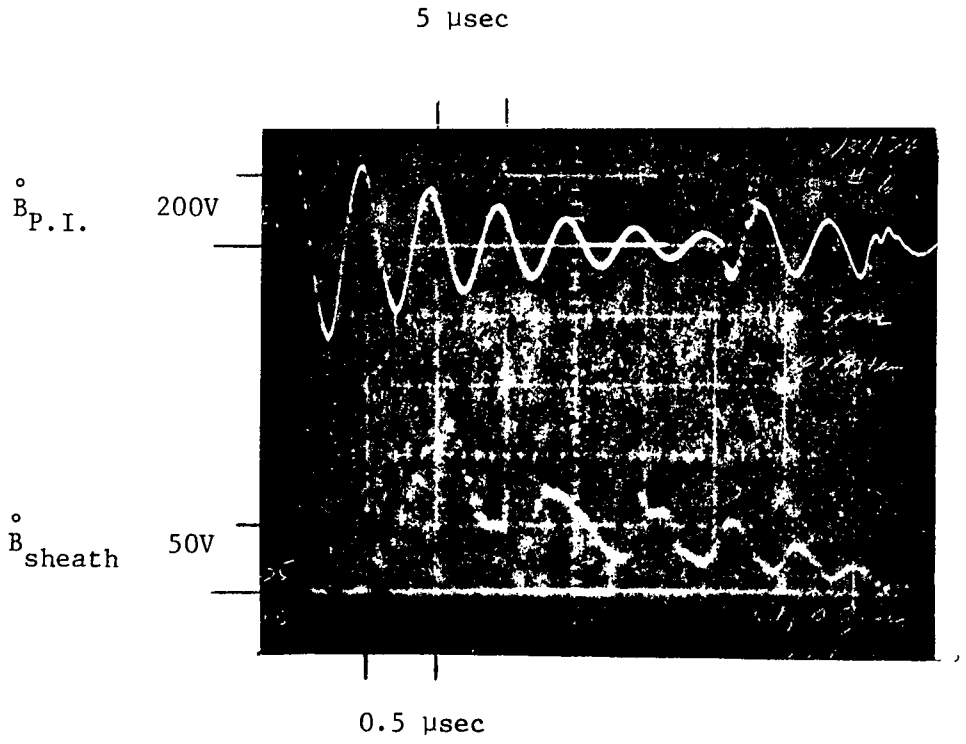

Figure 2. Sheath Formation at 400 mT Helium Fill Pressure

Upper trace is $\dot{B}$ for the preionization discharge. Lower trace is $\dot{B}$ for an internal magnetic probe inserted to a radial position of 2.25 cm.

1/4 cycle time). The first 0.5 μsec indicates dB/dt = 0, indicative of a diamagnetic plasma. The signal between 0.5 & 1.3 μsec indicates the current sheath passing over the probe.

The satisfactory preionization of helium at high fill pressures was anticipated by considering the energy an electron acquires in E_θ between ionizing collisions with helium atoms. The average electric field in the first quarter cycle of the preionizer is 48.6 volts/cm and the electron mean free path between ionizing collisions is about 1 cm. Hence, an electron has, on the average, about 48 eV upon collision with a helium atom. Comparing this with the 24.48 eV ionization potential of helium it is seen that collisional ionization of helium is expected.

The main bank discharge in conjunction with the preionization system is shown in Fig. 3. This figure presents an oscilloscope record of current through the θ pinch coil, obtained by integration of a Rogowski loop signal. The first 30 μsec of the record is the preionization current and the remaining part is the main bank current. It will be noted that all experiments studying the plasma column and endloss, including those reported in the following sections, are performed during the first half cycle of the main bank discharge.

3. Diagnostics

a. Local magnetic field sensors

Two magnetic field probes have been used, each probe consisting of a small multi-turn coil enclosed in a pyrex tube.[4] Both probes have been used to measure the axial component of magnetic field; their rise-times are less than 10^{-8} seconds. One probe was inserted radially

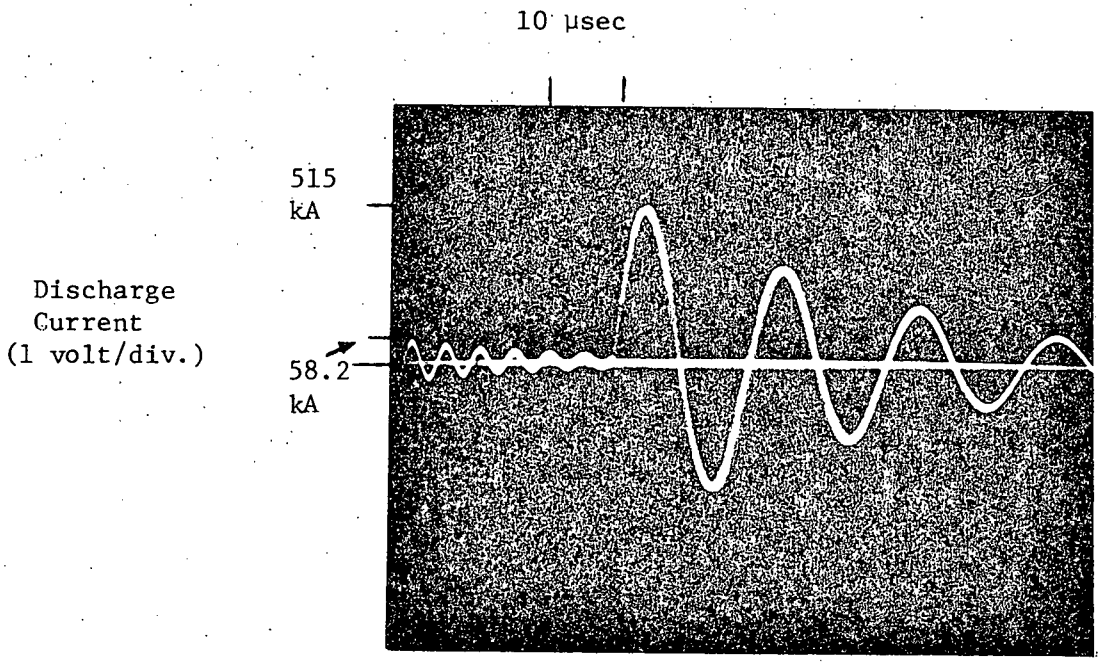

Figure 3. Current Waveform of Preionization Discharge Followed by that of the Main Bank (18 kV charge).

into the axial center position of the theta pinch (radial probe) and the other was inserted axially (axial probe). Magnetic field measurements during sheath collapse inside the theta pinch have been made. Measurements made thus far have given indications of pinch time and sheath velocity. Detailed study of such magnetic field measurements are expected to indicate percentage of mass pickup, current sheath thickness, column energy and column density. By placement of a probe inside the plasma, trapped field from the preionization can also be measured just before collapse of the plasma column

b. Double loop excluded flux sensor

A double loop system for measurement of plasma diamagnetism has been developed.[5] It consists of two coils; a single turn large area coil fitted in a small slot between the inside of the theta pinch coil and the discharge tube, the other a Rogowski coil fitted through a small slot located in one of the collector plates leading to the theta pinch. The large area coil responds to changing flux inside the theta pinch coil and the Rogowski coil responds to changing current through the coil. The signals from the two coils are balanced by a resistive differencing circuit with a vacuum inside the discharge tube. The integral of the difference signal between the two coils obtained with a plasma is proportional to the flux excluded by the plasma. No metal bar was needed to calibrate the apparatus as the needed RC time constant and voltage divider ratio of the electronics were measured directly. With a specification of the density profile and the plasma β on axis, measurement of the excluded flux provides an indication of the plasma radius as a function of time.

4. Pinch Characteristics

The axial component (z component) of the vacuum magnetic field was mapped using the probes described above. Inside the coil, the z component of the field was found to be essentially independent of radius and to be constant from the coil midposition to approximately 5 cm from the end. Outside the coil, for fixed axial positions the z component was found to drop slightly with increasing radius. These points are illustrated on Fig. 4. The fact that the magnetic field is found to be uniform over more than half the coil length is indicative of a non-uniform current distribution in the coil. With no plasma in the discharge tube there exists a higher magnetic field than would be predicted by a uniform current distribution along the coil, and so, there appears to be a higher current density on the outer third of the coil's length than on the central third.

Sheath collapse in helium for fill pressures of 50 and 100 mT has been studied. The collapse velocity was found to increase when the delay time between initiation of the preionization and the main discharge was increased. A possible explanation of this fact is related to percent preionization: as the delay time was increased, the percent preionization decreased giving rise to less mass pickup during the collapse thus leading to a faster collapse. These events are presented in Fig. 5(a, b), where two shots with different delay in main bank initiation were done in helium at 50 mT fill pressure. The lower traces are records of the current wave form in the theta coil. The first part of the current wave form is due to the preionization the later is from the main bank. The upper traces are records of $\dot{B}_z$ made

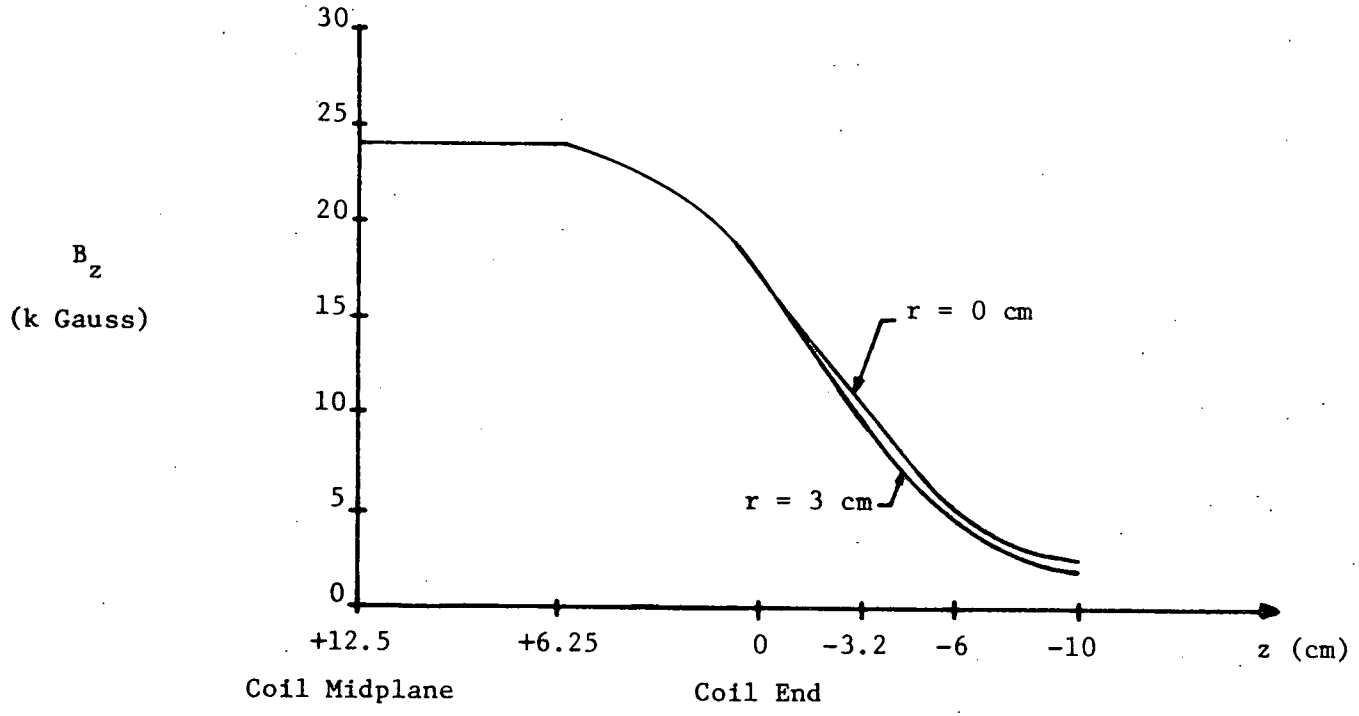

Figure 4. Axial Magnetic Field Variation with Axial Position

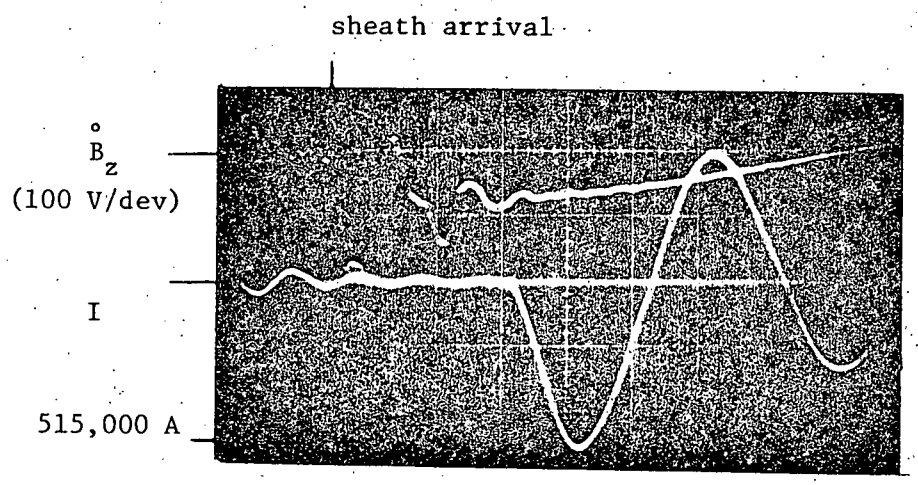

(a) Main bank initiation delay: 21 μsec

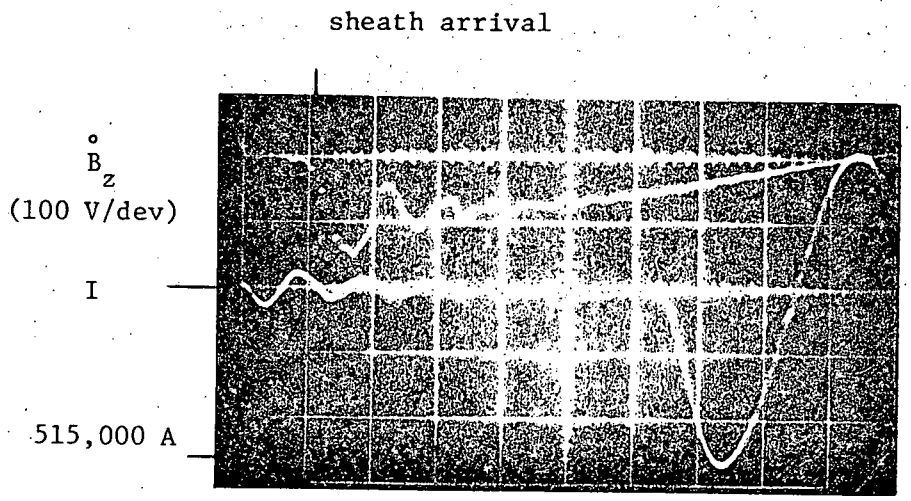

(b) Main bank initiation delay: 32 μsec

Figure 5. Effect of Percent Preionization on Sheath Collapse

50 mT helium fill pressure. Upper trace: $\dot{B}_z$ at z = 6.25 in. and r = 1.25 cm, 0.5 μsec/cm, triggered at onset of main bank. Lower trace: theta pinch coil discharge current 5 μsec/cm

with the axial probe. These traces were triggered upon initiation of the main bank and extend through the first quarter cycle. Notice that the initial signal is zero, indicative of a magnetic probe inside a diamagnetic plasma. The first negative-going signal on $\dot{B}_z$ is the current sheath passing over the probe. In (a) the delay time is 21 μsec. and the leading edge of the sheath start passing over the probe at about 0.7 μsec. In (b) the delay time is 32 μsec and the sheath starts passing over the probe in about 0.55 μsec. Hence, a faster collapse was observed when firing of the main bank was delayed.

Another feature of the collapse in helium found at both 50 and 100 mT fill pressures was that there was a faster collapse in the coil's midregion than in the outer 1/3 of the coil. This phenomena is illustrated in Fig. 6. Records (a) and (b) are of the same discharge. The relevant traces here are the upper traces in both figures. In (a), a record of $\dot{B}_z$ using the radial probe at Z = +12.5 an and r = 2.25 cm is presented; in (b) the upper trace is a record of $\dot{B}_z$ using the axial probe located at Z = +6.25 cm and r = +2.25 cm. It is noted that the sheath at Z = +6.25 cm took about 0.3 μsec longer to get to r = 2.25 cm than the sheath at Z = +12.5 cm. As the axial vacuum magnetic field was found to be equal at both these positions, the slower collapse at Z = +6.25 cm is not believed to be due to a smaller field there. Indeed, a slower collapse at the Z = +6.25 cm position implies a larger plasma radius, hence magnetic lines outside the plasma in this region would be under more compression than at the coil's center thus leading to higher field strength and a larger $\bar{v} \times \vec{B}$ collapse force. This type of behavior will be explored in detail. However, a possible reason for

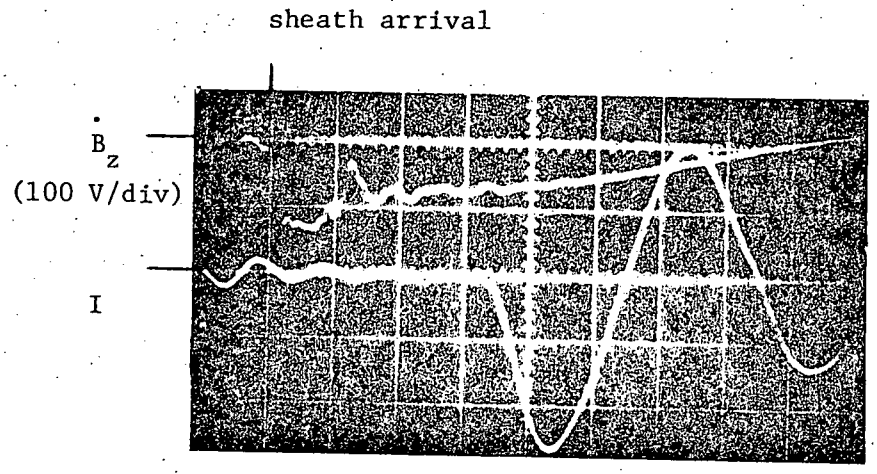

(a) Upper trace: axial probe $\dot{B}_z$ at z = 16.25 cm and r = 2.25 cm, 0.5 μsec/div.
Lower trace: pinch coil discharge current, 5 μsec/cm

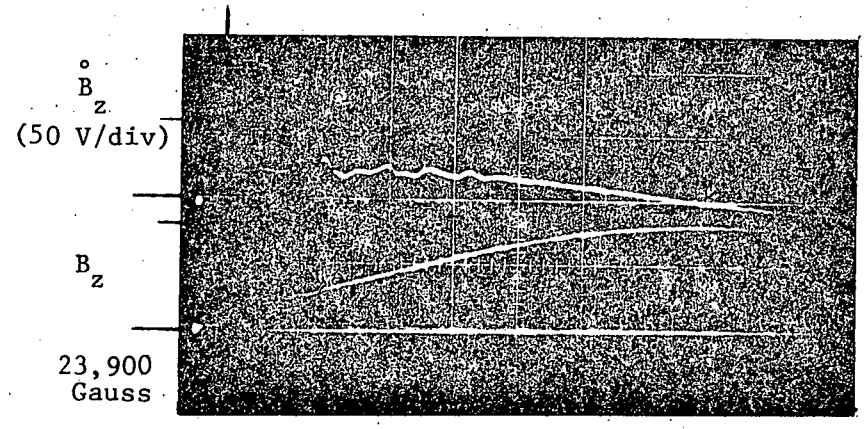

(b) Upper trace: radial probe $\dot{B}_z$ at z = 12.5 cm and r = 2.25 cm, 0.5 μsec/div.
Lower trace: B_z integrated from B_z radial probe

Figure 6. Comparison of Sheath Collapse at Different Axial Positions 50 mT Helium fill

this difference in collapse could be that the mass begins to flow out of the coil's midsection as the sheath collapses. This would cause a higher mass density at positions near the end resulting in slower collapse at Z = +6.25 cm than at the coil midplane.

Preliminary excluded flux measurements at the coil midsection have been performed. Figure 7(a) shows a null difference signal obtained with no plasma in the discharge tube. The upper trace is the first half cycle current of the main discharge and the bottom trace is the nulled difference signal. Fig. 7(b) shows a typical signal with excluded flux due to the presence of plasma; the bottom trace is the difference signal between the excluded flux coils. Negative signal represents exclusion of flux from the plasma. Collapse times indicated by excluded flux measurements are in agreement with those expected from snowplow calculations. Effective sheath radii obtained from these measurements correspond to those obtained from magnetic field probe data. More extensive excluded flux measurements are underway.

5. Spectroscopy

A spectroscopic system useful for observing spectra from the 25 cm theta pinch has been developed. The system consists of a Jarrell Ash 50 cm spectrometer along with associated optics and electronics. Preionization hydrogen and helium plasmas produced in the theta pinch are expected to have densities between 10^{15} cm^{-3} and 10^{16} cm^{-3} and electron temperatures of about 2 eV. Collapsed plasma columns of both gases are expected to have densities on the order of 10^{17} cm^{-3} and ion and electron temperatures between 20 eV and 30 eV. The apparatus should be capable of performing spectroscopic measurements that yield electron

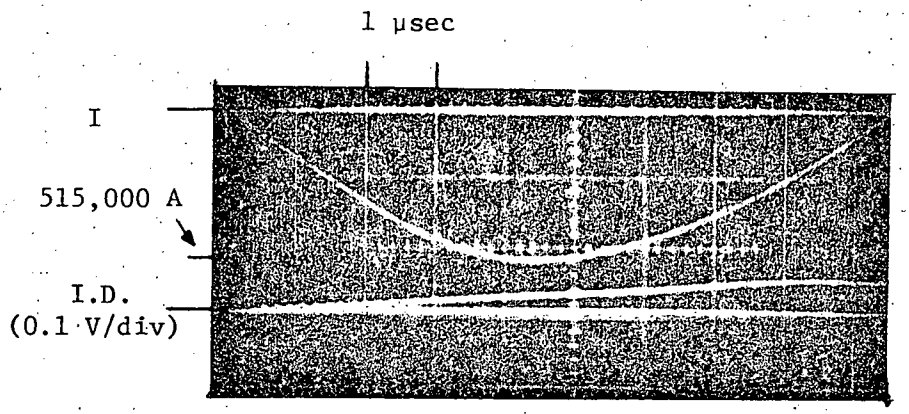

(a) Upper trace: Pinch coil discharge current
Lower trace: Null signal between the double loop coils with no plasma in discharge tube

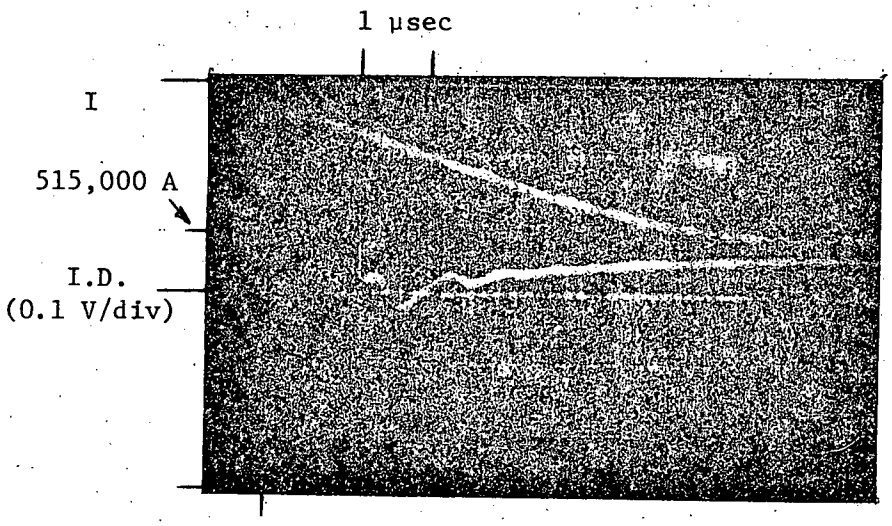

(b) Upper trace: Pinch coil discharge current
Lower trace: Diamagnetic signal due to the presence of helium plasma from 50 mT fill

Figure 7. Excluded Flux Measurements of the Theta Pinch Plasma

temperature, electron density and possibly ion temperatures of the above plasmas.[6] The results discussed briefly below are for a measurement of electron density in a preionized hydrogen plasma.

The spectrometer has an Ebert mounting, which consists of an entrance slit, a spherical mirror, a diffraction grating and an exit slit. The entrance and exit slit openings are equal; this width can be adjusted from 5 microns to 400 microns. The resolution of the spectrometer varies from 0.2 Angstroms at 5 micron slit openings to 1.2 Angstroms at 100 micron slit openings. The spectrometer's optical range is from 2000 Angstroms to 9000 Angstroms.

The chords across the plasma column are defined by two vertical sets of 0.04 inch diameter holes drilled in the side of the theta pinch coil. One set of holes is at the midplane of the theta pinch coil. The other is 6.25 cm in from the end of the coil. There is a 0.5 cm spacing between each hole.

The associated optics consists of a 3 inch diameter spherical mirror and a plane mirror. The spherical mirror views a selected chord across the plasma column through one of the holes. Light gathered by the spherical mirror is reflected by the plane mirror and is focused on the entrance slit of the spectrometer. Since the holes in the side of the theta pinch have a small aspect ratio; i.e., hole diameter/hole length is small, the depth of field viewed is large compared to the depth of plasma across each chord. Hence, the total intensity of the light gathered is constant across the chord being viewed; thus was verified by a separate experiment. Since the field of view is found to be small compared to the plasma radius, a chord across the plasma column is well defined.

The electronics used includes: an RCA 1P21 photomultiplier tube, an amplifier and a Tektronix 556 oscilloscope. The amplifier uses an RCA CA3015A operational amplifier. The amplifier has a transresistance (output voltage/input current) of 300,000 ohms. The entire circuit, including photomultiplier tube, amplifier, and scope, has a risetime of 0.5 microseconds.

Electron density and temperature of hydrogen and helium preionization plasmas can be measured for fill pressures ranging from 50 mT to hundreds of millitorr. Electron density is to be measured using Stark broadening of hydrogen lines. In order to do the measurement in helium a small percentage of hydrogen will be added to the helium fill. Use of the well defined H_β line is expected to yield electron densities with 5% accuracy. Preliminary density measurements in hydrogen have been performed and will be discussed below. Electron temperature in the preionization hydrogen plasma can be obtained from a ratio of hydrogen line intensities such as, H_β, H_γ or H_δ, to the underlying continuum in a 100 Å band centered at the line. Accuracies of 10% or better are expected for $ne \geq 10^{14}$ cm^{-3}, which is expected to be true for all fill pressures to be considered. The preionization helium plasma electron temperatures can be obtained from ratios of neutral helium lines to the 100 Å continuum. Accuracies of 10% are again expected.

Electron temperature, electron density and possibly ion temperature are to be measured in the collapsed plasma column inside the theta pinch. Electron density in both hydrogen and helium plasma are to be obtained from Stark broadening of spectral lines. Electron temperatures in hydrogen can be obtained from the intensity ratio of impurity lines

such as the carbon lines C_{IV} and C_{III}. In helium[7] electron temperatures are to be obtained from the ratio of He_{II} line intensity to the 100 Å continuum underlying the line. All the above measurements of electron density and electron temperature in the plasma column should yield results that are at least 20% accurate. The possibility of obtaining ion temperature from Doppler broadening also exists but due to the small broadening expected, ~1 Å, this may not be practical.

A computer program has been developed to Abel invert intensities recorded across chords of the plasma to yield intensities as a function of radius. Hence, all the above measurements on the plasma column can yield densities and temperatures as a function of plasma radius. Using the above mentioned spectroscopic system should yield temperature and density measurements with a time resolution of better than 1 microsecond and a radial spatial resolution of about 0.5 cm at both the coil midsection and 6.25 cm in from the end of the coil.

Electron density measurements have been made in a preionization hydrogen plasma for 100 mT fill pressures. The electron density was obtained from Stark broadening of the H_β line. Intensity measurements were done by viewing across the control chord running through the midsection of the theta pinch. Halfwidth of the H_β line was obtained by measuring the intensity as a function of time at various distances from the line center for consecutive discharges. Typical results are shown in Fig. 8 (a,b) both of which were triggered upon discharge of the preionizer. Fig. 8a is a record of intensity at 4861 Å and Fig. 8b was recorded at 4859 Å. From traces such as these the H_β profile was plotted for various times. The half widths of the profiles yield electron density at the chosen times. It was found for hydrogen at 100 mT

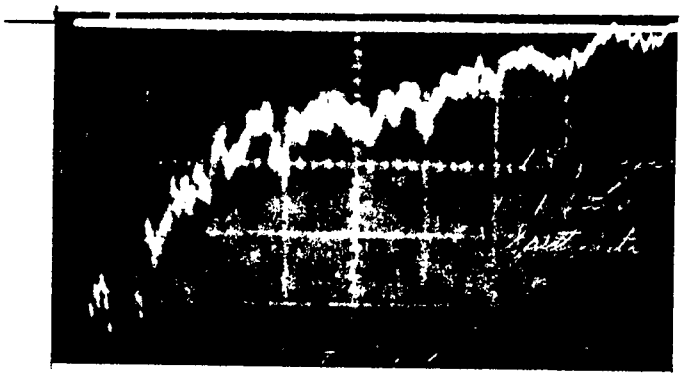

(a) Intensity at λ = 4861 Å of the H_β line:
1 V/cm, 10 μsec/cm

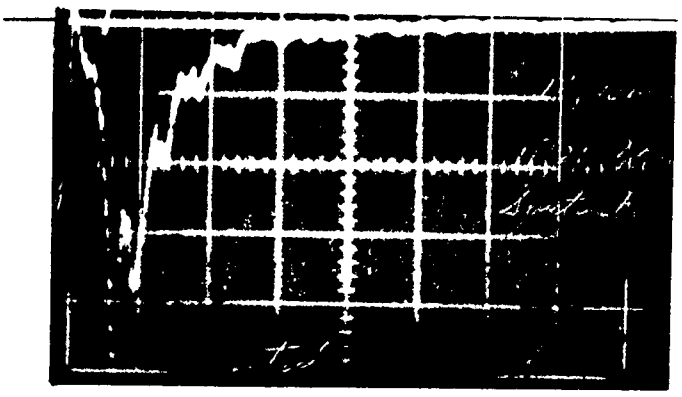

(b) Intensity at λ = 4859 Å of the H_β line:
1 V/cm, 10 μsec/cm

Figure 8. Spectroscopic Measurements of the Preionization Plasma
100 mT hydrogen fill pressure. Spectrometer slit width: 5 μ.

fill pressure that preionization was 74% 10 μseconds after discharge of the preionization and decayed to 16% 20 μseconds later.

6. Switch Gap Monitoring Circuitry
(Jacoby)

During the initial stages of bank operation, problems developed in attempting to fire all four capacitor rows simultaneously. This problem has been temporarily alleviated by gap adjustment, but it was felt that a spark gap monitoring circuit would be a critical bank diagnostic. It would permit a quick determination of any malfunctioning row or rows. As depicted in the capacitor bank description, each row of capacitors is terminated by its own spark gap; each gap is to be monitored and individually timed by the circuit to be described below.

As depicted in Fig. 9, the circuit consists of easily available blocks of digital circuitry. The time resolution is $\pm$0.1 μsec. This is set by the 10 Mhz clock signal which is common to all four channels. In the future, the capacitor bank is to be doubled and it will be noted that full provision for expansion of the circuit to accommodate this has been provided. To return to the circuit operation, the counter begins its operation when a signal from a Hewlett-Packard pulse generator is received. As noted in the description of the bank operation, the HP pulse generator initiates the main bank and hence, the count commences upon its signal. This signal sets the RS flip flop such that clock pulses are permitted to feed into the counter-display unit. Once the spark gap fires, the photodiode picks up the light signal and produces a voltage pulse across a resistor. This signal is amplified to a useful level and passed to a comparator. The comparator produces a low going, TTL compatible signal that is used to reset the RS flip flop.

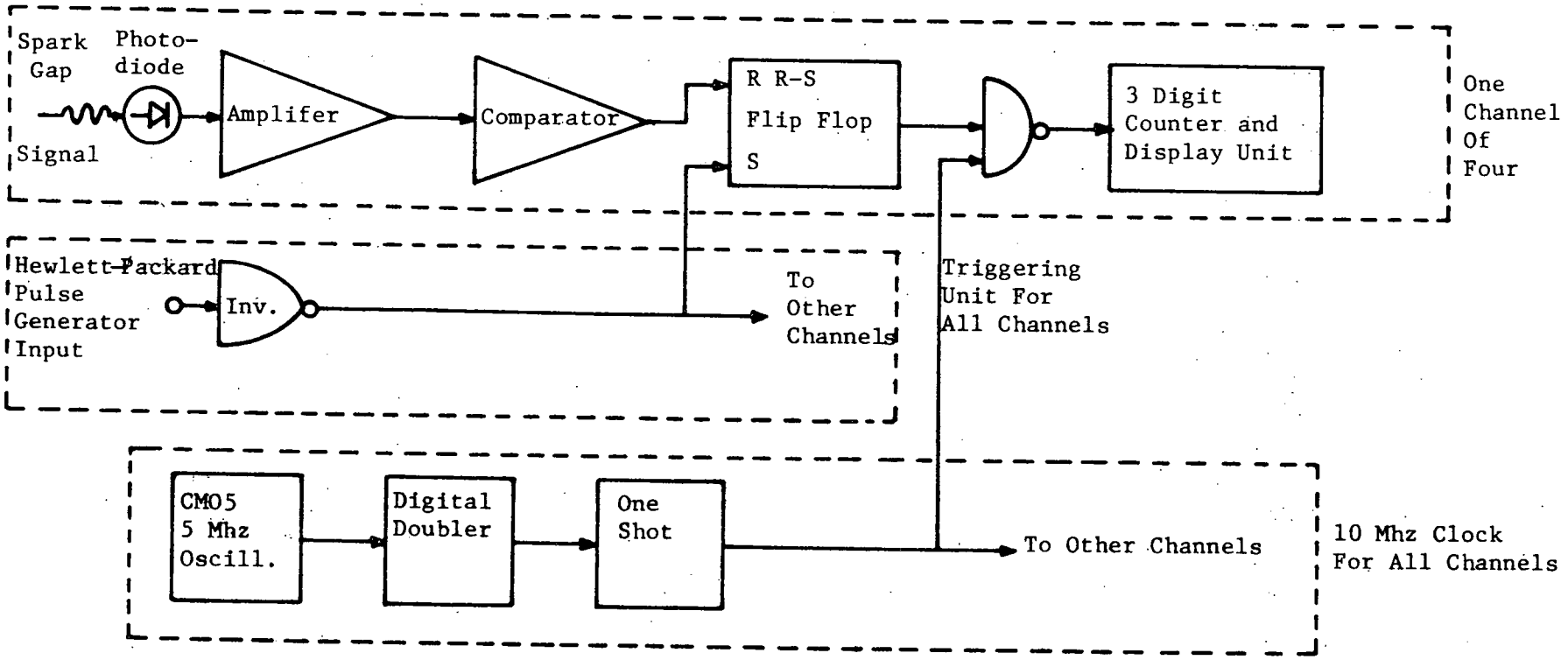

Figure 9. Block Diagram of Switch Monitoring Circuit

With the flip flop returning to its initial state, the clock pulses are cut off from the counter-display unit. The count ceases and the firing time is displayed on the counter-display unit in tenths of microseconds. This is the overall picture of the monitoring circuit for one channel.

The circuitry for one channel has already been bench tested. It performed as expected with the $\pm$0.1 μsec resolution for events. The full four channels are currently being constructed and their testing under actual firing conditions will be started shortly.

7. Completion of Transient Flow Studies on the 25 cm Long Theta Pinch

The detailed progression of the research will be addressed in the renewal proposal.

III. THOMSON SCATTERING DIAGNOSIS OF PLASMA DURING PINCH AND LOSS AT END (Jacoby, Mollo)

A Thomson scattering diagnostic is being developed to determine n_e and T_e properties in the discharge plasma. This diagnostic generally is well documented at this point in time,[7-10] and operation consists of firing a laser pulse into the plasma and examining the light scattered out at roughly 90° to the incident beam. Accordingly, two basic pieces of apparatus are needed for this work: a laser source and an appropriate detector with the plasma dictating the characteristics of both.

How the plasma controls the selection of both laser and detector is detailed in standard references.[7-10] Basically the electron density determines the intensity of light scattered out and the temperature of the electrons fixes the width of the frequency profile of scattered radiation. These two items are coupled with a suitable detection criterion, i.e., what signal levels are needed to rise above noise generated by both plasma and electronics, determine the source and detector.

1. Orders of Magnitude of Plasma Properties and Laser Scattering Apparatus

The plasma to be examined is that streaming out of a theta-pinch. To roughly fix densities and temperatures in the endloss region, the plasma was treated as a source gas undergoing converging-diverging nozzle flow[11] with the discharge tube area used as the fully expanded area. An appropriate throat area was selected from collisional and collisionless theories[12] of the theta-pinch endloss. Thus, using the expected range of plasma parameters in the main discharge as the initial conditions for the gas flowing through the nozzle, an expected range of expansion plasma parameters was found. Then the lowest values of electron density and

temperature were picked as the design criteria. In the main discharge the electron temperature ranges from 290 eV to 150 eV with an expected density of roughly 5 x $10^{16}cm^{-3}$. With these parameters the lowest values for endloss electron density and temperature were $10^{14}cm^{-3}$ and 1 eV respectively.

As mentioned above, the intensity of light scattered is fixed by the electron density. Specifically, the equation for the number of photoelectrons picked up by the detector is

$$N_{pe} = \frac{1}{C_h} \frac{w_i \lambda_i}{hc} r_o^2 LT\eta d\Omega n_e \qquad (1)$$

where T ≡ transmission coefficient of collection and focusing optics

C_h ≡ number of data channels

w_i ≡ energy incident on plasma

λ_i ≡ incident wavelength

h ≡ Planck's constant

c ≡ speed of light

r_o ≡ classical radius of an electron

L ≡ length of scattering volume

η ≡ quantum efficiency of detector

dΩ ≡ solid angle subtended by detector

n_e ≡ density of electrons .

The design parameters chosen were L = 1 cm, T = 0.1, dΩ = 2 x 10^{-3}ster, $n_e = 10^4 cm^{-3}$, η = .02, C_h = 12, and λ_1 = 6943A. Using 30 photoelectrons as the detectability limit, one arrives at an incident laser energy of 7 J. The number of photoelectrons was chosen such that a reasonable output from the detector could be seen, and the shot noise would not overwhelm the signal. The pulse width of the incident laser energy is

determined by two considerations: the signal to noise ratio arising from plasma radiation, and rise times of detectors and associated electronics. Taking a hint from Sheffied[7] a signal to noise ratio resulting from plasma Bremsstralung of $s/n > 10^3$ was used in this calculation. Combining this with temporal resolution of plasma phenomena on the order of 0.1 μsec or better, a pulse duration of 20 nsec was chosen. Finally the beam divergence was selected from constraints on spatial resolution and available aperatures for the main beam focusing optics. This calculation was made using a focusing lens diameter of 2 in. which is somewhat less than the discharge tube diameter, a focused beam diameter of 0.5 mm which was consistent with spatial resolution requirements, and a focal length of 55 cm. Combining these quantities, one concludes that a beam divergence of less than or equal to 3 mrad is required. Thus, the laser system parameters were determined.

With the above specifications on the laser being distributed to laser manufacturers, bids were received from Apollo, Korad, and Holobeam; after a thorough review, the Apollo Laser system was selected. The Apollo system met all the desired specifications, and in a number of details actually exceeded the design criteria. Specifically, the Apollo laser provides a beam energy of 10 J minimum into a total divergence of 2 mrad. The system also provides 7 J into a full divergence of 1.5 mrad. For the pulse duration, a variable setting of from 15 to 30 μsec is provided. The jitter on the pulse timing is $\pm$ 20 μsec which can easily fit into temporal resolution considerations. The RMS deviation in the energy of the laser pulse is less than 10% over a period of 60 sec after the laser capactior bank reaches its full charge. Finally the lifetime of the rods

is expected to be 10^4 shots. The total cost of this system, including installation, acceptance tests, and instruction in usage was within budget constraints.

The detection system exists under a different set of performance constraints. It has to resolve a frequency spectrum with a 1/e width of 20 Å: i.e. the wavelength difference from the center of the spectrum to the value of intensity that is down by 1/e from the center-line intensity. Three types of detectors were considered: PIN photodiode, avalanche photodiodes, and photomulitpliers. Due to the low intensities scattered back and the need to boost the signal above the Johnson noise of the load resistor, the photomultiplier was selected. The tube chosen was a RCA 7265 due to its internal amplification and frequency response to light. For the rise time needed to resolve the 20 nsec laser pluse a load resistor of 10 Ω was chosen when the tube capacitance was taken into account. Using these values with the tube characteristics, a 0.135 V output signal is expected. The means of examining the spectral width is to use two line filters 0/10 Å bandwidth on the low side of 6943 Å. They are to be centered at 6938 Å and 6928 Å. Presuming that the electron distribution is Maxwellian, the spectral width of the scattered radiation is derived by ratioing the signals from the two channels.[8] This presumption is reasonable for the electrons due to their fast collision time and hence swift thermalization.[13] Thus, the two channel detection set up is as follows: the light is coupled out of the plasma by a two lens focusing arrangement, it then is incident upon a beam splitter which divides the beam equally between the two channels, the divided light then falls on the 10 Å line filter, and behind the

filter lies the photomultiper tube. The tube uses the 10 Ω load to develop voltage and this voltage is displayed directly on a 100 Mhz oscilloscope.

In addition to determining the electron temperature, Thomson scattering also permits a measurement of the electron density. This is to be done using two calibration schemes. In one method an absolute determination of the transmission coefficients of the optical components will be made by intensity measurements using a calorimeter on both the pulse before and after transmission through the optics. Then through a theoretical consideration of the intensity scattered out, the electron density is determined. The other means of calibration is the comparison of the Rayleigh cross-section for scattering of neutral N_2 molecules with that for Thomson scattering.[7-9] The ratio of the two cross-sections is accurately known. Thus, the electron density can be determined when the density of the neutral N_2 used is known and the relative intensities of the scattered signals are known.

Beside the detector and laser source, a description of how the beam is arranged with respect to the plasma and how it is eliminated after passing through the plasma is necessary (Fig.10). The beam is to be shot in axially and focused on the scattering volume by a two lens set-up. This lens system will consist of a diverging-converging arrangement. After passing through the plasma, the beam will be absorbed in a dump consisting of two plates of Corning CS4-72 blue glass.[8] Behind the beam dump will be a PIN photodiode that will monitor the laser pulse shape.

The above description provides a summary on the laser system and detection apparatus being developed for Thomson scattering. Overall,

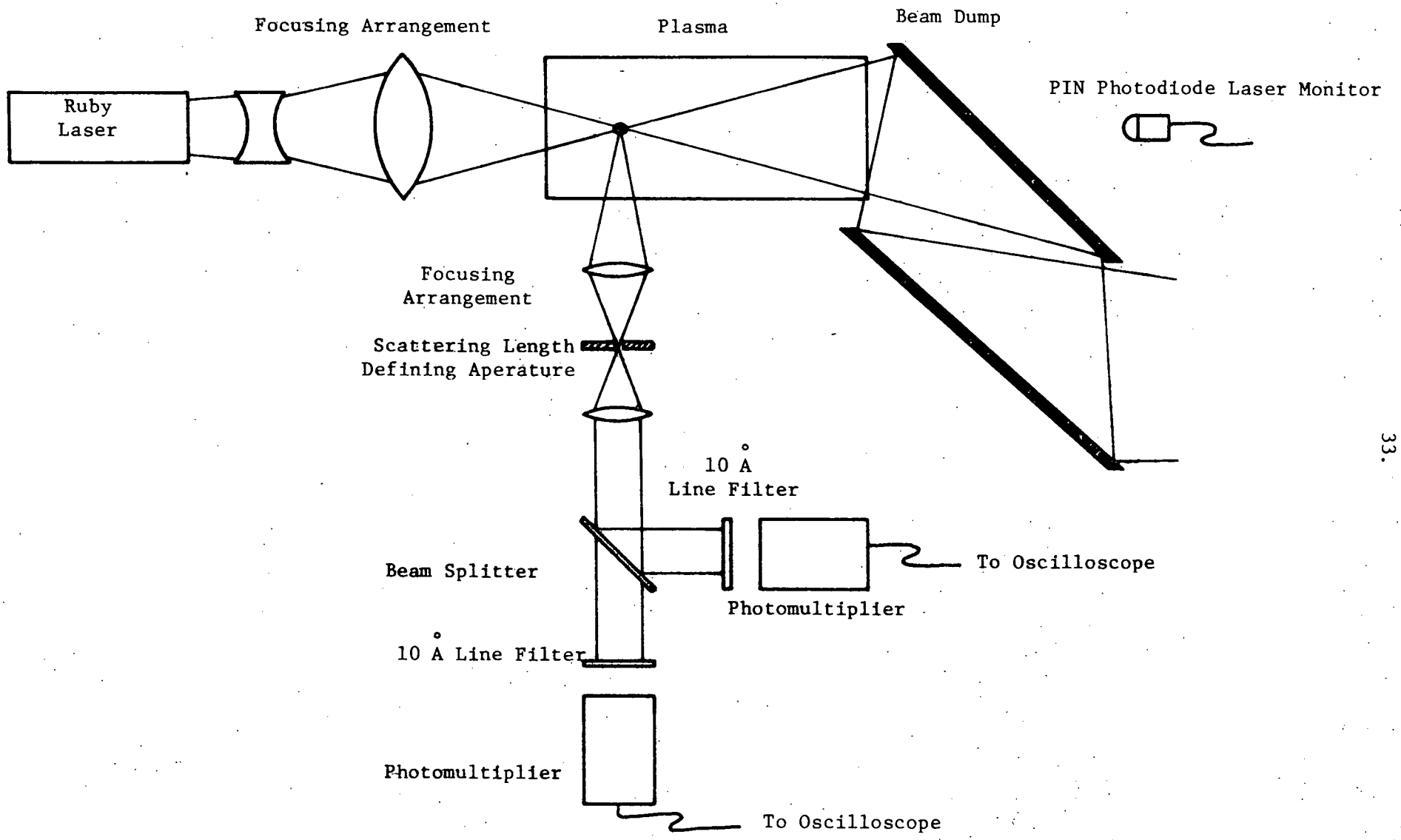

Fig. 10 Laser Scattering Experimental Set Up

the system is as simple as it can be without sacrificing information. Even so, the densities and temperatures that are expected in the endloss region should be quite acessible to measurement using this system.

2. Description of Lower Density Resolution with ND-YAG-Glass Lasing

The ruby laser detailed earlier actually lies in a region of poor sensitivity on the detector output curve. One would like to be able to have a source line that lies near the maximum output of the detector response in order to gain the full benefit of the detector spectral sensitivity. A possibility that has been considered is a Nd-Yag laser source in combination with a frequency doubler.

The Yag laser has an output at 10,600 Å. Frequency doubling brings this to 5300 Å, and upon examining the spectral response curves for the RCA 7265 photomultiplier the quantum efficiency at 5300 Å is found to be 0.11. For the ruby wavelength of 6943 Å the quantum efficiency is only 0.023. For the same detectability criterion (i.e. same number of photoelectrons ejected from the tube's cathode) it can be shown that

$$(w\lambda\eta)_{ruby} = (w\lambda\eta)_{doubled\ Yag} \qquad (2)$$

Accordingly, employing the parameters of the ruby system shown earlier, only an energy of 2 J need be incident on the plasma to achieve equal scattered energy when a doubled Yag system is used. This, however, does not take the doubler efficiency into account. Using a characteristic doubler efficiency of 50%, it can be seen that an energy of 4J output is needed from the Yag laser. This value compares with the 7 J needed by a ruby laser to perform the same as the Yag.

Another interesting aspect of the Yag system is revealed when the limits of density resolution are examined for the ruby and Yag lasers.

This particular criterion is of importance for the endloss studies since minimum densities in the expanded flow regime are only roughly estimated. What experimental number densities will be found is another question. Again we can compare the systems. The following equation is useful in this comparison:

$$(w\lambda\eta n_e)_{ruby} = (w\lambda\eta n_e)_{Yag} \tag{3}$$

For the same incident power, n_{eYag}/n_{eruby} is about 0.27, or the Yag system can resolve densities a factor of 3.7 below that of ruby. Again taking the doubler efficiency into account, one is actually defining a factor of 1.85.

In discussing density resolution, it can immediately be seen that the density which can be measured is related to the source energy by

$$w_i n_e = \text{const.}$$

Consequently, to go lower than the aforementioned ruby design of 10^{14}, a proportionately higher energy output from the laser is required. A ruby laser oscillator-amplifier system is limited to around 10 to 12 J. Nd-Yag oscillator-amplifier combinations have a potential to generate much higher energies.

Of course, energy cannot be continually dumped into the plasma at increasing values without appreciable heating effects occuring. This invalidates the temperature measurement and hence renders that aspect of Thomson scattering useless. To avoid this uncertainty, it can be shown that after choosing an acceptable limit on heating the plasma, the following holds true:

$$\left(\frac{w_i \lambda_i^2 n_e}{T_e^{5/2}}\right)_{Yag} = \left(\frac{w_i \lambda_i^2 n_e}{T_e^{5/2}}\right)_{ruby} . \tag{4}$$

Now presuming the same density in both cases and using the fact shown above that $w_{i_{ruby}}/w_{i_{Yag}}$ equals 1.85, a factor for temperature resolution can be arrived at. Performing the calculation gives a value of $T_{e_{ruby}}/T_{e_{Yag}}$ of 1.59. Accordingly the Yag system can resolve lower temperatures than the ruby system by that factor.

With these considerations in mind queries were made to laser manufacturers concerning powers available by interchanging rods in the ruby system that could be purchased from them. With the Apollo laser, it was found that 2 J could be generated by a Nd-Yag oscillator with a glass amplifier. Obviously net energy does not even start to approach the capabilities of the ruby laser. However, when another glass amplifier is added, a 10 J output from a Yag system can be generated. Performing calculations on density and temperature resolutions for a 10 J ruby and 10 J Yag system using the 30 photoelectrons per channel detectability criterion (actually a value of 60 photoelectrons was used in the calculation in order to take into the fact that the beam splitter in the detector system drops the scattered by one half), it was found that the Yag system outperforms a comparable ruby system. The results are summarized in the table below:

System	Ruby	Nd-Yag
Energy of laser	10 J	10 J
Lowest density accessible to measurement	$6 \times 10^{13} cm^{-3}$	$3 \times 10^{13} cm^{-3}$
Lowest temperature accessible to measurement	0.97 eV	0.422 eV

The temperature ratio of 2.3 which is greater than 1.59 results from the fact that formula (4) ignores a factor of $\ell n \Lambda$ on both sides for simplicity.

The advantages of a Nd-Yag laser scattering experiment can be summed up as follows. First, the effectiveness of the laser energy of the Yag is a factor of 1.85 over that of the ruby. Secondly, the temperature resolution of the Yag is a factor of at least 1.59 over that of the ruby. Indeed, at the low temperatures examined in this paper the temperature measurement improvement is actually a factor of 2.3. The development of such a laser system will not be considered in the renewal proposal as the cost of required items does not appear to be consistent with possible gains at this time.

3. Description of Possible New Diagnostic Using Nd-Glass

As discussed previously, a Nd-Yag laser holds certain advantages for the Thomson scattering diagnostic. To maximize the effectiveness of such a system requires two Nd-glass amplifiers to boost the Yag oscillator's energy to an acceptable value. This is standard scattering diagnostic technique but is somewhat of a wasteful process, since the glass amplifer has a broad bandwidth of about 50 $\mathring{A}$ FWHM while the Yag oscillator has a narrow bandwidth of around 5 $\mathring{A}$ FWHM. Consequently, only a narrow fraction of the amplifying ability of the glass is being used. A replacement of rods in the ruby system with two Nd-glass rods permits operation in a regime of from 10 to 50 J output in a single pulse which means densities on the order of $6 \times 10^{12} cm^{-3}$ could be detected. In this context a more efficient scheme in terms of energy output would be a glass oscillator coupled with a glass amplifier; for standard Thomson scattering, this would have an unacceptably broad bandwidth.

However, if this type of system is considered, the broad bandwidth of the laser output may be successfully taken into account in a new

diagnostic scheme. Again presuming the doubling system technique, the bandwidth of 50 Å FWHM is halved since frequency doubling means wavelength halving. In a 1eV plasma, which is of the variety expected in the endloss region, the doppler bandwidth in the scattered light due to an infinitesimally narrow laser line is also about 25 Å FWHM. In comparison the Yag after being frequency doubled has a bandwidth of 2.5 Å FWHM. Apparently this is sufficiently narrow to safely ignore its effect on the doppler broadened spectrum. Obviously, though, this is not the case with the glass system.

Consequently, we have examined what effects a broad source has on the scattered spectrum. Approximating the laser line as a Gaussian gives

$$W_i(\lambda) = W_o e^{-(\lambda - \lambda_o/\lambda_{1/e})^2} \tag{5}$$

where $\lambda_{1/e}$ is the 1/e th half bandwidth of the laser which is related to the full width at half maximum by

$$\lambda_{1/e} = \frac{\text{FWHM}}{2\sqrt{\ell n 2}}$$

Here $\lambda_{1/e}$ is 15 Å. Now the plasma will scatter back radiation according to

$$\frac{dN_P}{d-t}\, d\lambda_s d\Omega = \frac{P_i r_o^2 n_e L T d\Omega \eta}{h_c 2\sqrt{\pi}\, \sin\theta/2} [\hat{s} \times (\hat{s} \times \hat{E}_{10})]^2 \frac{c}{V_e} e^{-(\lambda - \lambda_\ell/\lambda_{1/e})^2} d\lambda \tag{6}$$

This equation presumes a delta function laser line centered at λ equals λ_ℓ. Thus, the effects of a broad laser line can be taken into account by convoluting equation (5) with equation (6) or

$$\frac{dN_P}{dt}\, d\lambda_s d\Omega = C \int_o^\infty e^{-(\lambda - \lambda_\ell/\lambda_{1/e})^2} e^{-(\lambda_\ell - \lambda_o/\lambda_{1/e\ell})^2} d\lambda_\ell$$

$$\frac{dN_P}{dt}\, d\lambda_s d\Omega = c' e^{-(\lambda - \lambda_o)^2/(\lambda_{1/ep}^2 + \lambda_{1/e\ell}^2)}$$

Thus, the effect of the laser bandwidth is merely to add to the doppler broadening in a root-mean-square fashion. Quite obviously if the laser bandwidth is known accurately, then its effects on the scattered radiation frequency profile can be easily subtracted out. Thus, the broadening due to temperature effects alone can be recovered.

To take the broadened laser output into account properly, one would actually have to use a Lorentzian profile for the laser line. However, this gets analytically complex, and it is easier to see the physical effect by using a Gaussian as an approximation to the Lorentzian. An investigation on the full effects of the Lorentzian is currently being pursued both numerically and analytically in an attempt to place limits on the error introduced by the Gaussian approximation.

As noted above, since an order of magnitude improvement in density resolution (from $6 \times 10^{13} cm^{-3}$ down to $6 \times 10^{12} cm^{-3}$) is possible with this system, it is felt that this research should be pursued. However, further analytical studies must be done before procurement of any equipment is considered. This is expected to be a specific topic for consideration in any future research proposals.

IV. TWYMAN-GREEN INTERFEROMETERIC STUDY OF LOSS FROM 10.5 CM THETA PINCH (Freeman, Mollo)

The studies of loss from the ends of theta pinches described above and in the research proposal have concentrated on new, local measurements of plasma properties at the ends during the loss events. However, there is a need to diagnose the change in the total particles contained within the pinched column; this has normally been carried out with some form of interferometry which averages properties over the column to indicate a line density. The change in line density is used to evaluate particle loss time, τ.[14-16] During the reporting period, research work has been carried out to develop a method of diagnosing total column density, and accomplishing the task within our unique constraints. First, as lasers appropriate for standard pinch interferometry would not be available, a method which used an inexpensive He-Ne CW laser was found acceptable. As such a laser would also be necessary for alignment of the ruby laser described above, its acquisition served two purposes. Second, as the progress of the studies of the 25 cm pinch would not allow satisfactory scheduling access for the development of an inteferometer diagnostic, it was decided to design and construct a small($\sim$10 cm), low power($\sim$10 μF) highly reliable theta pinch to be used as a plasma source for testing the pinch interferometry, as well as a test device for circuit components and other diagnostics. The discharge device, the interferometry diagnostic, and some results of its application will now be discussed. This work will be completely detailed in an M.S. thesis and technical report to be completed in the near future.

1. Description of the 10.5 cm Pinch Apparatus

The pinch coil itself was 10.5 cm long, 11.11 cm in diameter, and 0.159 cm thick aluminum. The coil was fitted around the middle of three

standard 4 in. pyrex tubes fitted together to make up the discharge chamber. Each pyrex tube was 30.25 cm long and had an inside diameter of 10.16 cm. The tube length of 62.25 cm was used so that any optical elements which had to be placed in the system could be positioned far enough away from the discharge so that their surfaces would not be damaged by streaming plasma. Special end flanges were constructed to hold the optics and diagnostics in place.

The discharge current was produced by two capacitors connected in parallel and charged to 11.0 kV. The combined capacitance and inductance of these capacitors were 9.85 μF and 20 nH respectively. The connection between capacitors was a parallel plate transmission line with total inductance of 16.5 nH. The system was switched on by use of an open air gap, around which helium was bled in order to breakdown the gap. The inductance of the gap was found to be approximately 42.7 nH.

Diagnostic devices used to investigate the properties of the discharge and plasma were a simple current loop (Rogovski coil), and an axial magnetic field probe. From the magnetic field probe data, sheath velocities, pinch times and approximate percent mass pick up were calculated. All calculations were compared to "snowplow" theory. This model of pinch collapse was fitted to best predict properties of the collison dominated plasma with fill pressures of hydrogen between 40 and 65 mT.

The current wave form was found to be damped sinusoidal in nature. The equation which represents this wave form is $I = v_o \omega c e^{-\alpha t} \sin \omega t$ where $\alpha = 4.446 \times 10^6 \text{sec}^{-1}$ and the other parameters are listed in the table below. The magnetic field also was damped sinusoidal in nature and was calculated using the Biot-Savart Law.

Theta-pinch characteristics

Voltage (kV)	11.0
Capcitance (μF)	9.95
Source inductance (nH)	79.2 nH
Coil length (cm)	10.5
Coil diameter (cm)	11.11
Inside radius of discharge tube (cm)	10.16
Coil inductance	81.3 nH
Maximum current (amps)	
First half cycle	7.893×10^4
Second half cycle	6.621×10^4
Maximum magnetic field (kG)	
First half cycle	6.487
Second half cycle	5.441
E_θ (at tube ID) (v/cm)	
First half cycle	1.48×10^1
Second half cycle	1.24×10^1
Half cycle (μsec)	3.95

As will be seen below, the E_θ generated by the discharge system was sufficient to preionize gas during a first half-cycle and to reproducibly create collapsing current sheaths during the second half-cycle over a fill pressure range from 20 mT to 200 mT hydrogen. Snowplow theory was used to get estimates on initial densities, temperatures and pinch times before the start of adiabatic compression.[17] These estimates are listed on the table below for the various fill pressures of hydrogen gas which were investigated:

Fill Pressure (mT)	Density n_p (cm^{-3})	Temperature $T_p = T_i + T_e$ (eV)	Pinch Time (μsec)
40	1.806×10^{16}	9.961	0.8790
50	2.257×10^{16}	8.909	0.9294
65	2.935×10^{16}	7.814	0.9925

2. Interferometer Description and Layout

The interferometer constructed was of the double pass Twyman-Green type. This interferometer was recently used by Molen[18] to study the

changes in line average electron density of a decaying plasma. The advantages of this form of interferometer are that both temporal and spatial changes in density can be investigated simultaneously, in a simple, inexpensive system. With other types of interferometers currently being used in plasma research, only temporal or spatial data can be taken on one discharge.[14-16] Another advantage is that since the Twyman-Green interferometer is a double pass device, it is twice as sensitive to changes in density than a single pass device such as a Mach-Zehnder interferometer.[14]

a. Overall diagnostic layout

The experimental layout (Fig. 11) was for a Twyman-Green interferometer which made a double pass through the plasma before interfering with the reference beam. The interferometer was lined up parallel to the axis of the theta pinch discharge tube. The light source was expanded and collimated to a beam diameter of 1.905 cm. The beam traveled through an isolation system then into a beam splitter where approximately half of the light was transmitted into the discharge tube and the other half was reflected onto the reference leg of the interferometer. Both beams were then reflected back onto themselves by means of a totally reflecting mirror situated at the end of each leg. The beams were recombined at the beam splitter and by use of a third mirror, the recombined beam was reflected, passed through a line filter and into the detection system.

When the optical path length of plasma changes by a factor of $\lambda/2$ one fringe shift occurs. The number of fringes to be seen was

$$x(t) = \text{number of fringes} = \frac{\text{difference in optical path length between vacuum and the plasma}}{\text{wavelength of light source } (\lambda_o)}$$

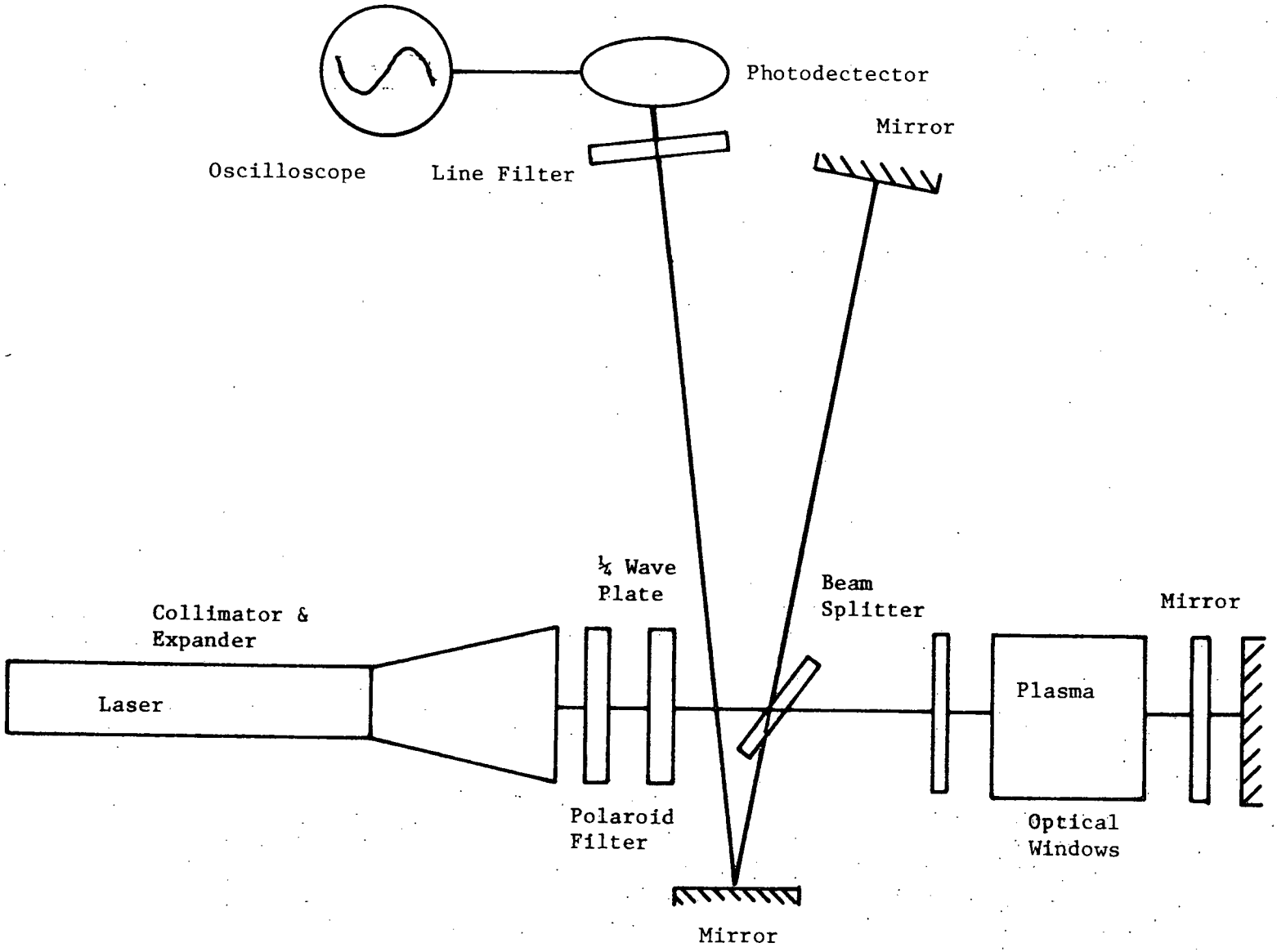

Figure 11. Twyman-Green Interferometer Layout

The optical path length = $\mu\ell$ when μ = refractive index and ℓ = total distance traveled by laser beams in the medium. For a vacuum $\mu = 1$, but for the plasma it has been shown[14] that $\mu_p \simeq \frac{1}{2}\frac{w_p^2}{w^2}$

w_p = plasma frequency = $[(4\pi e^2/m_e)n_e]^{1/2}$

e = electronic charge

m_e = mass of electron

n_e = electron density

w = laser frequency = $2\pi c/4$

c = speed of light

λ = wavelength of laser being used = 6328Å;

with the appropriate numbers, it was found that

$$\mu_p = 1 - 4.478 \times 10^{-14} n_e \lambda_o^2 .$$

Since the optical path length can be written as $\mu\ell_T = \int_o^{2\ell} \mu d\ell$ (upper limit of integration is 2ℓ instead of ℓ because system is a double pass-type). The number of fringes expected can be written as

$$x(t) = \frac{\int_o^{2\ell} \mu_{vacuum} d\ell - \int_o^{2\ell} \mu_{plasma} d\ell}{\lambda_o}$$

or

$$\bar{n}_e = \frac{1.117 \times 10^{13}\ \dot{X}(t)}{\lambda_o \ell}\ cm^{-3}$$

where ℓ = length of plasma column.

b. Equipment

The laser was a helium-neon laser model 3224H-PC made by the Hughes Aircraft Corp. The usable power output was measured at 6.9 mW on a Spectra Physics model 401B power meter. Tests showed that there was no visible drift in power output over a three hour testing period. This was desired so that the detector would always see the same intensity

beam. The beam divergence was 1.0 m rad and the diameter was 0.8 mm at $1/e^2$. The laser was linearly polarized so that an inexpensive optical system could be fabricated to isolate the laser from light reflection back into it from the two legs of the interferometer.

The collimater-expander was a Spectra Physics model 331 collimating lens and Spectra-Physics model 332 spatial filter, which had a 15 micron aperture situated between the two. The spatial filter consisted of a converging lens with a focal length of 12.8 mm, which focused the beam to approximately 13 microns spot size at the pin hole. The beam then expanded to 1.905 cm and was collimated by the collimating lens, with the power decreased to 4.8 mW.

The isolation system was fabricated so that light from the two legs of the interferometer could not return into the laser. For if any light was to enter the laser cavity from an external mirror it could couple with the laser cavity and could change the characteristics of the output. The isolation system consisted of a polaroid filter and a mica quarter wave plate.

The table below lists the important parameter of the optical components used:

	Diam. (in)	coating	material	flatness	% refl.	% trans.	% loss
Beamsplitter	2	dielectric	fused silica	$\lambda/10$ with 30 min. wedge	52.4	45.7	1.9
Mirrors	1	dielectric	fused silica	$\lambda/10$ with 30 min. wedge	99.44	-	0.56
Windows	1	none	fused silica	$\lambda/10$	-	94.6	5.4

The detector consisted of circuitry supporting an EG&G SGD 040A fast silicon photodiode which had a 0.815 mm^2 photosurface. The output

of the diode was amplified by an CA 30157 A operational amplifer (see Fig. 12). The load resistance seen by the diode was designed to be 2.2 kΩ which gave the diode a 20 MHz bandwidth. The gain of the amplifer was approximately 14 dB with 4 dB bulge centered around 15 MHz. The total bandwidth of the amplifer was 25 MHz.

The detector output was monitored by an oscilloscope so that a record of the passage of fringes with respect to time could be acquired. Spatial resolution was achieved by repositioning the detector, between discharges, at different radii with respect to the plasma column. Since only one detector has been developed to this point, one cannot achieve both spatial and temporal time rate of change of line average electron density simultaneously.

3. Magnetic Field Studies of Implosion Phase of 10.5 cm Pinch

A magnetic field probe[4] was used to investigate the plasma implosion phase of the theta pinch device. B and $\dot{B}$ measurement of the axial field were made keeping the radial position constant but varying the position in the axial direction so that it could be seen what manner of pinching was achieved near the ends of the theta pinch coil. Also, B and $\dot{B}$ measurements were taken at several radii at the axial center of the pinch coil in order that estimates of percent mass pick-up by the current sheath, pinch times, and average electron densities could be calculated.

The measurements made at several axial positions at 50 mT fill pressure, showed reproducible dynamic collapse of a plasma column near the axial center of the device but as one moved toward the outer edge of the coil the collapse became less sharp (see Fig.13). At the axial center of the coil the data showed that after the current sheath formed,

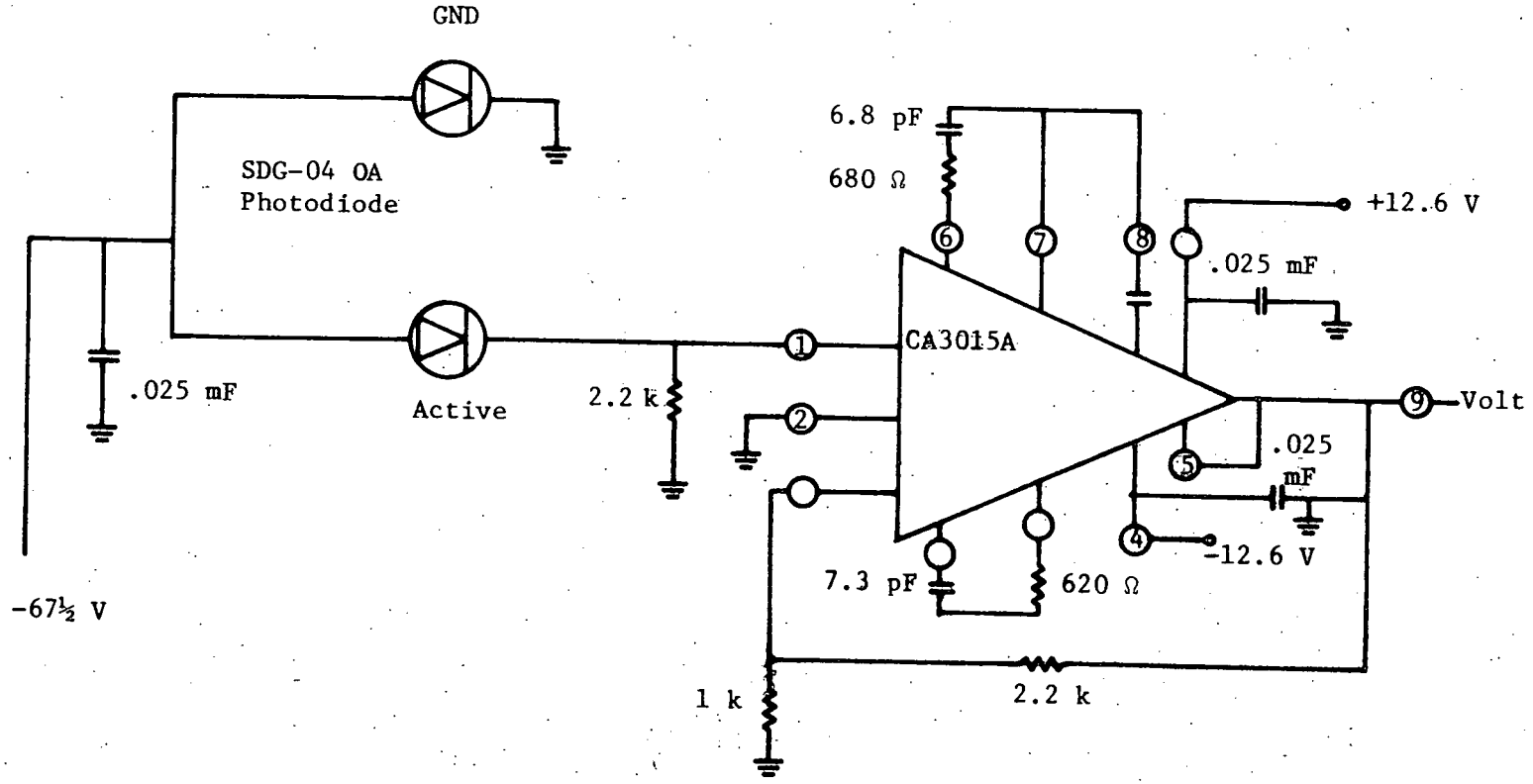

Figure 12. Fringe Photodectector Circuit

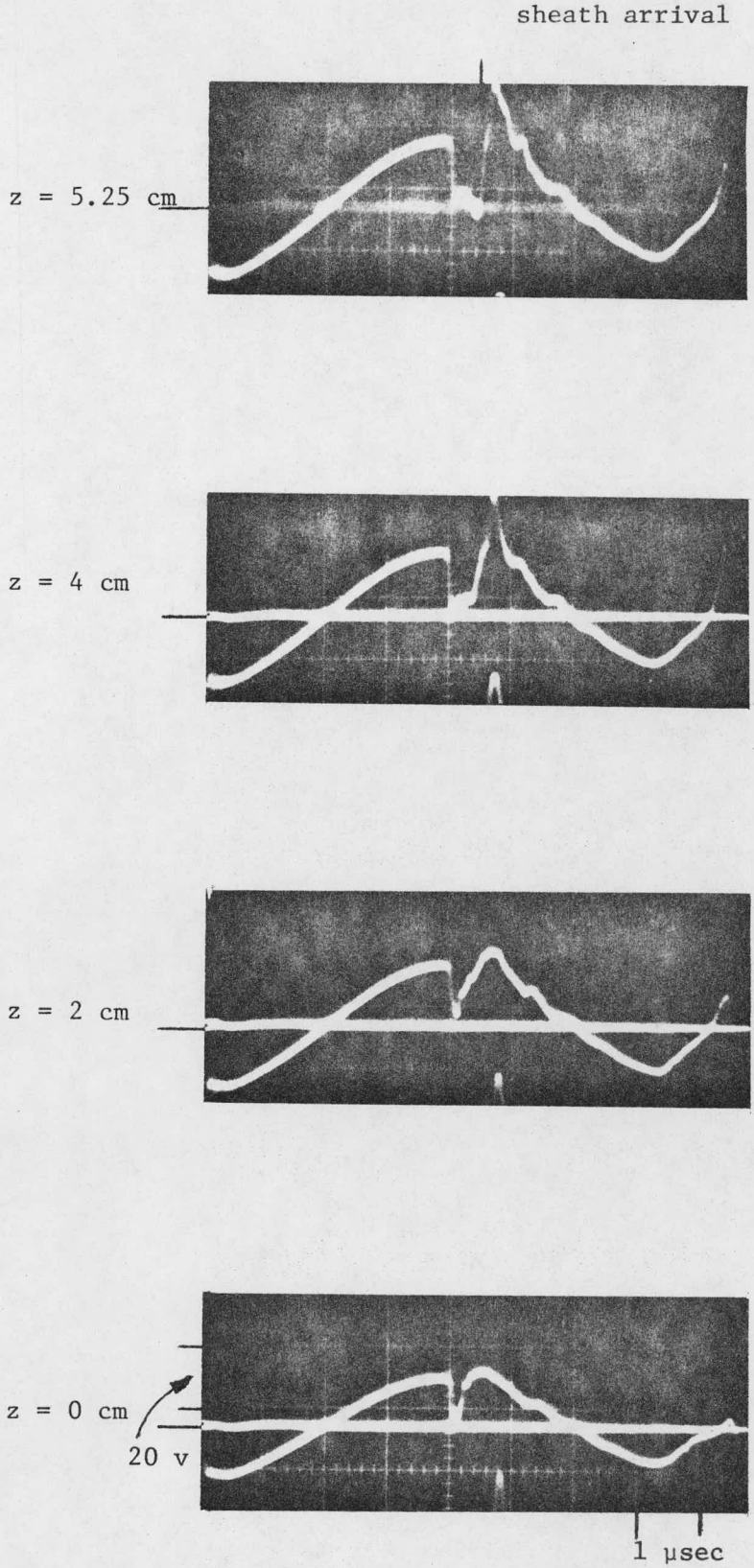

(Note: z = 5.25 cm defines axial center of coil)
r = 0 cm defines radial center of coil)

Figure 13. Axial Survey of the Theta Pinch Magnetic Field, $\dot{B}_z$
50 mT hydrogen fill pressure, r = 2.54 cm

the plasma became diamagnetic, the magnetic field remaining zero until the sheath passed over the probe at which time the collapsing magnetic field would be sensed.

The data taken at different radii (see Fig. 14) were used to map out the imploding trajectory of the sheath. A plot of the position of the sheath versus time for 40 mT, 50 mT and 65 mT fill pressures was carried out. From the simple force balance it can be shown that

$$\frac{B^2}{8\pi} = \alpha\, m_i n_o [v_s^2 + (\frac{b^2 - r^2}{2r})\frac{dv_s}{dt}]$$

where $\alpha \equiv$ fraction of mass picked up by sheath

$m_i \equiv$ mass of ions

$n_o \equiv$ fill density

$b \equiv$ inner radius of discharge tube

$r \equiv$ radial position of sheath

$v_s \equiv$ velocity of sheath

In these calculations average magnetic fields, velocities, accelerations and sheath positions were used. Velocities and accelerations were determined from the plot of sheath position vs. time. It was found that the percent mass pick-up was between 75 and 83 percent.

Effective pinch times also were obtained from these plots; values obtained were 0.820 μsec for 40 mT fills, 0.915 μsec for 50 mT fills and 0.956 μsec for 65 mT fills. When compared with snowplow calculations of pinch times presented alone, it was observed that experimentally found times were slightly less than predicted times, but in reasonable agreement.

When the probe was positioned near the radial center, plasma oscillations in the plasma column were identified by the magnetic field

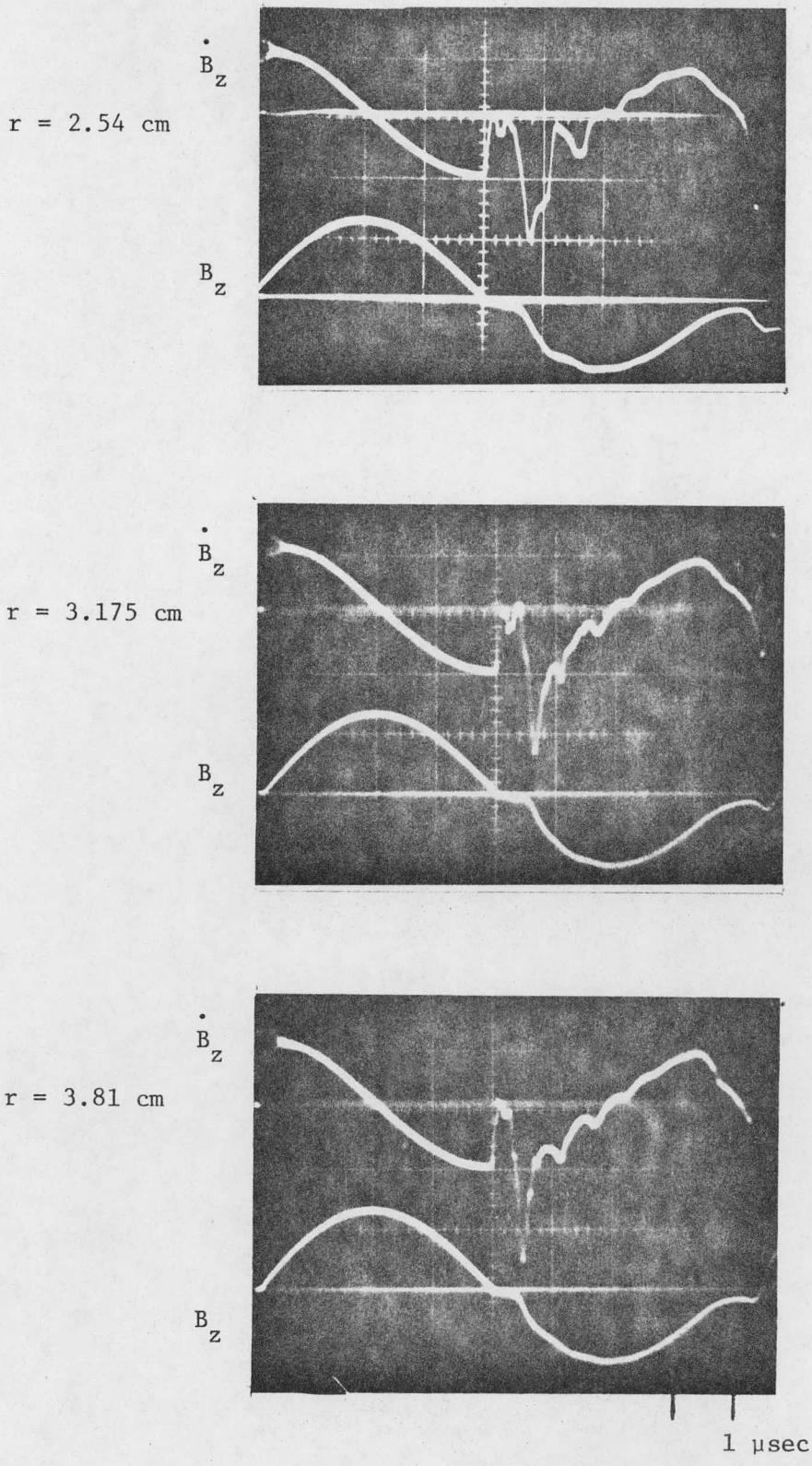

Note: z = 5.25 cm defines axial center of coil
r = 0 cm defines radial center of coil

Figure 14. Radial Survey of Axial Magnetic Field, B_z and $\dot{B}_z$
50 mT hydrogen fill pressure, z = 5.25 cm

probe (see Fig.15). From the frequency of oscillation, estimates of electron density can be calculated. It has been shown[19,20] that the mass per unit length in a plasma is related to the period of plasma oscillations:

$$M = \frac{B^2 \tau^2}{4\pi^2}$$

where, $\tau \equiv$ period of oscillations

$M \equiv$ line mass of plasma (mass per unit length)

$B \equiv$ confining magnetic field strength

Also, for a hydrogen plasma quasineutrality holds, so

$$n_e = n_i = \frac{M}{\pi r_p^2 m_i}$$

where $r_p \equiv$ plasma radius after the implosion phase. Therefore

$$n_e = \frac{B^2 \tau^2}{4\pi^3 r_p^2 m_i}$$

Calculations indicated densities of the order $1.7 \times 10^{16} cm^{-3}$ for 40 mT fills, $1.9 \times 10^{16} cm^{-3}$ for 50 mT fills and $2.3 \times 10^{16} cm^{-3}$ for 65 mT fills. These values are less than those predicted by the 100 percent sweep snow-plow model, but reinforce the prediction of a percentage mass pickup by sheath momentum balance.

The above results indicate that the 10.5 cm theta pinch device developed for this experiment created a plasma sheath collapse which was reasonably intense and reproducable. Also, it can be concluded that the snowplow model predicts the characteristics of the plasma with reasonable accuracy. The state and behavior of the plasma to be probed with the Twyman-Green interferometer can be concluded to be known and of an appropriate density for these studies.

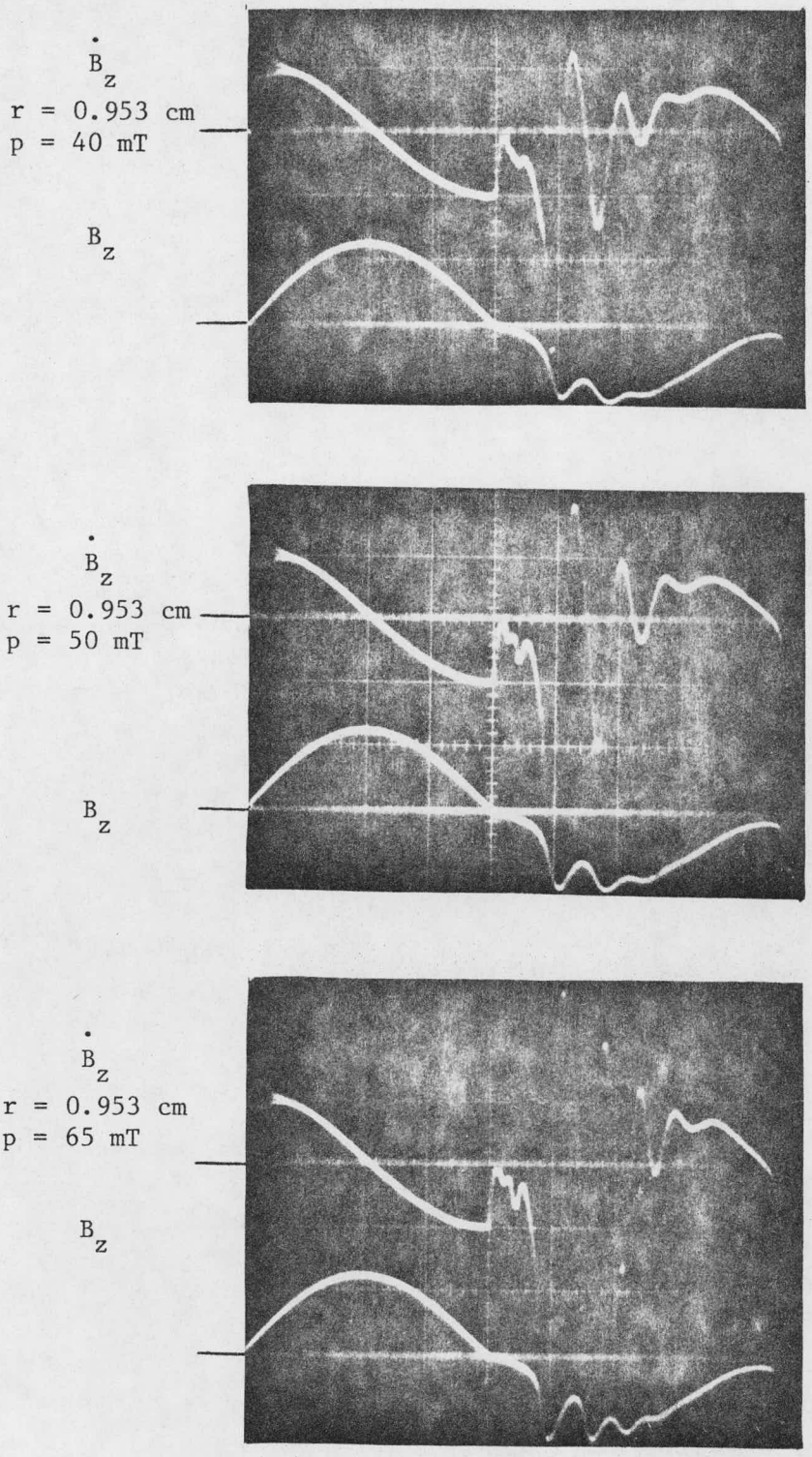

(Note: z = 5.25 cm defines axial center of coil)
r = 0 cm defines radial center of coil)

Figure 15. Magnetic Probe Survey of Plasma Oscillations
Probe position: z = 5.25 cm; 1 μsec/cm

4. Twyman-Green Interferometer Data and Preliminary Interpretation

Prior to the attempt to record interferometer records of the dynamics pinch discharge, a number of tests were made to record reference nulls. First, with ambient gas fill but with no laser light filter, plasma light was recorded by the photodetector; it was on the order of expected signal level. With a filter added, during the plasma discharge the null signal was a fraction of a millivolt. With laser light and no plasma, the only signal was a definable low frequency drift due to room vibrations; this can be accounted for in data interpretation.

Interferometric data indication of plasma events were taken for fill pressures of 50 and 65 mT, at three radial positions (r = 0, 3.5 and 7.25 mm). Figure 16 is an example of photodetector output at r = 0 for a fill pressure of 50 mT. Initiation of the signal is the beginning of the second half-cycle of the discharge which has a duration of 4 μsec. Pinch time is about 1 μsec. The peak to peak deflection of the detectors output was found to have been 6.5 mV and calculations have shown the expected deflection to be approximately 7 mv if the laser beam were suddenly to be blacked out. The oscillatory output of the photodetector can be interpreted as being caused by a dark fringe passing over the active area of the photodiode, with a fringe representing a change in average line density of 1.77×10^{17} electron/cm^2.

Interpretation of single-trace data such as that presented above is not absolute, but it will be discussed relative to the physical events occuring in the plasma column. During the second half cycle of interest four processes are active, all of which cause changes in line density. Following a 1 μsec implosion, there is a 1 μsec period of time where

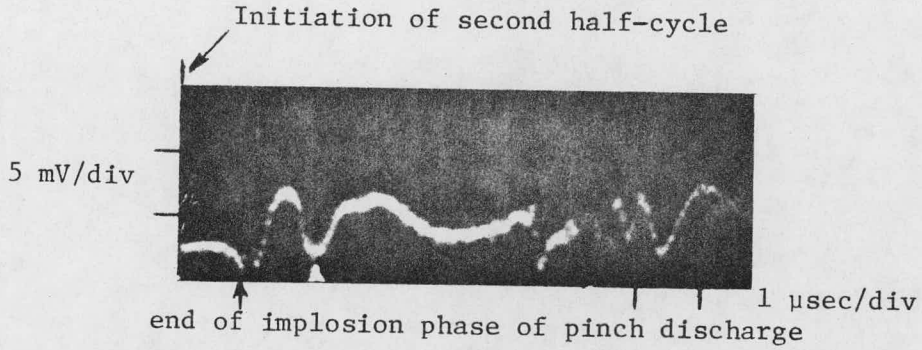

Figure 16. Photodetector Output During Second Half Cycle Pinch (50 milliton fill pressure, r = 0)

adiabatic compression and loss from the ends take place simultaneously. The adiabatic compression would tend to increase the line density, while the end loss would tend to do the opposite. After peak field, the decrease in B would cause the plasma column to expand, thus decreasing the line density; during this expansion the loss from the ends would continue. Also, the plasma column did show signs of radial oscillation, but these can easily be accounted for. However, the axial magnetic field probe studies did show that a plasma column was not formed along the entire coil length. It was seen that the plasma column length was somewhere under 10.5 cm, about 6 cm. Since $\overline{\Delta n_e}$ = (the change in average time density/the length of the plasma column) the amount of density change that one fringe corresponded to could not be considered accurately known. This problem has been recognized in all interferometer studies of theta pinches.

An approximate estimate of the number of fringes produced by loss from the ends of the device can be made by observing fringe behavior during the two microseconds after the implosion phase of the pinch. As peak magnetic field is reached after the first microsecond and the magnetic field waveform is symmetrical, the strength of the magnetic field is equal at the start and finish of the 2 μsec period. Therefore, if no end loss was to have occurred the observed density of the plasma should be the same at these two times, and the fringe position would be the same. The difference between the detector output at these two times can be taken to be caused by loss from the ends. It will be noted that the number of fringes caused by loss from the ends during this time could be estimated with reasonable accuracy to be less than one. One fringe

represented at least a 90 percent reduction in electron density in this case.

Following the interpretation scheme outlined above, it was found that for 50 mT fill pressures the number of fringes associated with end loss was approximately 0.45. This corresponded to an average line density change of 7.97×10^{16} electrons/cm^2. Also it was assumed that the plasma column was 6 cm long, this assumption led to the change in average electron density to be calculated at 1.33×10^{16} electrons/cm^3. Assuming the change in electron density due to end loss varied as $\overline{n_e} = \overline{n_o}\, e^{-t/\tau}$, where τ equals the 1/e loss time, τ can be calculated to be 3.32×10^{-6} seconds. This number was found to agree fairly well with loss times calculated by scaling from longer devices, specifically Scylla I-C, where the loss times have been experimentally determined by interferometric techniques. However, the method outlined here requires further substantiation, and further experimental work must be performed before data interpretation can be considered complete.

5. Completion of Research Studies

In order to fully explore the potential of Twyman-Green interferometer for use on pulsed theta pinch experiments some further steps are being taken. First, a second detector system is being fabricated. This will enable investigation of both temporal and spatial effects simultaneously. It will be utilized with variable position fiber optics pickup. Also, in order to provide a longer, quiescent period during which to examine loss, the capacitance of the bank will be expanded, and, by inclusion of inductors, the half-cycle time will be increased to approximately 15 μf. This will also allow investigation of loss at higher fill pressures (75-200 mT).

V. EVALUATION OF DIAGNOSTICS FOR STUDY OF THETA PINCH END LOSS

As indicated above, it is anticipated that several diagnostics which are inserted into the plasma will be used to study flow at the ends of the 25 cm pinch. These diagnostics include pressure sensors, electric field sensors, and velocity sensors, all of which have successfully been used in this laboratory to study transient flows from linear z-pinch plasma.[21,22] Initial studies of the performance of these diagnostics at the end of a linear theta pinch have been undertaken. However, because of the development of systems on the 25 cm pinch, and the conduct of detailed spectroscopic studies, the initial evaluation of probe performance was carried out in the 10 cm long theta pinch device. The general discharge characteristics, field strength, etc. have been addressed above, and that information will not be repeated here. Also, the details of the construction, performance, and general behavior of each of the diagnostics to be described have been reported elsewhere[22] and thus will not be repeated. Rather, some brief summary comments on the probes will be made, and then characteristics of the type of data gathered will be presented.

The general nature of the theta discharge was categorized above, where the plasma lifetime, density and temperature were estimated, and correlated primarily with local magnetic probe data. Specifically, with reference to Fig. 13, with 50 mT hydrogen fill pressure, it can be seen that during the second half-cycle an intense sheath collapse does occur at mid-coil ($z = 5.25$ cm). However, Fig. 13 shows that sheath collapse at axial positions approaching the end occur very quickly and probably with very little mass pickup and compression. Within the central 6 cm of the 10.5 cm pinch there appears to be dynamic sheath collapse and

compression; plasma in that region would be escaping through effectively vacuum fields at the ends (z = 0). It will be noted that the plasma created in this device is generally low energy (i.e. temperature), and so dynamic interactions will not be intense.

1. Pressure Sensor and Performance

The type of pressure probe that was utilized is shown in Fig. 17. The principal of operation is based on the piezoelective effect, with the application of mechanical stress to one side of the piezoelement producing a charge difference on the surface. The magnitude of the output is proportional to the applied stress. The specific instrument used was enclosed in an outer pyrex tube of 8 mm diameter with a quartz disk insulator epoxied on the sensing surface. The probe unit had a risetime of 0.1 μsec and was calibrated in a shock tube; the output was found to be $v_c/\Delta p = 0.38$ volts/atm. Units of this type had been used on Scylla I-C at Los Alamos,[12] but their risetime was 1 μsec because of cable lengths, (50 ft) involved.

Data was recorded with the pressure probe inserted axially through an end flange of the discharge tube. It was found that the probe structure was sensitive to forces induced by transient magnetic loading; these signals were suppressed by the fitting of a stainless steel tube outside, but not in contact with, the probe unit. Data is shown as Fig. 18 for several different axial positions. The probe was positioned on axis 2 cm inside coil (+2), at coil end (z = 0), and 2 cm outside (-2) coil with a gas fill pressure of 100 mT hydrogen. During the first four microseconds of discharge, the transient magnetic fields are producing preionization but no sheath collapse. During the second half cycle (4-8 μsec) a sheath is created and collapses to axis in about 1 μsec. At

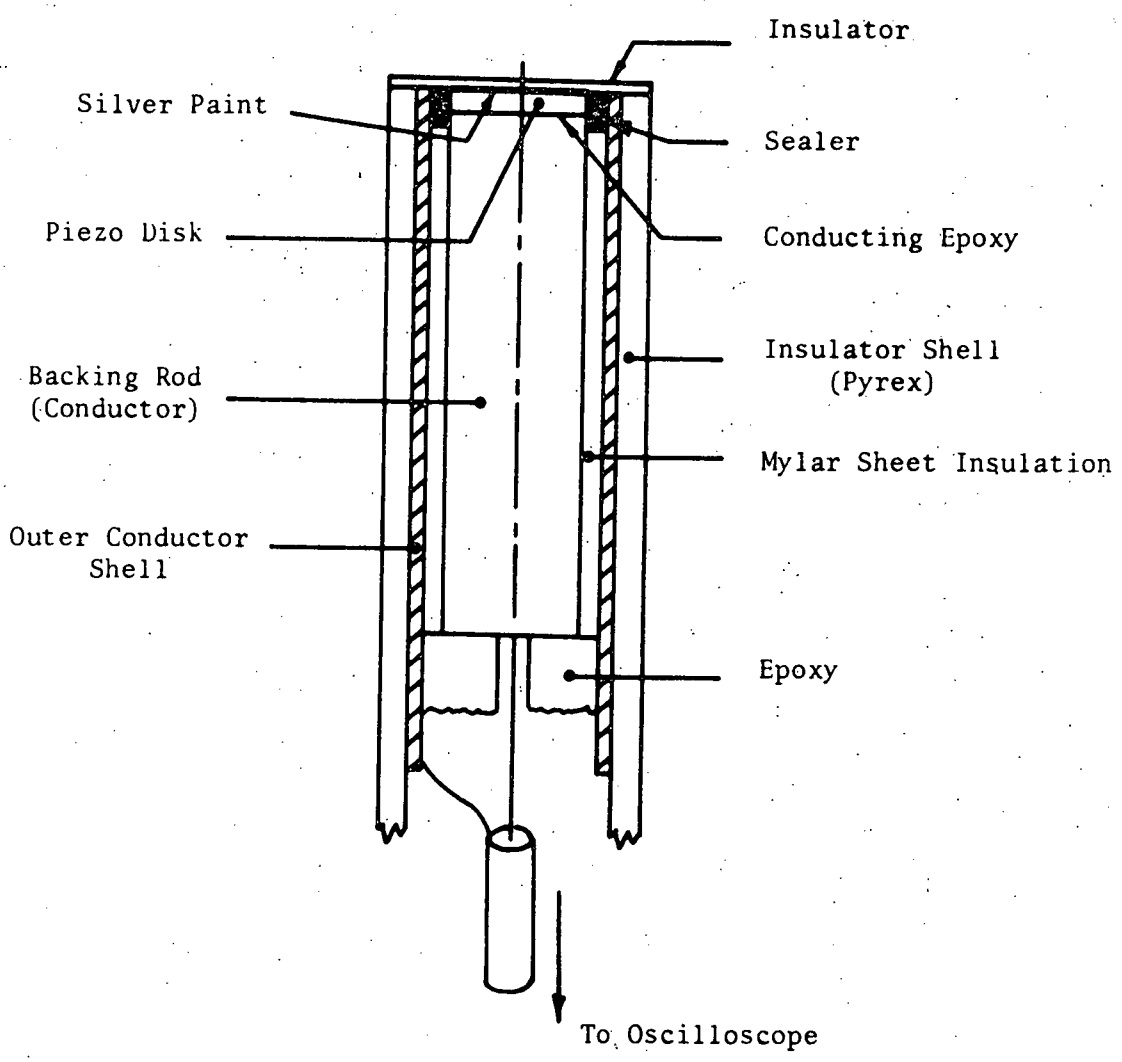

Figure 17. Piezoelectric Pressure Probe Schematic.

Sheath initiation

P_z
(0.1 V/div)
z = +2 cm
r = 0

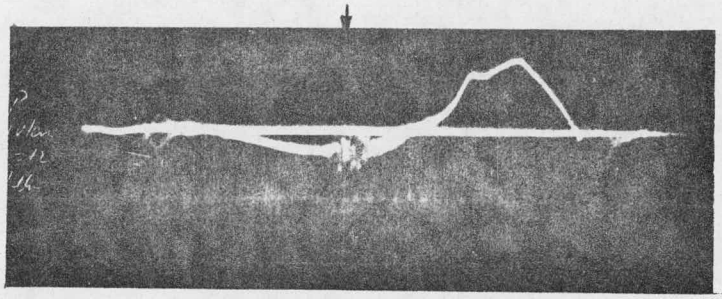

P_z
(0.1 V/div)
z = 0 cm
r = 0

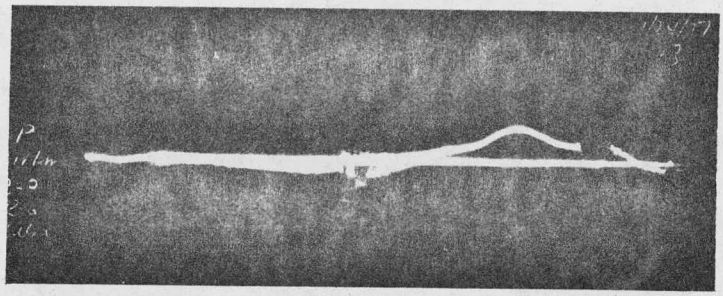

P_z
(0.1 V/div)
z = -2 cm
r = 0

B_z pinch
z = -2 cm
r = 1.75 in

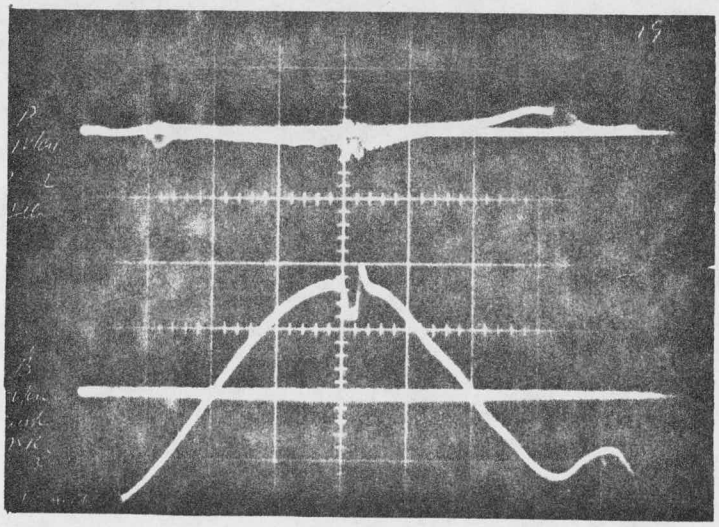

Figure 18. Response of Piezoelectric Pressure Probe to Flow at End of 10 cm Pinch
100 mT hydrogen fill pressure, 1 μsec/cm

all locations at this point in time there is the indication of signal initiation which then increases in magnitude before diminishing to reference at reversal time (8 μsec). Signals are stronger inside the coil and it does appear that there is propagation of a burst of plasma out of the system as evidenced by the delayed arrival of peak pressure signal at location farther from the center of the coil. It is concluded that this type of diagnostic can be developed satisfactorily to indicate flow transients occuring in 0.1 μsec time scale on the 25 cm long pinch.

2. Electric Field Sensor and Performance

The probe construction and circuitry is shown in Fig. 19. This type of diagnostic is well documented in the literature, 4 and has been used to study current sheath structure. It measures the difference between floating potential between two displaced electrodes. It was inserted axially into the pinch discharge tube in order to sense local E_z fields related to the transient plasma flow out of the discharge coil. Data was taken with 100 mT hydrogen fill and the probe positioned on axis at three different positions: 2 cm inside, coil end ($z = 0$), and 2 cm outside. Records are presented in Fig. 20, and again the distinction between preionization (< 4 μsec) and first dynamic collapse (4-8 μsec) should be noted. The indications of field before sheath formulation are not understood. Sheath collapse occurs in about 1 μsec, and the electric field behavior after this point in time (5 μsec) is of interest. While this data is preliminary, it will be noted that there apparently is a definable field structure when the plasma is flowing by the sensor, and its sequential development in time and space is similar to that indicated by the pressure sensor. The nature of the signals from this diagnostic

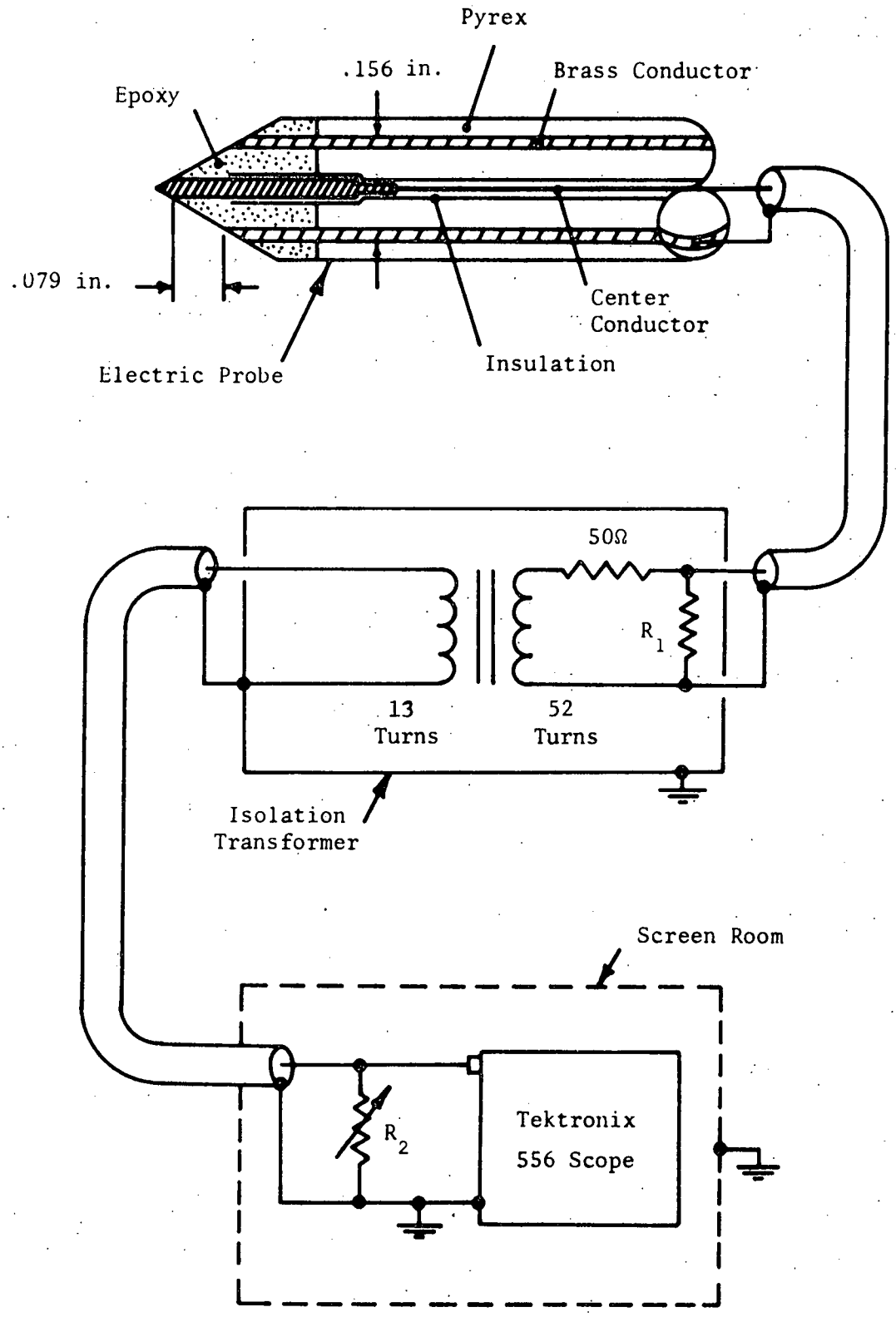

Figure 19. Electric Probe System Schematic.

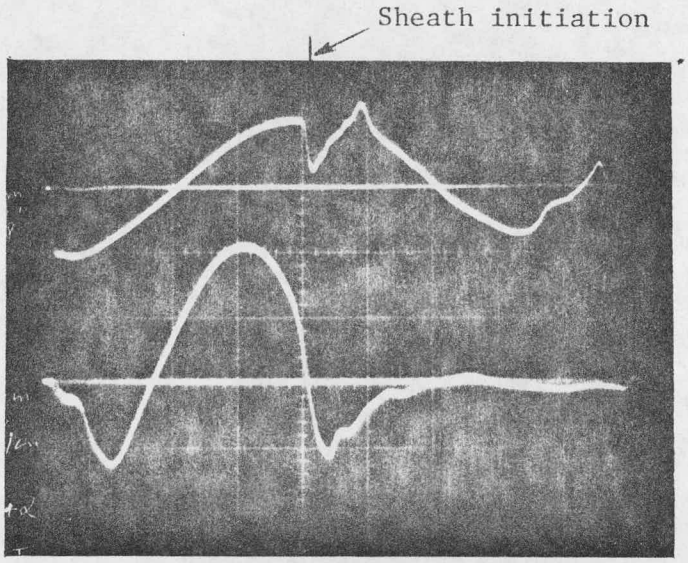

$\dot{B}_z$ pinch

z = +2 cm
r = 7/8 cm

E_z

(5 V/div)
z = +2 cm
r = 0

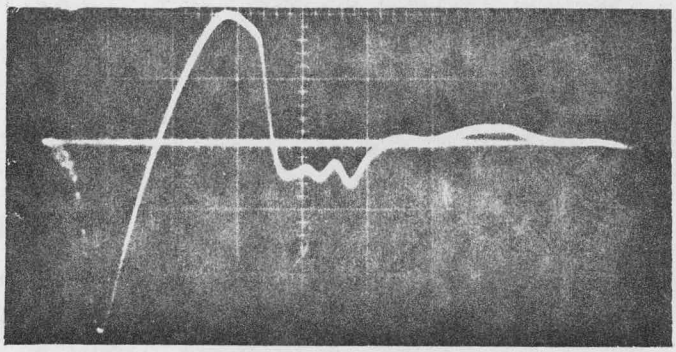

E_z

(5 V/div)
z = 0 cm
r = 0

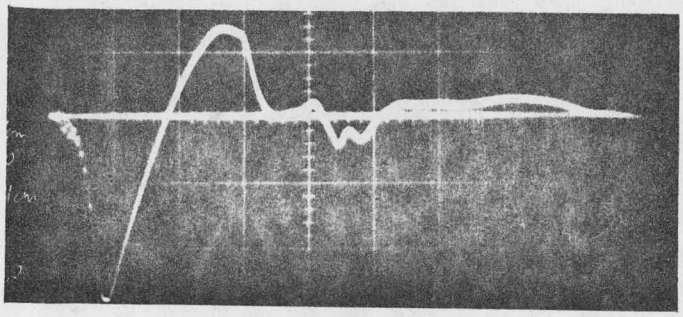

E_z

(5 V/div)
z = -2 cm
r = 0

Figure 20. Responses to E_z Probe to Flow at End of 10 cm Pinch
100 mT hydrogen fill pressure, 1 μsec/cm

provides a basis for further development and studies of the plasma flow in the 25 cm long device.

3. Velocity Indications From Displaced and Biased Pairs of Electrodes

A schematic of this type of diagnostic is shown in Fig. 21. It is intended to function by each pair of electrodes responding to the presence of plasma between them and allowing passage of current by being part of a capacitor driven circuit. Circuit current is monitored, and presuming that local perturbations in plasma density and temperature will be propagated with the plasma, the delay in similar signals should be indicative of plasma velocity.

This sensing device was placed in the theta pinch discharge tube with the leading pair at positions of +2 cm, 0 cm, and -2 cm. Definite signals of the expected nature were monitored during the third half cycle, but there was no ability to distinguish velocity during the second half cycle. Signal strength was found to diminish with increasing fill pressure between 50 and 200 mT hydrogen; it also decreased with distance from the coil center. It does appear that consideration must be given to altering the design of the probe, particularly with regard to: electrode spacing and size, bias voltage, and pair separation. This probe redesign will be carried out, and the diagnostic reevaluated for its' applicability in these plasma flows.

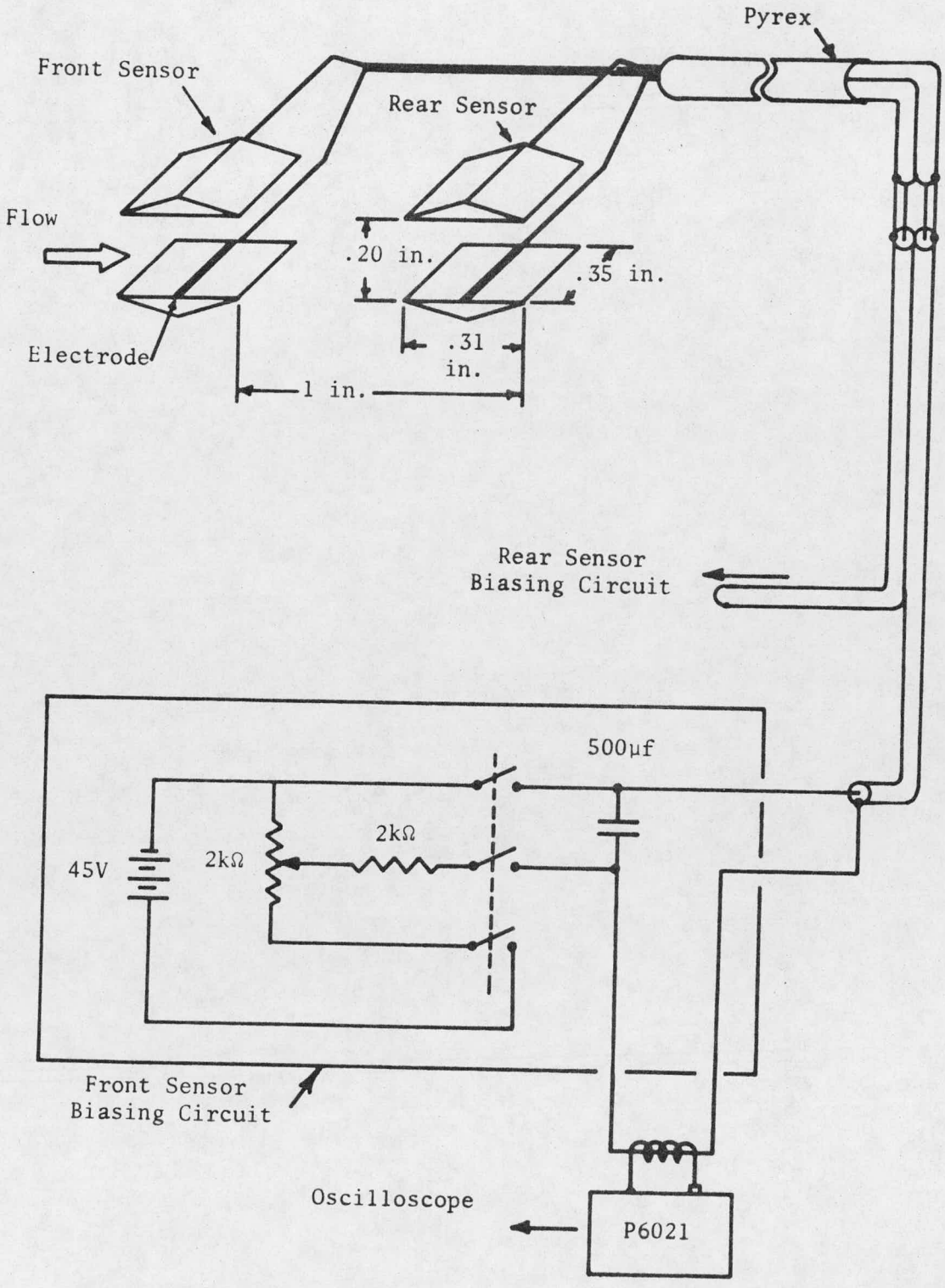

Figure 21. Velocity Probe System Schematic.

VI. ALTERATION OF FACILITY TO 50 CM LONG THETA PINCH (Robinson)

During the present reporting period, detailed attention has been given to the signifcant alteration of the present 25 cm long pinch discharge system. The changes in this system are intended to double the theta coil length, while maintaining the magnetic field strength. This will be accomplished by doubling the capacitance of the energy storage bank. Also, it is desirable to study the transient plasma loss events in a magnetic field configuration which is reasonably steady after dynamic collapse and adiabatic compression phases; this will be accomplished by crowbaring the electrical discharge. Lastly, this alteration of the energy discharge system must be compatible with the utilization of the Thomson scattering laser diagnostic, the timing of which requires accuracy within nanoseconds while events occur over milliseconds. The design phase of the alteration procedures is completed and the mechanical design and fabrication are being initiated.

1. Energy Storage Capacitors

Following an evaluation of performance and cost of capacitors that are currently available from manufacturers such as Maxwell, Tobe Deutschman, Sangamo and Aerovox, units that are manufactured by Maxwell Laboratories were selected and procured. Specifically, 11 capacitors rated at 14 μF, 20 kV and of a type designed for high voltage reversal (Model 33006) have been delivered for use. Two of these units will replace preionization capactors, eight will be in active use, allowing one capacitor available with project funding as a spare. Pairs of capacitors will be built into parallel plate feed line and connected to one of four switches, which will be connected by sets of (8) cables to the main theta pinch collecter plates.

2. Capacitor Bank Discharge Switches

Because of difficulties encountered in the simultaneous switching of rows of charged capcitors noted above, consideration has been given to the redesign of the switch units. Clearly, any such problem encountered will be magnified with a total of eight switches. The present design involves discharge of a switch capacitor into lines leading to pins centered on the axis of the ground electrodes of the opposed hemispherical electrode switches for each row. The inductance of the cables and switch capacitor result in a slowly rising pulse to drive the switches. An alternative scheme which utilizes the capacitance of 50 ft of RG 8/U coaxial cable to store switch energy produces a much sharper pulse for switch purposes. This scheme has been tested and will be used for developing the switch pulse because of its satisfactory performance. Also, to provide further precision in igniting the switch for each row, the center pin switch electrode will be replaced by units which are inserted midway between switch interelectrode gaps.

3. Preionization Discharge Switch

At the present time a low inductance gas switch has been used to initiate the preionization discharge. The "jitter" in the onset of preionization is on the order of 100's of microseconds. As the Thomson scattering experiment must have built in delays on the order of milli-seconds, a much more precisely timed PI switch must be installed. The switch unit will be built into the top of the PI capacitor and will be similar to those presently in use, as the anticipated delay of several microseconds is acceptable. The gap will be driven by a series of pulse generators which will convert a 5 V output from a signal delay generator into a 30 kV trigger pulse.

4. Crowbaring of the Theta Discharge Circuit

With the doubling of the energy storage capability of the capacitor bank, the total current flowing in the pinch coil will be a maximum of 1.4 MA. With a coil inductance of 20 nH, a satisfactory crowbar system, i.e. one which would have $\pm$ 10 percent residual ringing would require a crowbar inductance of about 5 nH. In order to achieve such performance a design has been developed using a series of spark gaps to be positioned along the feeder parallel plate system for the coil. With an estimate of 40 mH inductance for each gap, a series of 10 gaps (5 on each side) is expected to provide the necessary level of inductance to generate a satisfactory crowbared circuit behavior. Mechanical design and fabrication along with the associated switch generating circuitry are proceeding on this component. It has been decided to forego the use of ignitrons and thyratrons in this system as specified in the original proposal.

VII. END LOSS THEORY AND COMPUTER MODELING OF PLASMA COLUMN BEHAVIOR (E. Stover)

1. Introduction

Several theoretical studies have been conducted since the mid-1960's to describe plasma end loss from a linear theta pinch plasma column.[23-30] The primary goal of these studies was to analytically or numerically describe the axial flow of plasma particles and/or thermal conduction of energy through the ends of the plasma column. In the case of previous analytical studies conducted, emphasis, as a result of mathematical necessity, was placed on finding quasisteady or steady solutions for end loss without the inclusion of heat conduction effects.[23-26,30] Thus, the important inherent unsteady nature of the end loss phenomena resulting from plasma column properties evolving due to end loss and thermal conduction has not been considered. These effects, however, have been incorporated in the comprehensive, but complex and costly two dimensional numerical codes developed thus far.[28,29] Due to the cost and complexity of these codes, only a few theta pinch configurations have been investiated. The purpose of this investigation was to develop a relatively simple time dependent, zero-dimensional model in n, N, T_e and T_i to investigate the influence of thermal conduction, work done on the plasma by the applied magnetic field, and magnetic field diffusion on end loss.

End loss is modeled through the use of a confinement time τ_p which contains an unknown scaling parameter χ.

This can be expressed as

$$\tau_p = \frac{L}{2} \left(\frac{m_i}{2kT_i}\right)^{\frac{1}{2}} 2\sqrt{\pi} \quad \chi \ .$$

The parameter χ is chosen to match end-on interferometry measurement of N and is used as a basis for evaluating the models which will be considered below and evaluating the various plasma column phenomenon by matching experimental data with computed values of n, N, T_e and T_i.

2. Model Development

Our present computational capability has evolved through the continual development of a set of zero dimensional conservation equation. Three computer models of significance were developed from these equations and used to evaluate experimental results; they are the constant plasma area model, the constant embedded magnetic flux model, and the magnetic field diffusion model. All models include particle end loss, electron heat conductivity along the magnetic field lines, ion heat conductivity along the magnetic field lines if the ion-ion mean free path is less than the compression coil length, and electron-ion thermal equilibration. The zero dimensional conservation equations include conservation of total particles, and separate conservation equations for electron and ion energy. Modeling of end loss through the characteristic end loss time τ_p guarantees satisfaction of ion axial momentum. The electron axial momentum equation need not be considered here, for the electron axial motion is assumed to be tightly coupled to the ion axial motion due to their mutual electrostatic attraction and small electron mass. In addition, plasmas consisting only of isotopes of hydrogen are

considered; thus both electron and ion number densities and volumetric flow rates through the column ends are considered to be equal.

The conservation equations for plasma column electron energy, W_e, ion energy, W_i, and particles N can be written

$$\frac{dW_e}{dt} = W_{ie} - \dot{H}^e_{cond} - \varepsilon_e \Gamma - P_e\left(\frac{dV}{dt}\right) \qquad (1)$$

$$\frac{dW_i}{dt} = -W_{ie} - \dot{H}^i_{cond} - \varepsilon_i \Gamma - P_i\left(\frac{dV}{dt}\right) \qquad (2)$$

and

$$\frac{dN}{dt} = -\Gamma = -N/\tau_p \ , \qquad (3)$$

where

N = Total number of ions or electrons in the plasma column

$$= \int_{-L/2}^{L/2} \int^{Ap} n(r,z)\ dAdz = L \int_o^{Ap} n(r)\ dA$$

W_s = Thermal energy of species s

$$= \int_{-L/2}^{L/2} \int^{Ap} \frac{3}{2} n(r,z)\ k\ T_s(z)\ dAdz = \frac{3L}{2} \int^{Ap} n(r)\ kT_s\ dA$$

W_{ie} = Rate of energy transfer from the ions to the electrons

$$= (W_i - W_e) \ / \ \tau_{eq}$$

$P_s \frac{dV}{dt}$ = Work done by species s in the expanding plasma column

$$= n_s k\ T_s L\ \frac{dAp}{dt}$$

$\varepsilon_s \Gamma$ = Total flow of species s plasma thermal energy across the column ends

$$= L \int^{Ap} \frac{\varepsilon_s n(r)}{\tau_p}\ dA$$

$\dot{H}^s_{cond}$ = Rate of heat transfer by species s from conduction across the column ends.

$$= \int_{-L/2}^{L/2} \int^{Ap} \frac{\partial Q^s_{Th}}{\partial z}\ dzdA$$

The z coordinate is defined along the compression coil longitudinal axis with the midplane value equal to zero, and the r coordinate is the usual radial coordinate in cylindrical geometry. We have assumed that both ion and electron temperatures are independent of r and that Ap is the z averaged plasma column area. Furthermore, it was assumed that either the z dependence in T is weak enough or that significant axial gradients in T occur over a sheath thickness sufficiently small with respect to column length to justify $\overline{nkT} = \bar{n}\bar{k}\bar{T}$ where the barred quantities denote column averages over both r and z. Thus equations (1), (2) and (3) become

$$\frac{1}{T_e}\frac{dT_e}{dt} = \frac{1}{\bar{n}T_e}(T_i - T_e)\,\overline{(n/\tau_{eq})} - \frac{1}{\bar{n}}\,\overline{(n/\tau^e_{th})} - \frac{1}{\tau_p}\left(\frac{2\varepsilon_e}{3RT_e} - 1\right) - \frac{2}{3}\frac{1}{Ap}\frac{dAp}{dt}, \quad (4)$$

$$\frac{1}{T_i}\frac{dT_i}{dt} = \frac{1}{\bar{n}T_i}(T_e - T_i)\,\overline{(n/\tau_{eq})} - \frac{1}{\bar{n}}\,\overline{(n/\tau^i_{Th})} - \frac{1}{\tau_p}\left(\frac{2\varepsilon_i}{3RT_i} - 1\right) - \frac{2}{3}\frac{1}{Ap}\frac{dAp}{dt}, \quad (5)$$

$$\frac{1}{\bar{n}}\frac{d\bar{n}}{dt} = -\frac{1}{\tau_p} - \frac{1}{Ap}\frac{dAp}{dt}, \quad (6)$$

where the rate of heat transfer from conduction through the column ends was expressed in terms of a thermal conduction time τ^s_{Th} by

$$\dot{H}^s = 2\int^{Ap} Q^s_{Th}\left(\frac{L}{2}\right) dA \equiv \int^{Ap} \frac{\frac{3}{2}\,nkT_s L\,dA}{\tau^s_{Th}} = \frac{3}{2}\,kT_s L\,\overline{(n/\tau^s_{Th})}\,Ap.$$

The expression for τ^e_{Th} used throughout this study was obtained from an electron thermal heat conductivity analysis by Morse.[27] The result of Morse used here followed by assuming that: (a) heat flux out the ends is approximately constant along the magnetic field

lines; (b) the temperature declines from an average value T near the end of the plasma to zero in a distance ℓ_1 from the coil end; and (c) thermal conductivity is the classical electron thermal conductivity. His result is

$$\tau_{Th}^{e} = 8.65 \times 10^{-31} \frac{n\ell_1 L \ln \Lambda}{T_e^{5/2}} \qquad (6a)$$

where $\ln\Lambda$ is the Debye logarithm and all units are MKS with the exception of T which is in keV. The sheath thickness is not specified in the theory. The value $\ell_1 = .2L$ was chosen by Morse. The validity of this choice, as well as the assumptions stated above, are uncertain. Thus, further study will be made to examine the validity of the Morse result.

Ion thermal conduction was also considered in terms of a characteristic thermal conduction time. Taking the classical ion conductivity expression in Braginski[31], the ion thermal conduction time can be related to the electron thermal conduction time from

$$\tau_{Th}^{i} = \tau_{Th}^{e} \left(\frac{T_e}{T_i}\right)^{\frac{5}{2}} \left(\frac{m_i}{m_e}\right) \Big/ 1.745 \; . \qquad (6b)$$

The ion-ion mean free path was found to be greater than the plasma column length for some of the high temperature experiments investigated. In these cases, the ion cannot lose energy by classical ion conduction, so when $\lambda_{ii}/L > 1$, ion thermal conduction was neglected. The electron-electron mean free path is much smaller than the column length in all experiments considered, so classical electron thermal conductivity is always included as an energy loss mechanism.

The thermal energy ε_s convected across the column ends is also dependent on λ_{ii}/L. If $\lambda_{ii}/L<1$ it is assumed that species will lose by convection energy with a mean energy of $\frac{3}{2}kT_s$ per particle. Thus, ε_e is always $\frac{3}{2}kT_e$ for cases considered here. For ion collionless experiments, where $\lambda_{ii}/L>1$, a simple kinetic calculation indicates that fast particles preferentially flow through the column ends with a mean ion thermal energy of $2kT_i$. Thus, in summary,

$$\varepsilon_i = \begin{cases} \frac{3}{2}kT_i\ , & \lambda_{ii}/L < 1 \\ 2\,kT_i\ , & \lambda_{ii}/L > 1 \end{cases}$$

and $$\varepsilon_e = \frac{3}{2}kT_e \ .$$

On the basis of these considerations the electron and ion energy conservation equations become

$$\frac{1}{T_e}\frac{dT_e}{dt} = \frac{1}{nT_e}(T_i-T_e)\,\overline{(n/\tau_{eq})} - \frac{1}{n}\,\overline{(n/\tau^e_{Th})} - \frac{2}{3}\,\frac{1}{Ap}\,\frac{dAp}{dt}\ , \tag{7}$$

and

$$\frac{1}{T_i}\frac{dT_i}{dt} = \frac{1}{nT_i}(T_e-T_i)\,\overline{(n/\tau_{eq})} - \frac{1}{n}\,\overline{(n/\tau^i_{Th})}\,u(L-\lambda_{ii}) - \frac{1}{3\tau_p}\,u(\lambda_{ii}-L) - \frac{2}{3}\,\frac{1}{Ap}\,\frac{dAp}{dt} \tag{8}$$

where $u(\lambda_{ii}-L)$ and $u(L-\lambda_{ii})$ are heavyside step functions.

In the first numerical model developed-- Model 1--the plasma was taken to be radially uniform with a sharp boundary. In addition, based on interferometer measurements, the plasma column area was taken as constant. Plasma end loss was investigated for crowbared experiments

only, and for time points following crowbaring of the capacitor bank. With these assumptions, the conservation equations (6), (7) and (8) can be written as

$$\frac{dT_e}{dt} = (T_i - T_e)/\tau_{eq} - T_e/\tau_{Th}^e \quad ,$$

$$\frac{dT_i}{dt} = (T_e - T_i)/\tau_{eq} - (T_i/\tau_{Th}^i)\, u(L-\lambda_{ii}) - \left(\frac{1}{3\tau_p}\right) u\,(\lambda_{ii}-L) \quad ,$$

$$\frac{dn}{dt} = -n/\tau_p \quad .$$

This first order system of linear differential equations was numerically solved on the University IBM 360 computer using Hamming's modified predictor-corrector fourth order integration procedure. This integration method requires approximately one half the computation time as the Runge-Kutta method and gives about the same accuracy.

It should be noted that the radial pressure balance equation was not used any where in constraining the solution. Instead it was assumed that the magnetic flux embedded in the plasma column, ϕ_p, would vary to satisfy radial pressure balance

$$\phi_p^2 = B_e^2 A_p^2 - 2\mu_o nk(T_e + T_i)\, A_p^2 \quad .$$

In the next two models to be discussed here, the magnetic flux embedded in the plasma column will be restricted enabling the rate of plasma column area to be explicitly determined. A comparison between numerical and experimental results will be made in the next section.

Restricting the plasma column area to a constant prevents consideration of the work done on the plasma column by the applied magnetic field. Thus, development of the plasma column can not be studied either from post implosion to crowbar in crowbared systems, or at any time for non crowbared systems. In the next model considered , the work done on the plasma is obtained by constraining the magnetic flux embedded in the plasma to be a constant. This work is a generalization of Green et. al.[32] to include end loss. Plasma resistivity is thus assumed to be sufficiently small that diffusion of magnetic field into the plasma can be neglected. This model is discussed below.

In Model II, the plasma was considered to be radially uniform with a sharp boundary as assumed in Model I. To obtain (1/Ap) dAp/dt appearing in equations (6), (7) and (8), radial pressure balance is used:

$$nkT_e + nkT_i + \frac{\phi^2}{2\mu_o Ap^2} = \frac{B_e^2}{2\mu_o} \tag{9}$$

where ϕ is the magnetic flux embedded in the plasma. Differentiating (9) with respect to time and setting

$$\frac{d\phi}{dt} = 0,$$

the plasma area is found to be constrained by

$$nk(T_e + T_i)\frac{dn}{dt} + nk\left(\frac{dT_e}{dt} + \frac{dT_i}{dt}\right) - \frac{\phi^2}{\mu_o Ap^2}\frac{1}{Ap}\frac{dAp}{dt} = \frac{B_e}{\mu o}\frac{dB_e}{dt} \quad . \tag{10}$$

From equation (9) the flux, ϕ, is related to column parameters by

$$\phi^2 = B_e^2 A_p^2 (1-\beta) \tag{11}$$

where β has the conventional definition

$$\beta \equiv \frac{nk(T_e + T_i)}{B_e^2/2\mu_o} \quad . \tag{11a}$$

Thus, with the applied magnetic field wave form known, equations (6), (7), (8), (10) and (11) form a complete set of equations which can be solved explicitly for (1/Ap) dAp/dt ,

$$\frac{1}{Ap}\frac{dAp}{dt} = -\left(\frac{6}{6-\beta}\right)\frac{1}{B_e}\frac{dB_e}{dt} - \left(\frac{3\beta}{6-\beta}\right)\left[\frac{1}{\tau_p} + \left(\frac{T_e}{T_e+T_i}\right)\frac{1}{\tau_{Th}^e} + \frac{T_i}{T_e+T_i}\frac{1}{\tau_{Th}^i}\right.$$

$$\left. + \left(\frac{T_i}{T_e+T_i}\right)\frac{1}{\tau_p}\left(\frac{2}{3}\frac{\varepsilon_i}{kT_i} - 1\right)\right] . \tag{12}$$

Note that plasma column area will decrease as the result of particle and energy end loss as well as with increasing applied magnetic field. Plasma column parameters T_e, T_i, n and N were then solved for by numerical integration of the set of equations (3), (6), (7), (8) and (12).

A numerical simulation of Scylla IC using Model II yielded results which differed significantly from the experimental results presented by McKenna and York.[33] Numerical results indicated that plasma column magnetic field flux was not conserved but increased with time. This prompted consideration of a relaxation of the flux conservation logic by assuming that a flux increasing mechanism is

present which is sufficient to balance out the loss terms bracketed in equation (12). This assumption yielded good agreement between numerical and experimental results, indicating that magnetic field flux diffusion into the plasma column was significant for that experiment. This prompted a systematic extension of Model II to allow diffusion of applied magnetic field into the plasma column resulting from finite plasma resistivity. This final variation on the zero dimensional conservation equations will be referred to as Model III. Numerical simulation results from Model II are presented with Model I results in the next section.

In Model III the plasma number density and plasma magnetic field were allowed to vary with radius. The plasma magnetic field was assumed to vary parabolically with radius per Steinhauer,[30]

$$B(r) = B_a + (B_e - B_a)\,(r/a)^2 \tag{13}$$

where B_a is the on-axis magnetic field and a is the plasma column radius. Assuming T_e and T_i are independent of radius, the number density distribution is then found from radial pressure balance

$$\frac{B_e^2}{2\mu_o} = \frac{B^2(r)}{2\mu_o} + n(r)\,k(T_e + T_i),$$

to be

$$n(r) = \frac{B_{e/}^2}{k(T_e+T_i)}\left[(1-\zeta_a^2) - 2\zeta_a(1-\zeta_a)(r/a)^2 - (1-\zeta_a)^2(r/a)^4\right]$$

where

$$\zeta = B_a/B_e \ .$$

Note that as $\zeta_a \longrightarrow 0$ the n(r) profile approaches $[1-(r/a)^4]$ variation. As $\zeta_a \longrightarrow 1$, the parabolic term, $2(1-\zeta_a)[1-(r/a)^2]$

tends to dominate. Shape factors were determined for the energy equilibration and thermal conduction terms in equations (7) and (8), for τ_{Th}^{s} and τ_{eq} are functions of n. These will be discussed below.

Evolution of both the magnetic field embedded in the plasma column and the number density profile is dependent on the time variation of ζ_a. An expression for $d\zeta_a/dt$ was derived in terms of plasma resistivity η, ζ_a, $(1/Ap)(dAp/dt)$ and $(1/B_e)(dB_e/dt)$ by solving a magnetic flux diffusion equation for a long narrow plasma column.

Recalling Maxwell's equations,

$$\bar{\nabla} \times \bar{B} = \mu_o \bar{J} \quad , \qquad \bar{\nabla} \times \bar{E} = - \frac{\partial \bar{B}}{\partial t}$$

and Ohm's Law

$$\bar{J} = \frac{1}{\eta} (\bar{E} + \bar{u} \times \bar{B}) \ ,$$

and assuming that the plasma column is sufficiently long so that: (a) radial magnetic field components are small, $B_r/B_z \ll 1$ and, (b) B_z is dependent only on r , the rate of change of magnetic field flux in a column of radius a is given by

$$\frac{\partial \phi}{\partial t} = \int^{Ap} \frac{1}{r} \frac{\partial}{\partial r} \left(\frac{r}{\mu_o \sigma} \frac{\partial B_z}{\partial r} \right) dA = \frac{2\pi a}{\mu_o} \eta \frac{\partial B_z}{\partial r} \Bigg|_{r=a}$$

Recognizing

$$\phi = \int_o^a B_z \, 2\pi r dr$$

and remembering $B_z(r)$ from equation (13), the desired expression for $d\zeta_{a/dt}$ is obtained:

$$\frac{d\zeta_a}{dt} = \frac{8\pi\eta}{\mu_o}\frac{1}{Ap}(1-\zeta_a) - (1+\zeta_a)\left(\frac{1}{Ap}\frac{dAp}{dt} + \frac{1}{B_e}\frac{dB_e}{dt}\right) \quad . \qquad (15)$$

The plasma diamagnetic current must flow transverse to the magnetic field lines. Thus, the appropriate plasma resistivity must be chosen. For theta pinch experiments considered here, the magnetic field is of sufficient magnitude that the electron Larmor frequency is many orders of magnitude greater than the electron collision frequency. Consequently, the strong magnetic field limit expression for plasma resistivity[34] was used in this analysis,

$$\eta_\perp = 3.27 \times 10^{-9}\ \ell n\Lambda\ /T_e^{\frac{3}{2}} \qquad \text{(ohm-meters)} \ .$$

Again it was required that dAp/dt be explicitly determined. This was done by solving equation (6) where $\bar{n}$ is related to B_e, ζ_a, T_e+T_i , through

$$\bar{n} = \left(\int_o^a n(r)\ 2\pi r dr\right)/\pi a^2$$

with n(r) given by equation (14). Algebraic manipulation of the resultant equation (6) with equations (7), (8) and (15) yields the solution for (1/Ap) dAp/dt

$$\left(\frac{1}{Ap}\right)\left(\frac{dAp}{dt}\right) = -\frac{6}{(13+4\zeta_a+\zeta_a^2)}\left\{\frac{1}{2}(\zeta_a+5)\frac{1}{B_e}\frac{dB_e}{dt} - (\zeta_a+\tfrac{1}{2})(1-\zeta_a)8\pi\frac{\eta_\perp}{\mu_o}\frac{1}{Ap} + \right. \qquad (16)$$

$$\left.(1-\zeta_a)(1+\zeta_a/2)\left[\frac{1}{\tau_p} + \frac{1}{(T_e+T_i)}S(\zeta_a)\left(\frac{T_e}{\tau_{Th}^{e}} + \frac{T_i}{\tau_{Th}^{i}}u(L-\lambda_{ii})\right) + \frac{T_i}{T_e+T_i}\frac{1}{3\tau_p}\right]\right\}.$$

The factor $S(\zeta_a)$ is the shape factor noted above which arises from the non uniform radial distribution of particles in the plasma

column. It was determined by evaluating the column averages $\frac{1}{\bar{n}}\overline{(n/\tau_{eq})}$ and $\frac{1}{\bar{n}}\overline{(n/\tau^{s}_{Th})}$ in equations (7) and (8) with τ^{s}_{Th} given by equations (6a) and (6b) and

$$\tau_{eq} = 9.96 \times 10^{18} \quad T_e^{\frac{3}{2}}/(n\ell n\Lambda).$$

Performing the averages,

$$\frac{1}{\bar{n}}\overline{(n/\tau_{eq})} = S(\zeta_a)/(\tau_{eq})n_A, \qquad (17)$$

$$\frac{1}{\bar{n}}\overline{(n/\tau^{s}_{Th})} = S(\zeta_a)/(\tau^{s}_{Th})n_A, \qquad (18)$$

with

$$S(\zeta_a)=[8-7\zeta_a(1+\zeta_a)+3\zeta_a^2(1+\zeta_a^2)]/[10(1-\zeta_a)^2(1+\zeta_a/2)(1+\zeta_a)]$$

where subscripts n_A denote evaluation of n(r) on the plasma column axis. The complete set of differential equations describing Model III plasma column behavior are thus

$$\frac{dN}{dt} = -N/\tau_p$$

$$\frac{1}{T_e}\frac{dT_e}{dt} = S(\zeta_a)\left[(\frac{T_i}{T_e}-1)/\tau_{eq} - \frac{1}{\tau_{Th}e}\right] - \frac{2}{3}\frac{1}{Ap}\frac{dAp}{dt}$$

$$\frac{1}{T_i}\frac{dT_i}{dt} = S(\zeta_a)\left[(\frac{T_e}{T_i}-1)/\tau_{eq} - \left(\frac{1}{\tau_{Th}i}\right)u(L-\lambda_{ii})\right] - \left(\frac{1}{3\tau_p}\right)u(\lambda_{ii}-L) - \frac{2}{3}\frac{1}{Ap}\frac{dAp}{dt}$$

$$\frac{d\zeta_a}{dt} = \frac{8\pi\eta}{\mu_o}\frac{1}{Ap}(1-\zeta_a)-(1+\zeta_a)(\frac{1}{Ap}\frac{dAp}{dt} + \frac{1}{B_e}\frac{dB_e}{dt}$$

and $\frac{1}{Ap}\frac{dAp}{dt}$ is given by equation (16).

The numerical solution proceeded by first calculating (1/Ap) (dAp/dt) which can then be used to evaluate dT_e/dt, dT_i/dt and $d\zeta_a/dt$. All of the above differential equations were then numerically integrated to obtain N, T_e, T_i, ζ_a and Ap. It should be noted that only four of the above differential equations need be solved to uniquely define the plasma properties. From ζ_a the average column number density may be found and combined with the plasma column area and given plasma length to determine the total number of particles inside the column, N. Equation (3) was integrated and used as a check for self consistency of the solution. Differences between N obtained from equation (3) and N calculated from

$$N = Ap\ \overline{nL}$$

were, in all cases checked, less than one per cent.

3. Analysis of Numerical Results by Comparison with Experimental Results

The numerical results from the three computer models are discussed below. These findings are compared with both collisional and collisionless experimental results in an effort to identify important physics issues such as the significance of both ion and electron heat conductivity on particle loss; the importance of magnetic field diffusion and the use of a single end loss scaling parameter. Except for Scylla I-C, most experimental data presented did not include sufficient information to enable a complete comparison with computed parameters, T_e, T_i, n and N determined from the numerical codes. However, sufficient data were presented in

most experiments such that some parameters could be compared.

The first model analyzed, Model I, is the most crude of the three models considered. However, it was found to be valuable in making quick evaluations for specific experiments. Again, in this model, because the plasma column properties are assumed to be uniform across a fixed column radius, applicability of the results is limited to theta pinch configurations in which the capacitor energy storage system is crowbared, and to times following crowbar. Four such theta pinch configurations are investigated below: (1) linear Scyllac;[35] (2) Scylla IV-P;[36] (3) Scylla IV-3;[37] (4) Scylla I-C.[33] Plasma initial conditions (crowbar) were obtained from the literature.

Theta pinch configurations which are clearly collisionless--Scylla IV-P and linear Scyllac--will be discussed first. Due to the fact that $\lambda_{ii}/L>1$ for both of these configurations, it would be anticipated that classical ion thermal conductivity would be meaningless and that ion temperature would change only as a result of ion-electron thermal equilibration. The electron temperature change would be dependent on the balance between energy gained by electron-ion thermal equilibration and energy loss by electron conduction. Comparison of numerical results with Scylla IV-P experimental results for time histories of ion temperature and total number of particles in the plasma column do indeed substantiate these statements. The comparisons presented in Figure 22 indicate that if the plasma ions were losing energy by classical ion conduction, the ion temperature

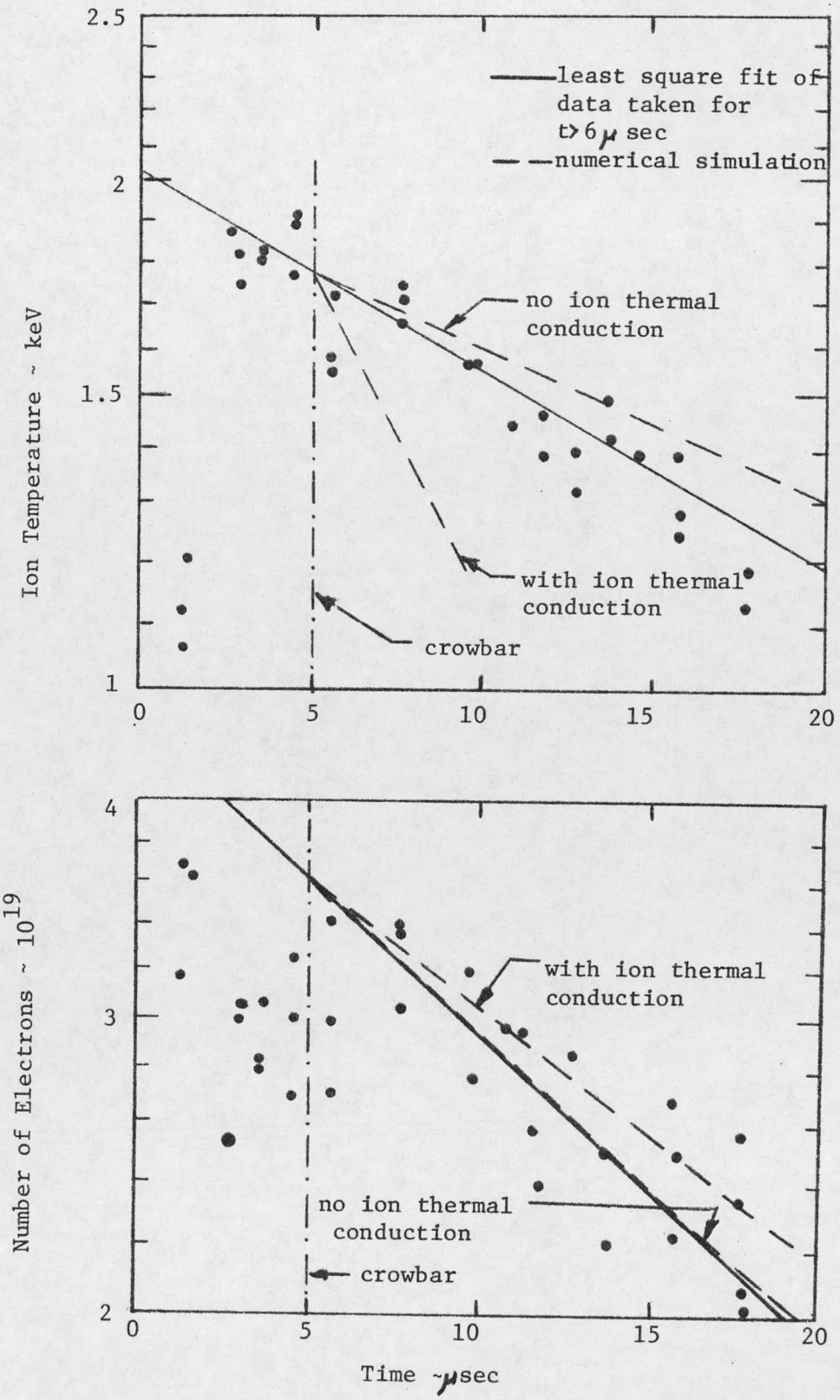

Figure 22. Comparison of Numerical Simulation Solution with Experimental Results - Scylla IV-P

decay time constant would be a factor of five greater than the value indicated by the experiment. Thus classical ion thermal conduction is not an energy loss mechanism for Scylla IV-P. The particle end loss parameter χ was chosen to be 1.08 to give reasonable agreement with the least squares curve fit of N vs. t data for t >6μsec in Figure 22. The effect of ion thermal heat conduction on end loss is also shown in Figure 22. Due to the lower ion temperature, predicted particle confinement time is too low. Comparison of χ with existing end loss theories will be discussed below. The power terms T_e/τ^e_{Th} and $(T_i-T_e)/\tau_{eq}$ are plotted in Figure 23 and indicate that the electron temperature decays monotonically with time from an initial value of 400eV. The electron thermal conduction time was found to vary from 5 μsec to 9μsec while the electron-ion equilibrium time remained at approximately 40μsec. Time histories of Scylla IV-P electron temperature were not available, preventing a check on the Morse model[27] adopted for electron thermal conduction effects. The good agreement between numerical and experimental ion temperatures does suggest that the model is reasonable.

The linear Syllac theta pinch experiment[35] was collisionless ($\lambda_{ii}/L \simeq 1$ at crowbar) so again ion thermal conduction effects should be negligible. Plasma column development was found to be similar to Scylla IV-P, for the ordering of τ^e_{Th}, τ_{eq} and τ_{EL} is the same. Again, electron thermal conductivity was found to be important, for τ^e_{Th} was found to vary from 3μsec to 6μsec over the

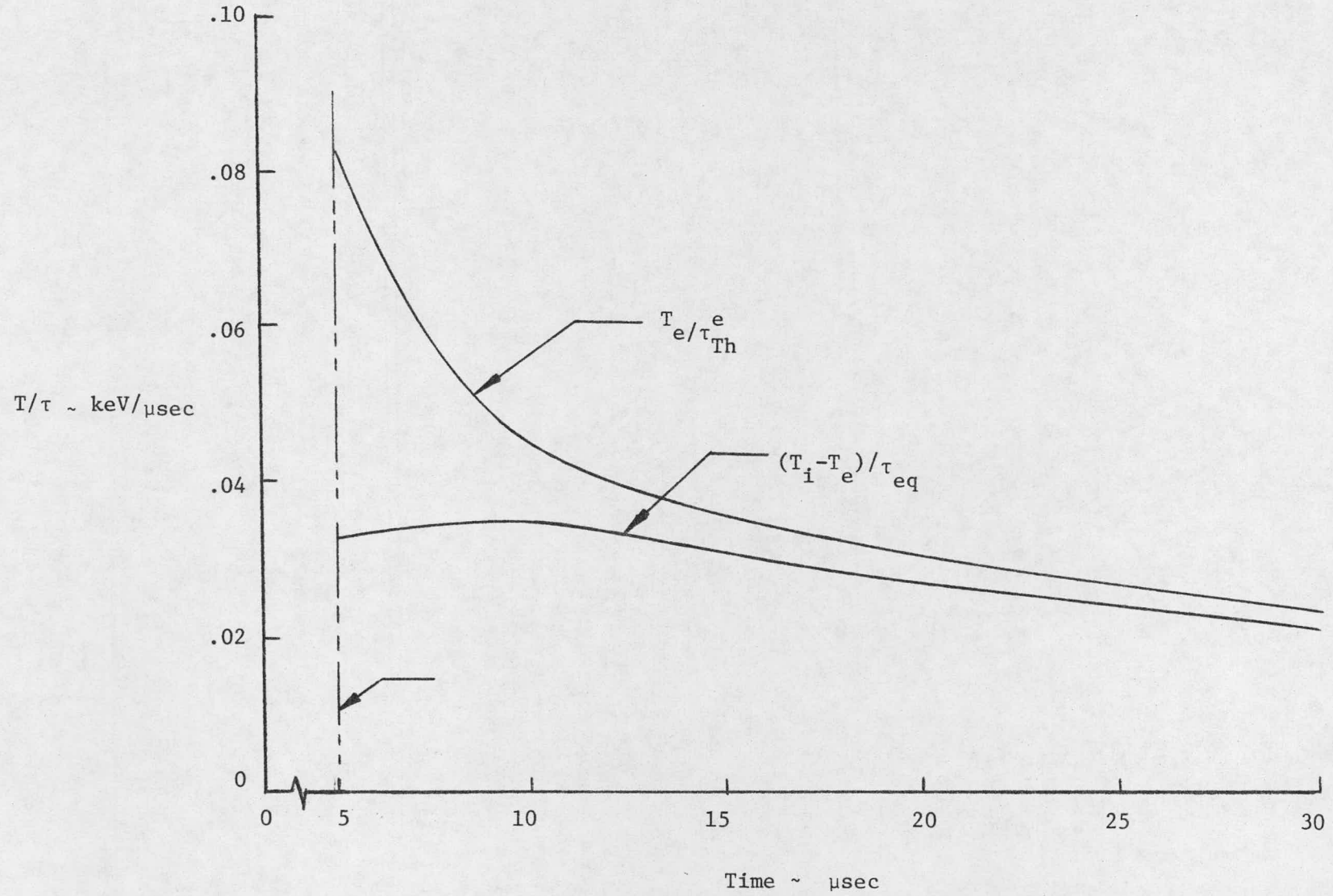

Figure 23. Electron Power Balance - Scylla IV-P

particle end loss time, 11.5μsec , determined from end on interferometry. Ion temperature was found to decay from the crowbarred value of 2.7 keV to 2.0 keV, assuming no ion thermal conduction. Experimental results presented did not include an ion temperature history. Consequently, the importance of ion thermal conductivity could not be verified. Electron temperature was found to decay from 610 ev at crowbar to 410 ev at 10μsec after discharge initiation, slightly higher than the factor of two drop in electron temperature observed with Thomson scattering. Again, the end loss parameter χ was chosen to agree with end loss interferometry data and was found to be 0.61.

Both Scylla IC, ($\lambda_{ii} << 1$), and Scylla IV-3, ($\lambda_{ii}/L=0.3 \longrightarrow .02$), were considered collisional experiments. Scylla IC was found to be a good experiment to study due to the comprehensive data base presented. The numerical simulation indicated that thermal conductivity effects are negligible, for τ^{e}_{Th} ranged approximately from 250μsec to 300μsec. Ion and electron temperatures were found to be nearly identical, in agreement with τ_{eq} <1μsec while τ^{i}_{Th} was on the order of milliseconds. Significant post-crowbar magnetic field oscillation made a detailed simulation of number density and temperature impossible. This prompted development of Model II. The end loss parameter, χ, was estimated from end on interferometry data to be 0.55 and is compared below with existing theories.

Scylla IV-3 simulations were made assuming that the plasma column was losing energy from classical ion thermal conduction. Due to the fact that $\lambda_{ii}/L = 0.3$ at crowbar, the validity of this

assumption is subject to question. Unfortunately, detailed T_i, T_e, n data are not available for analysis. Numerical simulation results indicate that ion energy loss by ion thermal conduction is approximately equal to the ion energy loss to the electrons, but less than the electron energy loss due to electron thermal conduction. Both electron and ion temperature thus decay monotonically. Over a time span of one particle confinement time, approximately 10 μsec, the characteristic times are: (1) $\tau_{Th}^{e} = 6\,\mu\text{sec}$; (2) $\tau_{Th}^{i} = 11\,\mu\text{sec}$ to $27\,\mu\text{sec}$ and (3) $\tau_{eq} = 15\,\mu\text{sec}$. The end loss parameter, χ, for this experiment was estimated to be 0.66. The end loss parameter determined for Scylla IV-3 and all other experiments discussed above will now be compared with experiment.

Results from the more significant end loss theories were summarized in Reference 28. The particle confinement time was presented in the form

$$\tau_p = \frac{L}{2} (m/2kT)^{\frac{1}{2}} \chi$$

where χ is a function of plasma β. Results from analytic theories were presented for collisional and collisionless plasmas with sharp boundary and diffuse profiles. Also included are the numerical results from an unsteady two dimensional MHD plasma theory. These results are reproduced in Figure 24 from Reference 28. The expression for τ_p used in Reference 28 differs from the scaling relation used in this study,

*Note that computer simulation η is plotted versus a β time averaged over τ_p.

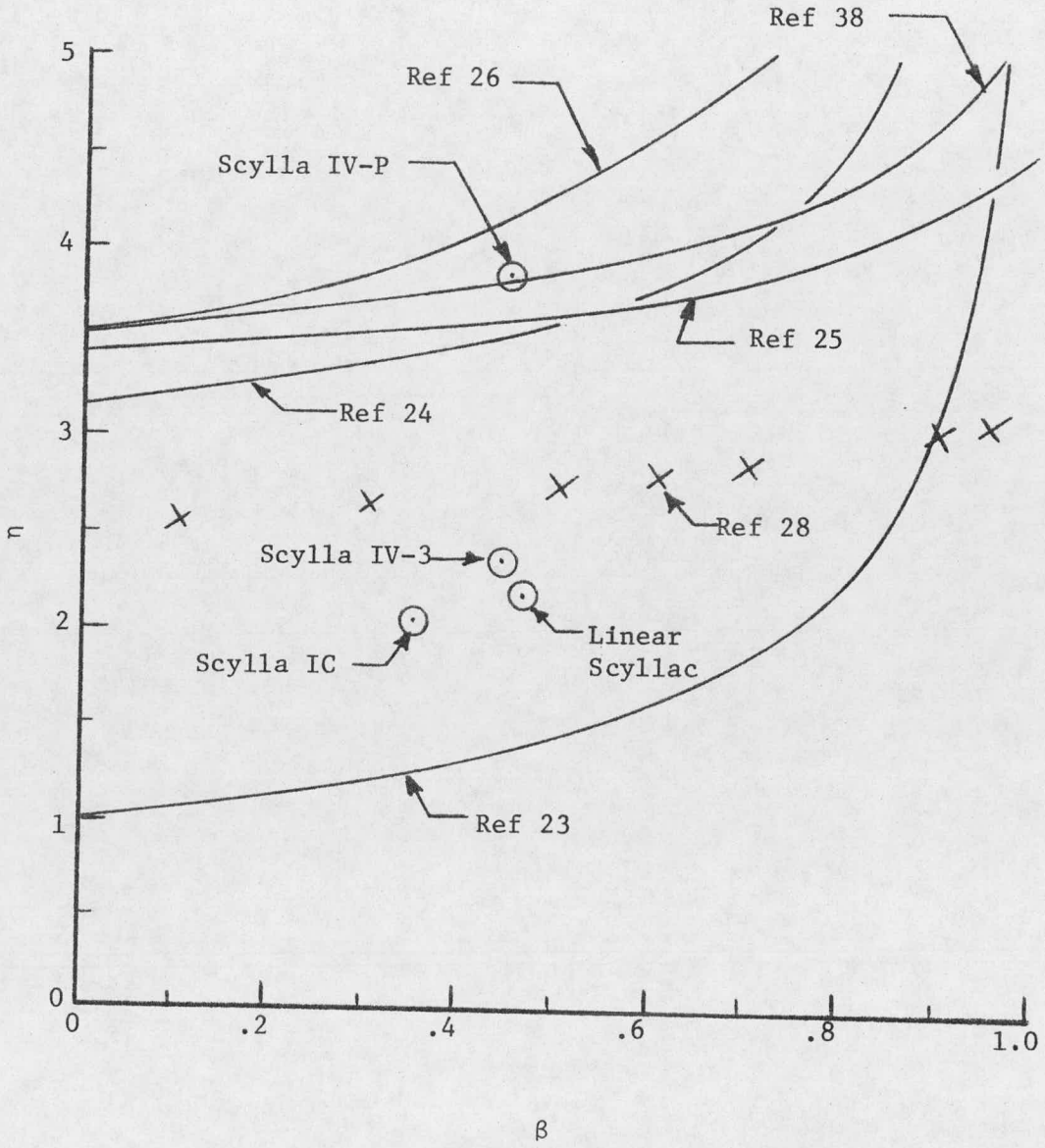

Figure 24. Theta Pinch End Loss Parameter versus Plasma Beta

$$\tau_p = \frac{L}{2}\left(\frac{m_i}{2kT_i}\right)^{\frac{1}{2}} \; 2\sqrt{\pi} \; \chi \quad ,$$

Thus the χ determined from the simulations discussed here must be multiplied by $2\sqrt{\pi}$ before comparisons can be made with Figure 24. A plasma column β, time averaged over τ_p, was calculated for each experiment from equation (11a) assuming the magnetic field remained constant after crowbar. These results are presented on Figure 24. Collisional experiments Scylla IC and Scylla IV-3 agree most closely with the numerical collisional MHD theory model. This would be anticipated, for the numerical model is unsteady, two dimensional and includes heat conductivity effects. Most of these effects were not considered in the analytic models due to the mathematical complexities introduced. Scylla IV-P results were found to be in agreement with Friedberg's[38] collisionless guiding center plasma model for a radially diffuse plasma profile. This is not surprising, for Scylla IV-P is a collisionless experiment. However, linear Scyllac was also a collisionless experiment, yet it shows the best agreement with MHD theory and differs considerably from collisionless theory scaling. This behavior is not understood at this time.

Use of the constant plasma area limitation imposes a strong constraint on the number of theta pinch experiments which may be reasonably considered, and specifically restricts applicability to only certain phases of plasma column development in those experiments.

In Model II, the constant area plasma column restriction was removed, enabling; (1) consideration of the magnetic compression phase following post implosion column formation, (2) study of non crowbarred capacitor energy storage systems and (3) a closer evaluation of crowbarred systems where the crowbarred magnetic field exhibits relatively wide variations over a characteristic particle confinement time. Model II was used to simulate two experiments: (1) Scylla IC, where the crowbarred field shows significant variation in applied magnetic field; and (2) the General Electric 50 cm theta pinch which was not crowbarred. In both cases specification of a post implosion initial condition was initially based on an approximate snowplow model.[39] These initial conditions were generally not sufficient to give good agreement with experimental data at later times, therefore a starting trial and error iterative process had to be performed to arrive at an acceptable initial condition.

The General Electric 50 cm theta pinch[40] will be considered first. The General Electric theta pinch was not crowbarred and, unlike all other theta pinch configurations investigated, it had mirrored ends which produced a vacuum mirror ratio of 1.24. This machine was found to produce a collisional plasma with λ_{ii}/L varying from 0.1 to 0.3. Ion thermal conduction was therefore included as a plasma loss mechanism. All confinement times τ_{EL}, τ^{i}_{Th}, τ^{e}_{Th} and τ_{eq} were found to be roughly $3_{\mu sec}$ to $5_{\mu sec}$ so that conductivity was indeed indicated to be an important energy loss mechanism. It was hoped that plasma column behavior could be deduced by using Model II to match electron number density and electron temperature data obtained

from a Thomson scattering diagnostic. Data were taken at several z locations along the machine centerline, but were limited to being on axis. The z dependency was averaged out to enable comparison with our computer model. These averaged data are presented in Figure 25 along with averaged column diameter data obtained from image converter photographs. The calculation was started at an initial condition which agrees closely with that used in the one dimensional code used in Reference 40. Assuming that the on-axis electron parameters were uniform across the column diameter, good agreement was found with our computer simulation where χ was chosen to be approximately .7, yielding $\tau_p \approx 3\mu sec$. Such results suggest that ion thermal conduction is indeed a plasma energy loss mechanism and that electron thermal conduction is reasonably described by Morse's model.[27] The good agreement between the computational model and the data suggests that magnetic flux is conserved. However, plasma properties were also calculated by relaxing the constant flux restriction for $t > 5\mu sec$. This was done by removing the bracketed energy loss terms in equation (12). The difference in number density and electron temperature between inclusion of flux conservation and relaxation of flux conservation was found to be small for this experiment. Jones et. al.[40] did not feel, based on their one-dimensional modeling, that the end loss was suitably characterized by a flux-conservation assumption. Their belief was that the flux in the plasma was either non-uniform along the axis, or decreased because of "onion-skin" leakage. Our zero-dimensional

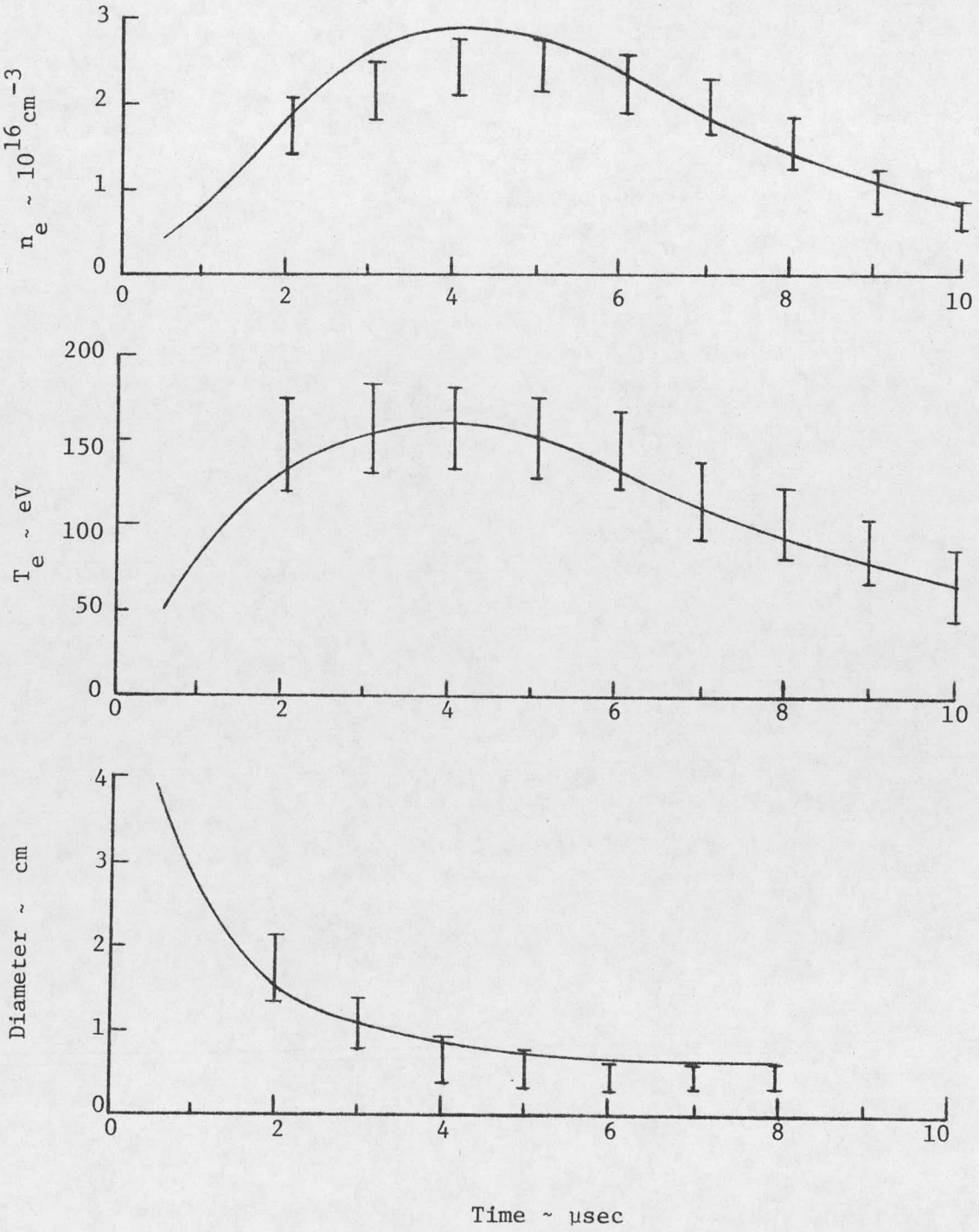

Figure 25. Comparison I of Numerical Simulation Solution with Experimental Results - GE pinch

modeling does not give insight on this issue. Indeed, as we discuss shortly, a model which allows flux diffusion into the plasma also gives good agreement with measured values of T_e and axially-averaged n. Consequently, we are not able to draw any conclusions about flux conservation. The difficulty is that the rise-time of the B field is on the same time scale as the particle and conduction losses. Hence, compression is occuring during most of the experiment. The plasma column radius, which is sensitive to flux behavior, is dominated by the compression field and is not sensitive enough to definitively determine flux behavior.

On the other hand, in the Scylla I-C experiment, the rise-time of the B field was very short (2μsec) and the field was crow-barred. Since the plasma radius was determined after crowbar by end-on interferometry, this makes it possible to check whether ϕ was indeed constant.

Model I results indicated that thermal conduction effects are unimportant in Scylla I-C and τ_p was known from interferometry results. Such a numerical simulation was performed using magnetic field waveform data presented in Figure 26. Plasma number density was found to significantly exceed the experimental results and the predicted temperatures following crowbar were found to increase rather than decrease. The predicted high number densities indicate that the column radius must have been greater than predicted. This behavior suggested that a radial flux diffusion mechanism was responsible. This was checked by assuming that a flux diffusion mechanism was operative which balanced out the bracketed energy loss terms in Equation (12). The results of this simulation are

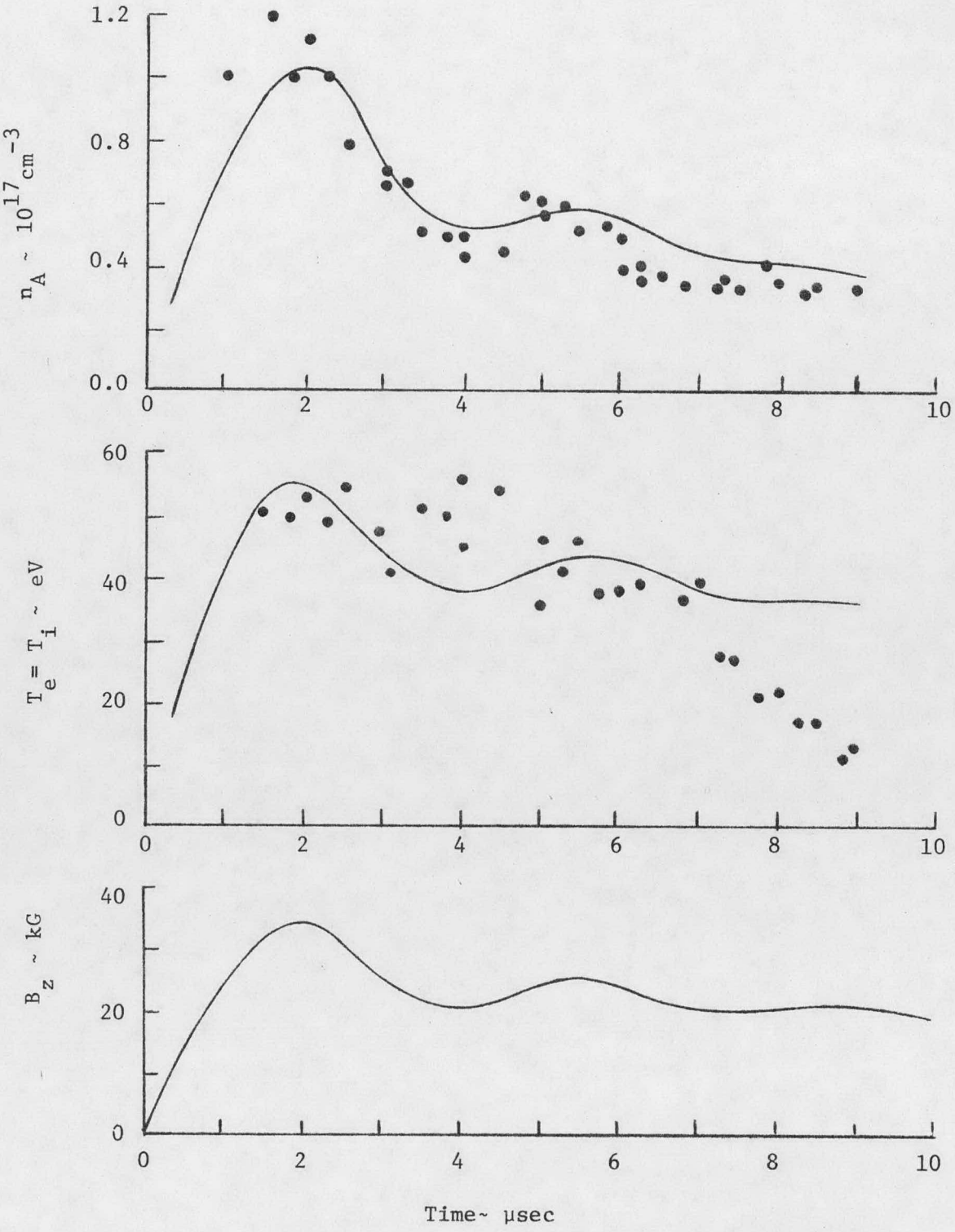

Figure 26. Comparison I of Numerical Simulation Solution with Experimental Results - Scylla-IC

also presented in Figure 26 and were found to agree closely with experiment[33] for $t < 7\mu sec$. This finding promoted development of computer simulation Model III which would enable evaluation of the observed flux diffusion.

In Model III, the effect on plasma column behavior of magnetic field diffusion into the plasma resulting from finite plasma resistivity is investigated. The radial variation in plasma column magnetic field was constrained to be parabolic, thus fixing the radial distribution of plasma through radial pressure balance. Computer simulations were conducted, assuming the Spitzer form of resistivity $\eta_\perp$, for current flow across a strong magnetic field. These results, presented in Figure 27, indicate that classical resistivity was responsible for the diffusion of magnetic flux into the Scylla I-C column. A sensitivity to plasma resistivity was checked by increasing plasma resistivity to $5 \times \eta_\perp$. These results, also presented in Figure 27, indicate that plasma column parameters are sensitive to plasma resistivity in this experiment. Thus plasma resistivity changes are distinguishable. Simulation results assuming plasma resistivity equal to the no magnetic field limiting case[34] ($\eta=\eta_\perp/2$) were found to yield slightly better agreement with experimental results, although the difference is considered insignificant, in light of the limitations of the accuracy of the model.

Presented in Figure 28 is a comparison between the experimentally observed near- Gaussian plasma number density distribution and the numerically determined distribution. Reasonable agreement was found between the profiles for $t = 2.5\mu sec$, $6\mu sec$ and $8\mu sec$.

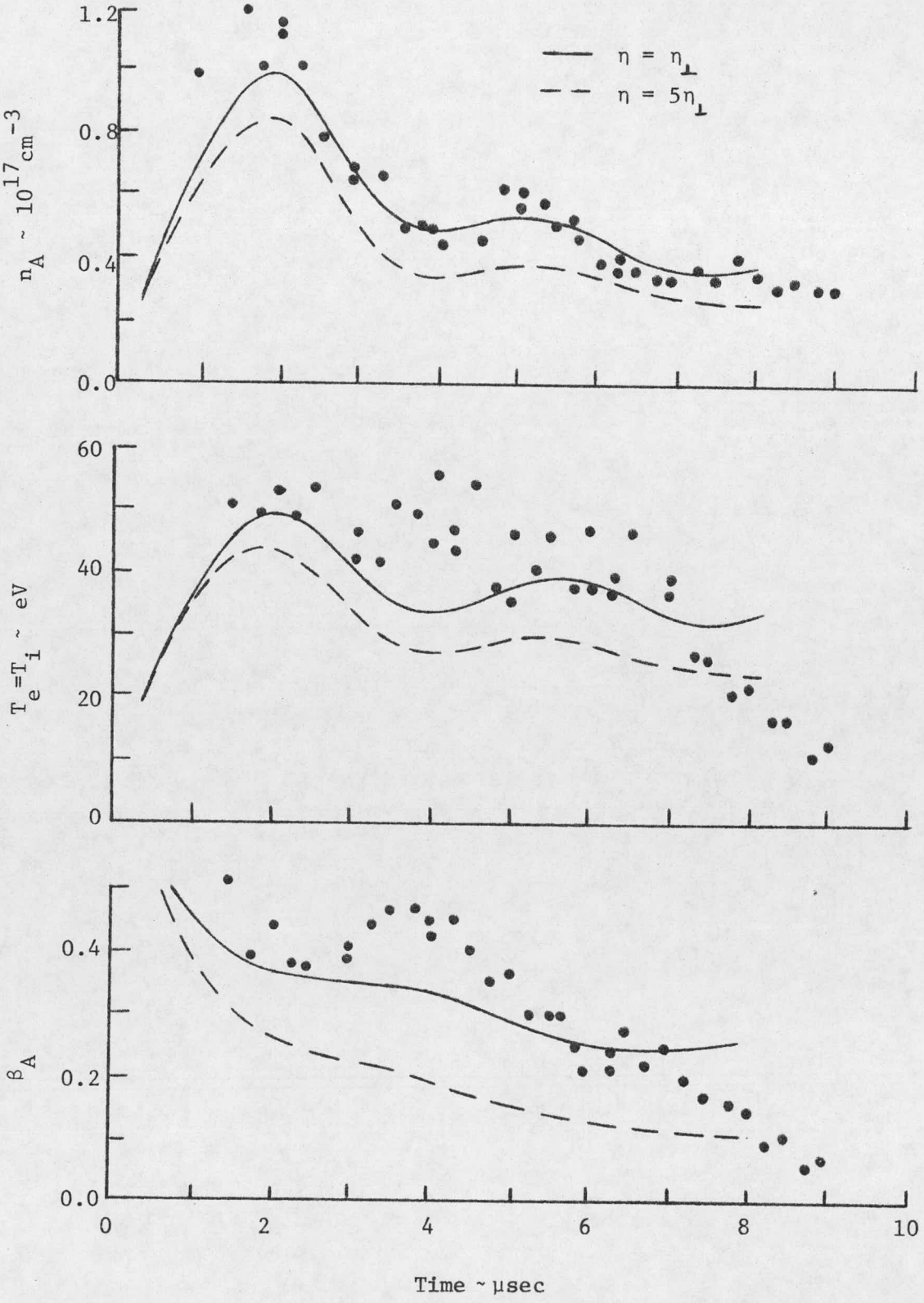

Figure 27. Comparison II of Numerical Simulation Solution with Experimental Results - Scylla-IC

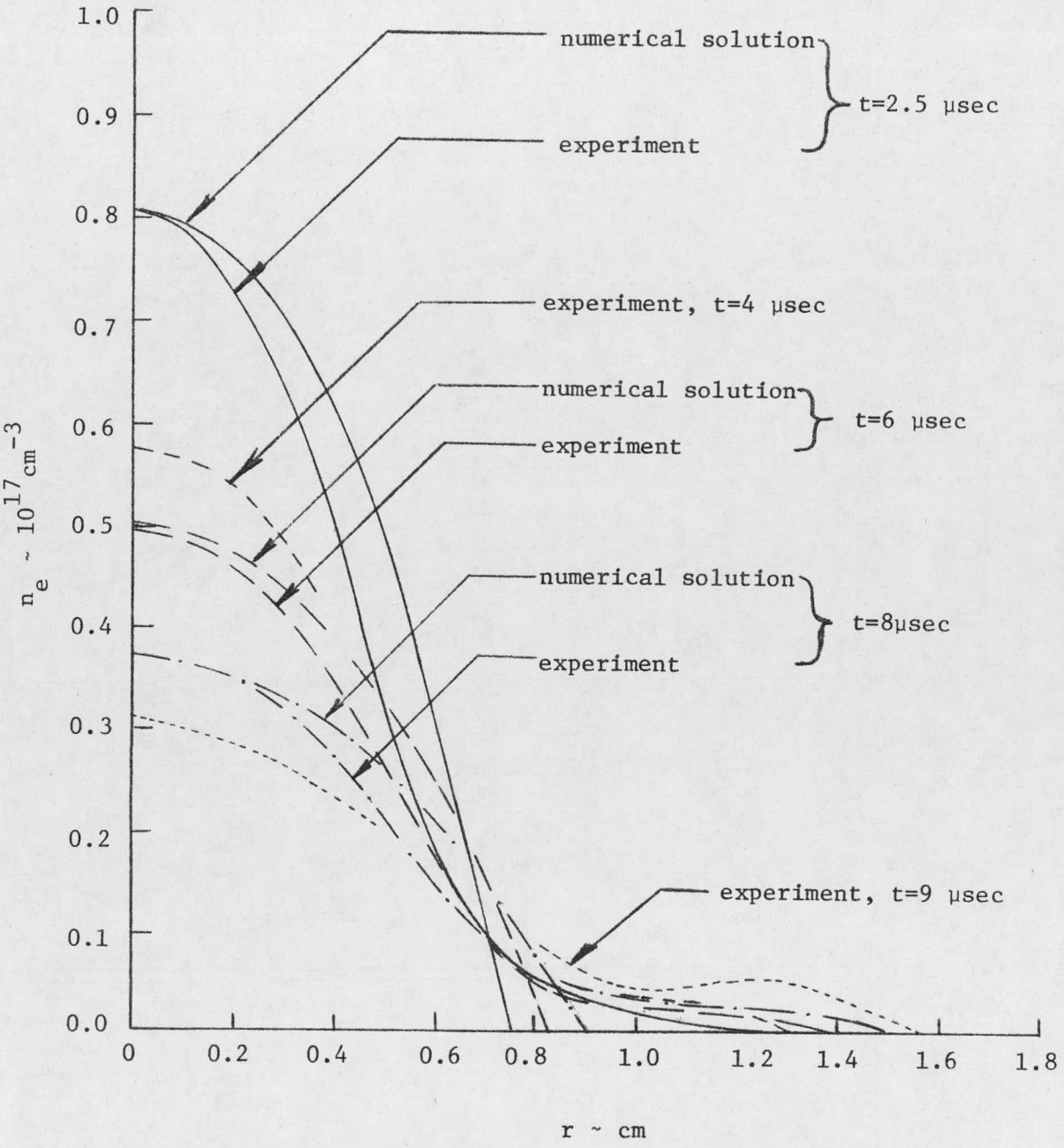

Figure 28. Comparison of Numerical Solution with Experimental Number Density Profile - Scylla-IC

An inexplicable 25 per cent difference between simulation and experiment was found on axis at 4μsec and the results at 9μsec were not compared in the interest of clarity. It is significant to note that both simulation and experiment indicate relatively small changes in column radius with time, consistent with the assumed Model I results discussed above for Scylla I-C.

The General Electric theta pinch was also evaluated using the flux diffusion computer simulation model. These results are presented in Figure 29 along with experimental data for electron number density, column diameter and electron temperature. Good agreement between simulation results and number density and temperature data was found by choosing the end loss parameter, χ=1.4. This resulted in a particle end loss time of 7μsec. Jones et. al.[40] state that between $t = \frac{1}{2}$μsec and 5μsec, the end loss time is 1.5μsec, roughly a factor of 5 smaller. Good agreement between experiment and simulation was found using the flux conservation model by letting χ= 0.7. This resulted in a particle end loss time of 3μsec. It should be noted that Thomson scattering data were taken only on axis, so the experimental estimate of end loss time is open to question. Furthermore, the lack of experimental ion temperature data does not permit η to be identified with reasonable certainty. End on interferometry data or Thomson scattering data properly averaged over plasma column radius and length would have enabled particle end loss to be treated here self consistently. Simulated plasma diameter using the flux diffusion model was found to be consistently greater than values obtained using an image

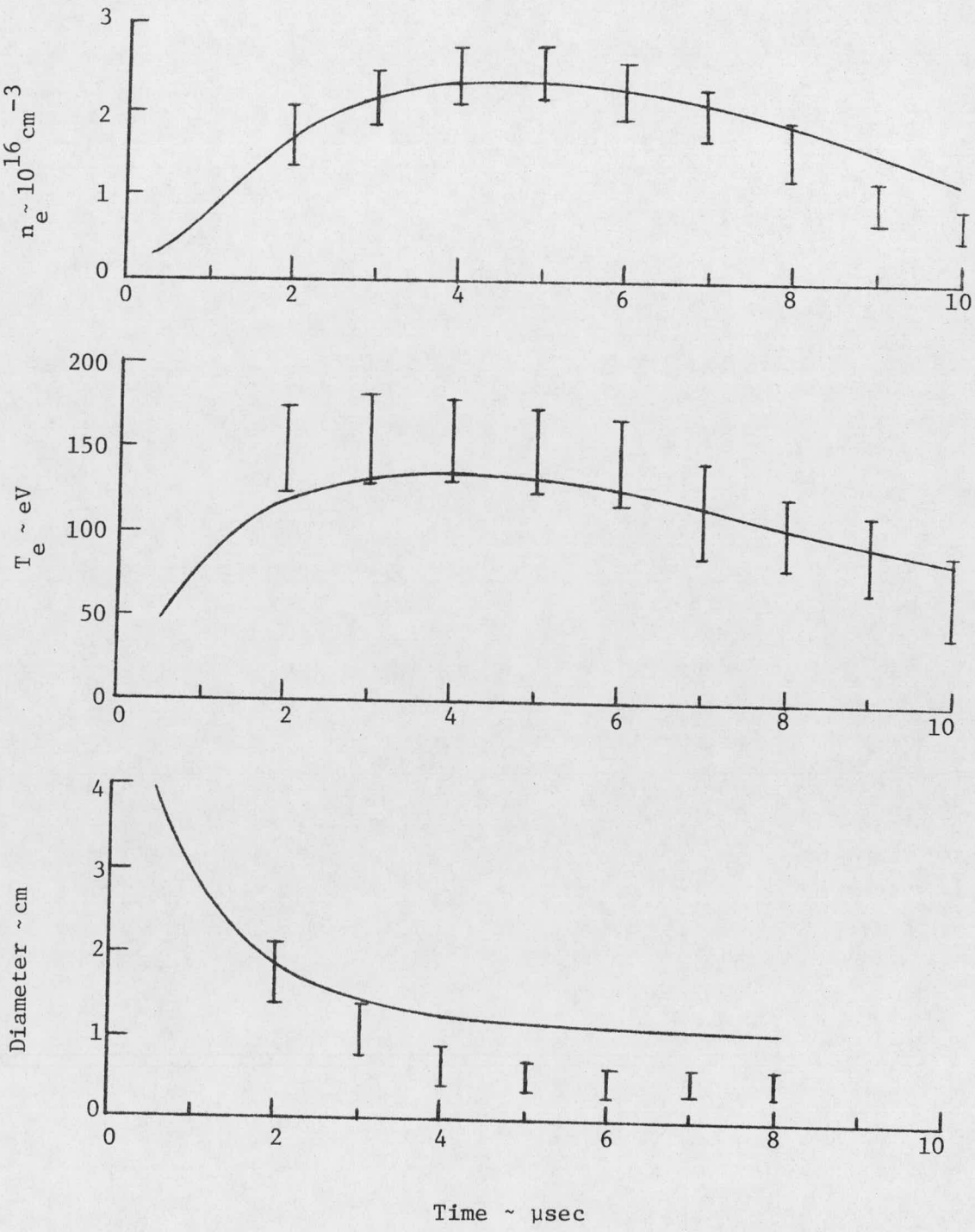

Figure 29. Comparison II of Numerical Simulation Solution with Experimental Results - Scylla-IC

converter camera. The flux conservation simulation yielded column diameter closer to the measured values but still slightly higher than measured values for $t>4\mu sec$. It is felt that the scope of experimental data presented in the General Electric theta pinch experiment is not sufficient to allow a detailed comparison with the computational models presented here.

4. Theta Pinch Scaling

This work was begun by T. York while at Los Alamos in the summer of 1976. A report on this work, entitled "Scaling of End Loss Times in Linear Theta Pinches" was completed under the contract and is appended as Report COO-4020-1.

Computer simulations are planned in the near future to provide more detailed scaling information, and to compare with the predictions in the above report.

5. Future Work

During the next several months, the zero-dimensional time-dependent modeling program will be largely completed. The following topics remain to be examined:

1. Simulation of the PSU 25 cm and 50 cm pinches. Predictions will, when possible, be compared with experimental results.
2. Scaling Study--The expected behavior of longer theta pinches - 15m to 150m - will be investigated.
3. Parameter study to determine the sensitivity of particle and energy end loss to variations in resistivity η, end loss parameter χ and thermal conduction parameter ℓ_1.
4. Assessment of the validity of the Morse model for thermal conduction. Alternate models, especially the one of Green et. al., will be examined for comparison.

VIII. FUSION ENGINEERING STUDIES
(E. Klevans and R. Ankney)

1. Introduction

A small part of the effort on this research project has been aimed at defining and determining the parameters needed to achieve power with a linear theta pinch system. This work began in 1976 prior to receiving contract support, and was continued by E. Klevans under the contract. It resulted in the paper "Machine Parameters For Linear Theta Pinch Fusion Reactors," which was presented at the American Nuclear Society Second Topical Meeting on the Technology of Controlled Nuclear Fusion, September 21-23, 1976, Richland, Washington. This paper is included as report COO-4020-2 which is appended to the present technical report.

In essence, the work extended the paper by Ellis'[41] on reactor modeling to include thermal conductivity and to allow for implosion models other than the programmed bounce model. The latter is required for the higher fill pressures that were associated with very high magnetic fields. It was found that Ellis' results were optimistic with regard to coil length, coil diameter, magnetic energy storage and efficiency.

Those calculations assumed that there was no significant end

stoppering. They were all very long devices. For example, the device that used B=300 kG was 4.2 km long and had a coil radius of 21 cm. Even the fusion/fission hybrid design with B=300 kG had a length of 1 km.

2. Requirements for "Interesting" Machines

Recent calculations have been devoted to determining target criteria for achieving a commercially interesting and technologically feasible linear theta pinch system. Sample results are shown in Table 1. Parameters down through neutron wall loading were specified, while those below neutron wall loading were computed.

Of special interest are the end loss enhancement factor and the thermal conduction enhancement factor. The end loss enhancement factor is the multiplicative increase required over that indicated by Linear Syllac confinement. However, the latter had a beta of only 0.73. With Scylla IV-P scaling and extrapolation of β to unity, an end loss enhancement factor of only 10 may be adequate. A more serious problem is suggested by the thermal conduction enhancement factor. For short machines this is especially serious. These results emphasize that fact that solution of the particle confinement problem is necessary but not sufficient.

The machine parameters listed in Table 1 indicate that the electrical output is rather low. To increase the power, one could increase the burn time. However, this would increase the

TABLE 1
Parameters for a Linear Theta Pinch Power Reactor

Magnetic Field	300 kG
Coil radius	10 cm
Length	300 m
Average Burn Temperature	10 keV
Mean Burn Time	10 ms
$n\tau_E$	5×10^{14} sec-cm^{-3}
Average Ion Density	1.1×10^{-17} cm^{-3}
E_θ	2 kV/cm
Neutron Wall Loading	3.5 MW/m^2
Cycle Time	4 sec
Total Power Produced (Including Blanket)	1000 MW
Electrical Power Produced (Assuming a thermal efficienty of 42% and a direct conversion efficienty of 55%)	340 MW
Magnetic Energy Storage	5 GJ
End Loss Enhancement Factor (based on Linear Syllac scaling)	22
Thermal Conduction Enhancement Factor	72
Fractional Burnup	7.7%

end loss enhancement factor even further.

3. Future Work

The zero dimensional time dependent computer model which has been developed to model theta pinch experiments will be used to determine the validity of the scaling laws used in our previous fusion engineering work, and to obtain design parameters for linear systems of potential interest. This work will be initiated during the Spring Term 1977 by an undergraduate student who will receive academic credit and will not be supported by the contract.

IX. ANALYSIS OF PLASMA BEHAVIOR IN THE EXHAUST REGION
(E. Stover)

Discussed are the results of a preliminary analysis conducted to identify plasma parameters in the exhaust region of the Penn State 50 cm theta pinch. Relevant plasma parameters such as mean free path and ratio of gyro frequency to collision frequency were used to identify which particle interactions are relevant in the exhaust and whether the exhaust should be treated as collisional or collisionless. Plasma properties, number density and temperature, used to evaluate these parameters were determined using a simple, isentropic, steady, gas dynamic model. The above number density and temperature distributions were compared to those predicted by a collisionless guiding center plasma model.

The collisional gas dynamic model adopted here assumes that the plasma isentropically expands in one dimension to the vacuum chamber walls in a convergent-divergent nozzle. The plasma is represented as a perfectly conducting compressible fluid. The plasma column was considered to have a throat[33] at each end of the compression coil and to maintain a reasonably constant number density and temperature. The ratio of exhaust vessel background pressure to plasma column pressure was considered sufficiently low such that the flow in the throat is sonic and the exhaust flow is supersonic throughout. This analysis will be approximately valid over the time interval that it takes a pressure disturbance to propagate upstream to the point under consideration due to the exhaust wave front interacting with the vacuum wall. This point will be addressed more completely in the next phase of our work. By assuming both fully isentropic flow

and a sonic throat, the variation of pressure, temperature, and density can be evaluated at any point in the exhaust as a function of plasma cross sectional area and plasma column properties[42] (zero subscript) from

$$\frac{A}{A^*} = \frac{1}{M^2}\left[\frac{2}{\gamma+1}\left(1+\frac{\gamma-1}{2}M^2\right)\right]^{(\gamma+1)(\gamma-1)}$$

$$\frac{T}{T_o} = \left(1+\frac{\gamma-1}{2}M^2\right)^{-1} ,$$

$$\frac{P}{P_o} = \left(\frac{T}{T_o}\right)^{\gamma/(\gamma-1)} ,$$

$$\frac{\rho}{\rho_o} = \left(\frac{T}{T_o}\right)^{1/(\gamma-1)} ,$$

where A^* is the plasma throat area, $T \doteq T_e + T_i$, and γ is the ratio of specific heats,

$$\gamma = (n+2)/_n ,$$

with n equal to the number of fully excited degrees of freedom for a plasma particle.

The axial distribution of the exhaust cross sectional area was found by invoking radial pressure balance,

$$P = \beta B_e^{\,2}/2\mu_o , \qquad (2)$$

where B_e is the external magnetic field. The magnetic field distribution, $B_e = B_e(z)$, was predicted from the law of Biot and Savart[43] in which the compression coil current was assumed to have a uniform axial distribution. Vacuum discharges of the Penn State 25 cm theta pinch suggest that the compression coil current is not

uniformly distributed but is instead higher at the coil end. This resulted in slightly higher B fields at the end than predicted. The exhaust B_e profiles determined from the law of Biot and Savart were corrected for this mirroring effect.

Some uncertainty exists in specifying the throat area. Therefore, the isentropic flow calculations were made assuming that the throat area is: (1) equal to the plasma column area; and (2) equal to the area inferred from the end loss model of Brackbill.[28]

$$A_t = \left(\frac{1}{\chi}\right) A_c \qquad (1)$$

where r_c is the plasma column radius and χ is the end loss parameter which is not very sensitive to β and was taken to be 3. Selecting a value for γ also involves uncertainty but a plasma without internal structure with three translational degrees of freedom will be assumed here. For a fully dissociated, fully ionized hydrogen plasma then, $\gamma = \frac{5}{3}$.

For plasma column conditions obtained from a snowplow implosion analysis,[39] $T_e=T_i=$ 290 eV, $n_i=n_e=5\times10^{16}$ cm^{-3} and $r_c=0.5$ cm with $\beta=1$, exhaust plasma properties were calculated assuming throat area equal column area, and are presented in Table 1. Using these results, the interaction of the exhaust plasma with the background gas was evaluated. Mean free paths were evaluated for: electron-neutral and for ion-neutral interactions using

$$\lambda = \frac{1}{n\sigma} \quad ,$$

Table 1. Collisional Gasdynamic Model Exhaust Properties
$\beta = 1.0$
Penn State 50cm Theta Pinch

z(cm)+	r(cm)	T(eV)*	$n^*(10^{16}cm^{-3})$
0	.50	217	3.3
2.0	.53	165	2.2
3.5	.66	110	1.2
5.5	.9	73	.63
8.5	1.2	45	.32
11.8	1.6	31	.18
14.0	2.0	22	.11
18.0	2.4	16	.07
21.3	3.5	11	.035
23.0	4.5	7	.021

+ Referenced to the compression coil end plane.

* $T = T_e = T_i$, $n = n_e = n_i$

where σ is the cross section for the interaction of interest and n is the background gas number density.

Three electron-neutral interactions were considered: (1) elastic scattering; (2) excitation; and (3) ionization. A summary of electron-neutral mean free path results are presented in Table 2 based on cross section data presented by Jahn [44] and Mitchner and Kruger. [45] Elastic interactions were found to be the dominate electron-neutral interactions and should be significant only in the downstream half of the vacuum vessel. Excitation interactions were found to be negligible with mean free paths two orders of magnitude greater than the exhaust vessel length, 25 cm. Ionization mean free paths were found to be approximately twice the exhaust vessel length. Thus, electron-neutral ionization interactions also are not important. The total mean free path was evaluated for all electron-neutral interactions and found to vary from 12 cm at the coil end to 3 cm at the exhaust vessel end plane, so that these interactions will be important only in the exhaust far field.

Two ion-neutral interactions were considered: (1) elastic scattering; and (2) charge exchange. A summary of mean free path results for these interactions are presented in Table 3 for $H_e^+ - H_e$ interactions. Data trends from Jahn [44] indicate that H^+ -H cross sections are approximately 80 per cent the $H_e^+ - H_e$ cross sections. Therefore H^+-H interaction mean free paths would be only 20 per cent higher than the $H_e^+ - H_e$ values presented in Table 3. The charge exchange interaction was found to be important throughout

Table 2. Mean Free Path for Interaction of Exhaust Electrons with Background Neutrals Penn State 50cm Theta Pinch

z(cm)	T(eV)	λ^+(cm) Elastic Scattering	λ^+(cm) Excitation	λ^+(cm) Ionization	λ^+(cm) Total
0	217	15	2200	60	12
2.5	165	15	2200	60	12
4.8	110	15	1700	43	11
7.2	73	13	1700	40	10
10.0	45	10	1700	60	9
14.0	31	6	1700	75	6
16.5	22	5	1500	100	5
19.4	16	4	1500	∞	4
25	11	3	∞	∞	3

+ Background pressure is 10mTorr.

* Cross section for Helium used.

Table 3. Mean Free Path for Interaction of Exhaust Ions with Background Neutrals Penn State 50cm Theta Pinch

z(cm)	T(eV)	λ^+(cm) Elastic Scattering	λ^+(cm) Charge Exchange	λ^+(cm) Total
0	217	10	1.2	1.1
2.5	165	9	1.1	1.0
4.8	110	8	1.0	.9
7.2	73	5	1.0	.9
10.0	45	4	1.0	.8
14.0	31	3	.9	.7
16.5	22	2	.9	.6
19.4	16	2	.8	.5
25	11	1	.7	.4

+ Background pressure is 10mTorr

the exhaust plume with mean path remaining constant throughout at approximately 1 cm. Elastic interaction mean free path was found to vary from 10 cm at the compression coil end plane to 1 cm at the exhaust vessel end plane. These results indicate that energy and momentum transfer from the exhaust plasma to the neutral background will be important only in the exhaust far field.

Exhaust plume parameters describing both the interaction between exhaust plume electrons and ions and the interaction of the plasma with the magnetic field are summarized in Table 4. Electron and ion mean free paths were found to vary from approximately 3 cm at the coil end plane to approximately 1 cm at the exhaust vessel end plane. In addition, the ratio of cyclotion frequency to collision frequency, ω_c/ν, was found to vary from coil end plane to near exhaust vessel end plane with values of 11 to 0.2 and 330 to 6 for ions and electrons respectively. These results suggest that the plasma is collisionless in the vicinity of the throat and becomes collisional further downstream. Ion gyro radius varied from .07 cm in the throat, approximately 20 per cent of the throat radius, to 2.8 cm near the vacuum vessel end plane, over 60 per cent of the vacuum vessel radius.

Exhaust plume properties were also calculated using the gas dynamic collisional model for cases $\beta = 0.6$ and $\beta = 0.8$. Plasma column properties were determined by modifying the implosion dynamics model of York and McKenna[39] to include magnetic flux trapped in the plasma. This analysis yielded the plasma column properties

Table 4. Exhaust Interspecies Interaction and Interaction With the Applied Magnetic Field Penn State 50cm Theta Pinch

	Ions			Electrons		
z(cm)	λ_i(cm)	ω_{Li}/ν_i	r_{Li}(cm)	λ_e(cm)	ω_{Le}/ν_e	r_{Le}(cm)
Column	3.6	11.0	.05	2.5	330	.001
0	3.0	7.4	.07	2.1	230	.001
2	2.7	4.8	.11	1.9	144	.002
3.5	2.2	3.6	.16	1.6	105	.003
5.5	1.8	2.0	.28	1.3	60	.006
8.5	1.4	1.2	.47	1.0	36	.009
11.8	1.2	.6	.89	.84	19	.018
14.0	1.0	.5	1.2	.72	14	.021
18	.9	.3	2.0	.62	9	.040
21	.7	.2	2.8	.52	6	.056

$\beta = 0.8$ $\quad T_e = T_i = 271$ eV

$n_e = n_i = 4.3 \times 10^{16}$ cm^{-3}

$r_c = 0.54$ cm

$\beta = 0.6$ $\quad T_e = T_i = 247$ eV

$n_e = n_i = 3.5 \times 10^{16}$ cm^{-3}

$r_c = .60$ cm .

Plasma column throat radius was determined for each β from equation 1 with $\eta=3$,

$\beta = 1$ $\quad r_t = .29$ cm ,

$\beta = 0.8$ $\quad r_t = .31$ cm ,

$\beta = 0.6$ $\quad r_t = .35$ cm .

Plasma column properties are presented in Table 6 for $\beta = 0.6$ and $\beta = 0.8$. The per cent change in plasma temperature and number density for β variations considered here, were found to be sufficiently small so that variations in λ_i, λ_e, ω/ν and r_L would not be appreciable. Exhaust boundries are depicted in Figure 30 for $\beta = 1$ with $r_t = r_c$ and $r_t = .29$ cm and for $\beta = 0.6$ with $r_t = .35$cm. Note that the exhaust boundary intersects the vacuum vessel either at or near the exhaust vessel end plane.

The gas dynamic model results presented above are compared with the results from a simple, collisionless, guiding center plasma (GCP) model. For a collisionless plasma, the magnetic moment, μ is an adiabatic invariant

$$\mu = W_\perp / B_i \quad ,$$

Table 6. Collisional Gasdynamic Model Exhaust Properties
$\beta = 0.6$ and $\beta = 0.8$
Penn State 50cm Theta Pinch

	$\beta = 0.6$			$\beta = 0.8$		
z(cm)	r(cm)	T*(eV)	n*	r(cm)	T*(eV)	n*(cm^{-3})
Column	.6	247	3.5×10^{16}	.54	271	4.3×10^{16}
.0	.35	185	2.3×10^{16}	.32	203	2.8×10^{16}
2.0	.37	141	1.5×10^{16}	.33	155	1.8×10^{16}
3.5	.46	94	8.4×10^{15}	.41	103	1.0×10^{16}
5.5	.60	62	4.4×10^{15}	.54	68	5.4×10^{15}
8.5	.83	38	2.2×10^{15}	.75	42	2.7×10^{15}
11.8	1.1	26	1.3×10^{15}	.99	29	1.6×10^{15}
14.0	1.4	19	7.7×10^{14}	1.3	21	9.5×10^{14}
18.0	1.7	14	4.9×10^{14}	1.5	15	6.0×10^{14}
21.3	2.4	9	2.5×10^{14}	2.2	10	3.1×10^{14}
25.0	3.3	6	1.4×10^{14}	3.0	7	1.7×10^{14}

* $T = T_e = T_i$, $n = n_e = n_i$

Figure 30. Plasma Exhaust Boundaries

Penn State 50cm Theta Pinch

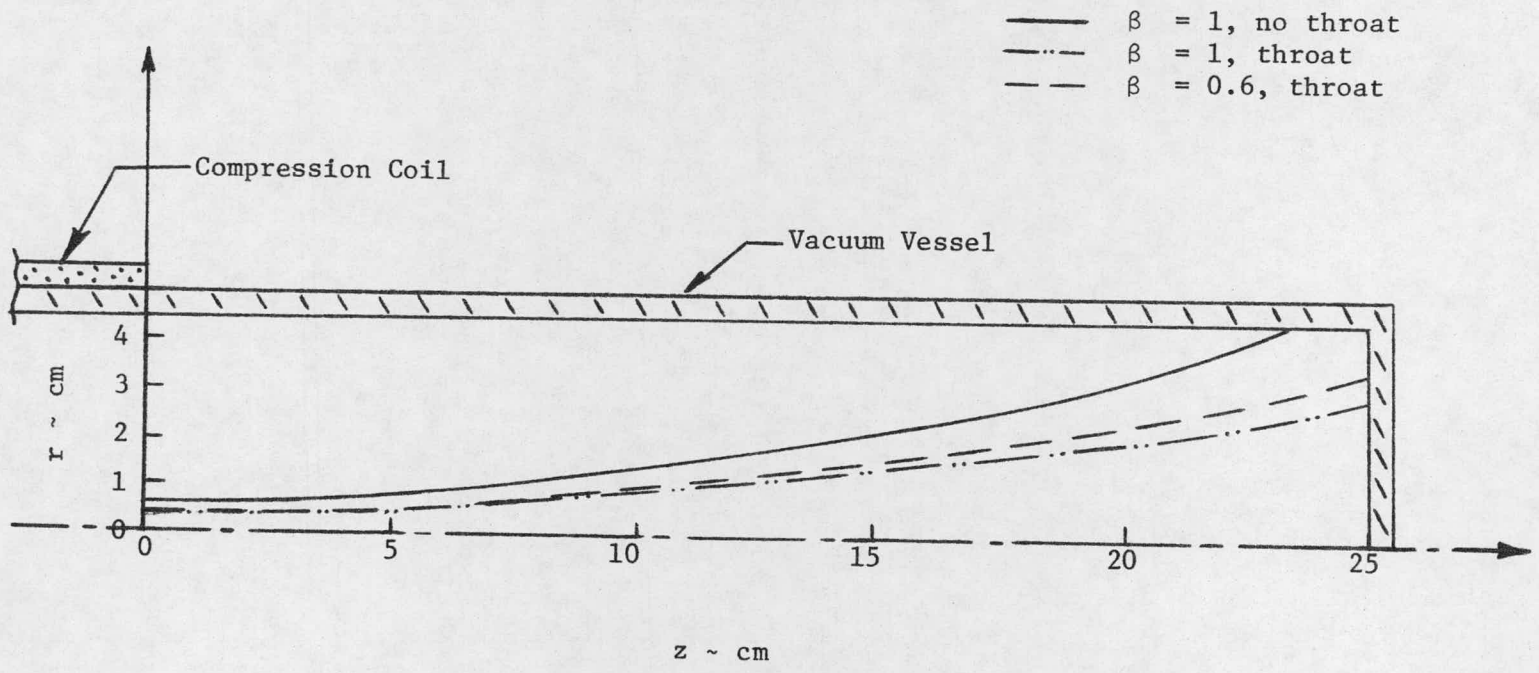

where

$$W_{\perp} = \frac{1}{2} m v^2$$

and B_i is the magnetic field internal to the plasma. The radial pressure, P can be expressed as

$$P = nkT \approx n W_{\perp} \qquad (3)$$

Therefore

$$\frac{P}{nB_i} = \text{constant} . \qquad (4)$$

From radial pressure balance expressed as equation (2), and an alternate form

$$B_i = B_e (1-\beta)^{\frac{1}{2}} , \qquad (5)$$

and furthermore assuming β = constant along the length of the exhaust, then

$$\frac{B_e}{n} = \text{constant} .$$

From known plasma column source conditions and known magnetic field distribution, the number density distribution was found. Perpendicular temperature was then evaluated by combining (3), (4) and (5). Exhaust radius was found from flux conservation

$$B_i A_p = \text{constant}$$

and (5). Exhaust plasma temperature and number density distributions were calculated using this model for $\beta = 0.6$ and $\beta = 0.8$. These GCP results are presented in Figure 31 along with the corresponding gas dynamic model results for $\beta = 0.6$. Agreement between models was found to be good with GCP perpendicular temperature predicted slightly lower than the gas dynamic model temperature and CGP number density predicted slightly higher than the gas dynamic model number density.

Figure 31. Comparison of Exhaust Characteristics Between Gasdynamic and GCP Theories
$\beta = 0.6$
Penn State 50cm Theta Pinch

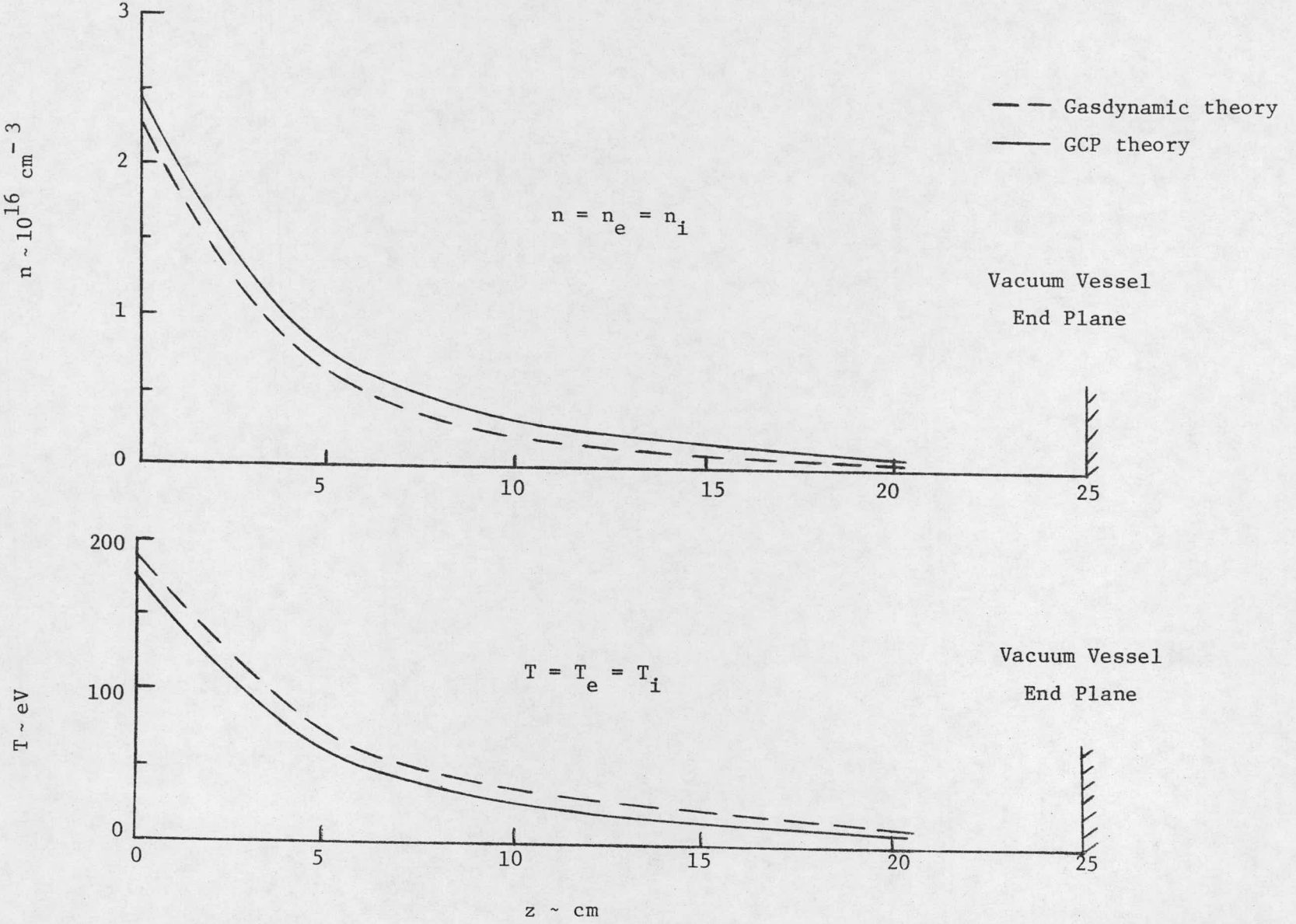

X. REVIEW OF FACULTY AND STUDENT PARTICIPATION

T. M. York Associate Professor of Aerospace Engr.	June 1976 July 1976 Sept.-May	FT FT 35%	2 weeks 2 weeks
(Visiting Staff Member Los Alamos Scientific Laboratory)	June-July	FT	2 weeks
E. H. Klevans Professor of Nuclear Engineering	June 1976 July 1976 Sept.-May	FT FT 25%	4 weeks 4 weeks
John Heidrich Graduate Assistant, Physics	June 1976- May 1977	50%	
Elemer Stover Graduate Assistant, NucE	Sept. 1976- May 1977	50%	
Barry Jacoby Graduate Assistant, NucE	Sept. 1976- May 1977	50%	
Robert Freeman Graduate Assistant, NucE	Dec. 1976- Feb. 1977 Mar. 1977- May 1977	25% 50%	

XI. PROJECT REFERENCES

1. Reports

   a. T. M. York, Scaling of End Loss Times in Linear Theta Pinches, ERDA C00-4020-1, Sci. Rept. 77-1, The Pennsylvania State University, January 1977.

2. Reports and Preprints

   a. E. H. Klevans and R. Ankney, Machine Parameters for Linear Theta Pinch Fusion Reactors, ERDA C00-4020-2, Sci. Rept. 77-2, The Pennsylvania State University, January 1977.

3. Presentations

   a. E. H. Klevans with R. Ankney, Machine Parameters for Linear Theta Pinch Fusion Reactors, paper presented at Second Topical Meeting on the Technology of Controlled Nuclear Fusion, September 21-23, 1976, Richland, Washington.

   b. T. M. York with E. H. Klevans, Scaling of Particle and Energy End Loss in Linear Theta Pinches, presented at 18th Annual Meeting of the American Physical Society, Division of Plasma Physics, November 15-19, 1976, San Francisco, California.

4. Abstracts Accepted for Presentation

   a. E. Stover, E. H. Klevans and T. M. York, Computer Modeling of Linear Theta Pinch Machines accepted for presentation of IEEE International Conference on Plasma Science May 23-25, 1977, Troy, New York.

   b. T. M. York, R. Freeman, R. Mollo, Evaluation and Scaling of Plasma Loss from a Very Short Theta Pinch, accepted for presentation of IEEE International Conference on Plasma Science May 23-25, 1977, Troy, New York.

References

1. Los Alamos CTR Program Progress Report for the Period Jan.-Dec. 1974 LA 6044-PR, August 1975, complied by F. L. Ribe.

2. B. H. Hui, S. Hamasaki, R. C. Davidson, "Fluid Numerical Studies of High-Density Theta-Pinch Implosion Including Chemical and Anomalous Transport Process," Nuclear Fusion, 16, 1 (1976) 73.

3. S. Hamasaki and N. A. Krall, "Parametric Study of Theta Pinch Implosions," Paper 7R2, Bulletin of Am. Phys. Soc., II, 21, 9 (1976) 1150.

4. R. H. Huddlestove and S. C. Leonard, Plasma Diagnostic Techniques, Ch. 3, Academic Press, New York (1965).

5. Los Alamos CTR Program Progress Report for the Period Jan.-Dec. 1972 LA-5250-PR, June 1973, complied by F. L. Ribe.

6. H. R. Griem, Plasma Spectroscopy, Ch. 13, 14, McGraw-Hill, New York (1964).

7. J. Sheffield, Plasma Scattering of Electromagnetic Radiation, Academic Press, New York (1975).

8. A. W. DeSilva and G. Goldenbaum, Methods of Experimental Physics 19 (Pt. A) (1970).

9. H. J. Kunze, in Plasma Diagnostics (W. Lochte-Holtgraven, Ed.) North Holland Pub. Co., Amsterdam (1968).

10. S. A. Ramsden, in Physics of Hot Plasmas (Rye and Taylor, Eds.) Plenum Press, New York (1970).

11. A. H. Shapiro, Compressible Fluid Flow, Ronald Press, New York (1953).

12. K. F. McKenna and T. M. York, "Plasma End Loss Studies on Scylla I-C" Los Alamos Scientific Laboratory Report LA-6412-MS, August 1976.

13. N. A. Krall and A. W. Trivelpiece, Principles of Plasma Physics, McGraw Hill, New York (1973).

14. F. C. Jahoda and G. A. Sawyer, "Optical Refractivity of Plasma" in Methods of Experimental Physics, Vol. 9, Part B. (Griem-Lovberg Eds.) Academic Press, New York (1971).

15. K. S. Thomos, "Measurements of θ-Pinch End Loss Using a Gas Laser Interferometer" Physics of Fluids, Vol. 11 (1963) 1125.

16. R. W. Peterson and F. C. Jacobs, "A Far-Infrared Coupled Cavity Interferometer" Appl. Physics Letters, Vol. 18 (1971), 440.

17. T. M. York and K. F. McKenna, "Laser Plasma Interactions in the Scylla I-C Experiment-Preliminary Analysis" Los Alamos Scientific Laboratory Report LA-5957-MS, May 1975.

18. G. M. Molen, "Multiple Beam Laser Interferometry" Preprint of paper presented at 1975 IEEE International Conference on Plasma Science, Ann Arbor, Michigan, May 1975.

19. G. B. F. Niblett and T. S. Green, Proc. Phys. Soc., Vol. 74 (1959) 737.

20. T. S. Green, "An Investigation of the Theta Pinch Using Magnetic Pick-up Loops," Nuclear Fusion, Vol. 2 (1962) 96.

21. K. F. McKenna and T. M. York, "Transient Flow and Expansion of a Pinch Discharge Plasma in Self-Induced Magnetic Fields," Plasma Physics, Vol. 17 (1975).

22. K. F. McKenna, "An Investigation of the Transient Plasma Flow from a Self-Field Pinch Discharge" Ph.D. Thesis, The Pennsylvania State University, June 1973.

23. J. B. Taylor and J. A. Wesson, "End Losses from a Theta Pinch," Nuclear Fusion, 5, 1965.

24. J. A. Wesson, "Plasma Flow in a Theta Pinch," in Plasma Physics and Controlled Nuclear Fusion Research (Proc. 2nd Int. Conf. Culham, 1965), 1, IAEA, Vienna, 1966.

25. J. P. Freidberg, H. Weitzner, "End Loss from a Linear θ-Pinch," Nuclear Fusion, 15, 1975.

26. R. L. Morse, "Adiabatic End Loss from a θ-Pinch," Physics of Fluids, 11, 7, 1968.

27. R. L. Morse, "Electron Temperatures and Thermal Conduction in High-Energy θ-Pinches," Physics of Fluids, 16, 4, 1973.

28. J. U. Brackbill, M. T. Menzel, and D. C. Barnes," Numerical Studies of the Linear Theta Pinch," LA-UR-75-1568.

29. H. A. B. Bodin, J. McCartan, I. K. Pasco, and W. H. Schneider, "Experimental and Two-Dimensional Computational Study of End Losses from a Theta Pinch," Physics of Fluids, 15, 7, 1972.

30. L. C. Steinhauer, "Endloss from a Slender High Beta Plasma Column Contained in a Linear Solenoid," Physics of Fluids, 19, 5, 1976.

31. S. I. Braginskii, "Transport Provesses in a Plasma," Review of Plasma Physics, 1, Consultants Bureau, New York, 1965.

32. T. S. Green, D. L. Fisher, A. H. Gabriel, F. J. Morgan, and A. A. Newton, "Energy Loss from a Theta Pinch," Physics of Fluids, 10, 8, 1967.

33. K. F. McKenna and T. M. York, "End Loss from a Collison Dominated Theta Pinch Plasma," submitted to Physics of Fluids for publication.

34. L. Spitzer, Jr., Physics of Fully Ionized Gases, Interscience Publishers, Inc., New York, 1956.

35. K. S. Thomas, H. W., Harris, F. C. Johoda, G. A. Sawyer, and R. E. Siemon, "Plasma Experiments on the Linear Scyllac Theta Pinch," Physics of Fluids, 17, 6, 1974.

36. Commisso, Ekdahl, McKenna, et. al., "Scylla IV-P", LASL Progress Report, CTR-3, July thru September, 1976.

37. R. F. Gribble, W. E. Quinn, R. F. Siemon, "Plasma Experiments with a Three-Meter θ-Pinch," Physics of Fluids, 14, 9, 1971.

38. J. P. Freidberg, unpublished.

39. T. M. York, K. F. McKenna, "Laser-Plasma Interactions in the Scylla 1-C Experiment: Preliminary Analysis," LA-5957-MS, 1975.

40. W. B. Jones, L. M. Goldman, R. W. Kilb, and R. L. Bingham," Energy and Particle Loss from a Short Theta Pinch," Physics of Fluids, 13, 3, 1970.

41. W. R. Ellis, "CTR Applications of the High-Density Linear Theta Pinch," Nuclear Fusion, 15, 1975, 255.

42. H. W. Liepmann and A. Roshko, Elements of Gasdynamics, John Wiley and Sons, Inc., New York, 1957.

43. J. D. Jackson, Classical Electrodynamics, John Wiley and Sons, Inc., New York, 1962.

44. R. G. Jahn, Physics of Electrical Propulsion, McGraw-Hill Book Company, New York, 1968.

45. M. Mitchner and C. H. Kruger, Jr., Partially Ionized Gases, John Wiley and Sons, Inc., 1973.